# Measurement of the ratio of neutron cross-section to proton cross-section in muon deep inelastic scattering at 490 GeV/c

by

Silhacène Aïd

Dissertation submitted to the Faculty of the Graduate School

of the University of Maryland in partial fulfillment

of the requirements for the degree of

Doctor of Philosophy

1991

Advisory Comittee :

Professor George Snow, Chairman/Advisor

Professor Dieter Brill

Professor Rabindrah Mohapatra

Professor Andris Skuja

Professor Scott Wolpert

AAB4585

## Abstract

Title of Dissertation : Measurement of The Ratio of Neutron Cross-section to Proton Cross-section in Muon Deep Inelastic Scattering at 490 GeV/c

Silhacène Aïd, Doctor of Philosophy, 1991

Dissertation directed by : Professor George A. Snow
Physics Department

The ratio of the neutron to proton cross-sections has been measured in deeply inelastic muon scattering at an incident beam energy of 490 GeV/c using a large-angle scattering trigger. The ratio was found to be consistent with unity as the scaling variable $x_{bj}$ approaches 0. It was found to be consistent with an independent measurement performed with a small-angle scattering trigger in the region of overlap of the two triggers. The measurement of the cross-section ratio allowed an estimate of the Gottfried integral in the available kinematical range. Our result was found to be consistent with the measurement reported by the New Muon Collaboration.

## Dedication

*To my parents*

*and my sister, Malika*

# Acknowledgments

Without the work and contribution of many, Experiment 665 would not have become a reality. Without the help of many, this work would not have been possible. These acknowledgements, necessarily short, cannot do justice to all those to whom I am indebted in the accomplishment of this endeavour .

Phillip Steinberg was, until 1987, my advisor. His premature demise has been a loss, as a friend and as a guide. George Snow, who then took over the difficult task of advising a stubborn student who was never satisfied until things looked perfect, is to be thanked for his advice, his infinite patience and the numerous times he went beyond his duty as an advisor to help me.

During all the years I spent at Fermilab, Shuichi Kunori taught me the Art of Data Analysis. There is a world between knowledge acquired in books

and the actual doing of, the *experience* about, physics. With infinite patience, he provided constant guidance and suggestions in our work. For this and his friendship, I thank him.

I wish to thank Andris Skuja who shared his experience in experimental High Energy Physics; although it was not his duty, he took the time to read this work and make valuable suggestions.

I wish to thank Hugh Montgomery, who has been a constant source of suggestions and help. He never missed an opportunity to curb our skeptical pessimism and make us see the diamond in the mud. This work owes much more to him than can be rendered in these few lines.

Among all E665 collaborators, my fellow students deserve a special place. Borne out of shared difficulties, a spirit of camaraderie grew stronger as years went by and friendship, transcending linguistic and cultural barriers, developed.

I wish to thank Michael Schmitt, who, in the last leg of my journey through data analysis, provided moral support, suggestions and help. This shall not be forgotten, nor shall his contribution to the experiment be forgotten.

I wish to thank Uwe Ecker, whose friendship throughout his stay at Fermilab helped make our work a more enjoyable experience.

I wish to thank Alejandro Salvarani, whose contribution to the track fitting code has been essential in the analysis of our data, who never hesitated to help

and listen during all the years that we spent at Fermilab.

I wish to thank John Ryan for helping bring the reconstruction code to a level where it could be used to produce physics results. He was a colleague but nevertheless a friend.

I wish to thank Stephen O'Day for his contribution to the Monte Carlo work. And for his friendship.

I wish to thank Anwar Bhatti for taking care of some of the most tedious aspects of the software development.

I wish to thank Douglas Jansen for his contribution to the pattern recognition

I wish to thank David Jaffe for useful suggestions and comments.

I wish to thank Detlev Hantke for accepting to take over the responsibility of maintaining the first-stage Monte Carlo.

And many more people, who in one fashion or another helped this experiment, are to be thanked. I wish to thank Mark Adams, Don Geesaman, Clive Halliwell, Harry Melanson, Wolfgang Wittek and Steve Wolbers for for the active part they took in the experiment. I wish to thank Tom Kirk for having got E665 off the ground. His leaving the experiment in order to have the time to take greater responsibilities was a great loss for our collaboration.

Many aspects of this analysis have been made possible by the use of CERN software packages. We thank CERN for letting us use HBOOK4, PAW, GEANT and other utility routines from the CERN software library.

Being away from the University of Maryland did not make the handling of administrative matters trivial. And without the diligence of thoughtfulness of many at College Park, I would probably have spent more time arguing with the administration than working on E665. For this reason, I wish to thank Sibylle Sampson, Jane Hessing, Sally Megonigal and Brenda Dunn for taking care of all those details without which there is nothing gets accomplished.

I wish to thank Tristan Hübsch and his wife Dunya. Neither one were involved in Experiment 665, but this is immaterial. In the life beyond Experiment 665, there is so much that I owe them that no words can possibly repay my debt. But let this be a small token of my gratitude.

Finally, I wish to thank my parents for their love and support; my sister Malika for her encouragement while I was away from home. To them, I dedicate this thesis. Since English is not their mother tongue, I shall write this that concerns them in a language they know. Je remercie mes parents pour leur amour et leur soutien moral; je remercie Malika ma sœur pour m'avoir constamment encouragé durant la rédaction de cette thèse, alors que j'étais si loin de ma famille. A mes parents, qui ont cru en moi, et à Malika, je dédie cette thèse.

This work was funded by the United States Department of Energy.

# Table of Contents

**Introduction** . . . . . 1

**Chapter 1 Lepton Deep Inelastic Scattering : a Survey** . . . . 4

**1.1** Historical overview . . . . . 4

**1.1.1** From atoms to nuclei . . . . . 4

**1.1.2** From nucleon to quarks . . . . . 8

**1.2** Deeply Inelastic Scattering and the Structure of the Nucleon 10

**1.2.1** Kinematical variables of DIS . . . . . 10

**1.2.2** QCD and the quark-parton model . . . . . 12

**1.2.3** The Parton Model . . . . . 21

**1.2.4** Sum rules . . . . . 22

**1.2.5** Scaling violations . . . . . 25

**1.2.6** $F_2^n/F_2^p$ . . . . . 26

**Chapter 2 Experiment 665 at Fermilab** . . . . . 28

**2.1** Generalities . . . . . 28

**2.2** The muon beamline and the beam spectrometer . . . . . 29

**2.3** Targets . . . . . 32

**2.4** Forward spectrometer . . . . . 34

**2.4.1** Tracking system . . . . . 34

**2.4.2** Particle identification . . . . . 35

**2.5** Triggering system . . . . . 36

**2.5.1** LAT trigger . . . . . 37

**2.5.2** SAT trigger . . . . . 39

**2.6** Data-acquisition system . . . . . 40

**Chapter 3 Data analysis** . . . . . 43

**3.1** Generalities . . . . . 43

**3.2** Analysis software . . . . . 47

**3.2.1** Reconstruction software . . . . . 47

**3.2.1.1** Event splitting . . . . . 47

**3.2.1.2** Event filtering . . . . . 47

**3.2.1.3** Pattern recognition . . . . . 49

**3.2.1.4** Track fitting . . . . . 50

**3.2.1.5** Muon identification . . . . . 51

**3.2.1.6** Vertex search . . . . . 52

**3.2.2** Simulation software . . . . . 55

**3.3** Beam normalisation . . . . . 76

**3.4** Trigger efficiency and trigger acceptance . . . . . 82

**3.4.1** Trigger acceptance . . . . . 82

**3.4.2** Trigger efficiency . . . . . 88

**3.5** Software Efficiency . . . . . 108

**3.5.1** Method . . . . . 108

**3.5.2** Filter efficiency . . . . . 108

**3.5.3** Pattern-recognition efficiency . . . . . 109

**3.5.4** Muon-matching efficiency . . . . . 113

**3.5.5** Vertex-reconstruction efficiency . . . . . 114

**3.5.6** Other issues in reconstruction efficiency . . . . . 114

**3.5.7** Corrections and systematic uncertainties . . . . . 115

**3.6** Issues in spectrometer calibration . . . . . 116

**3.7** Issues in kinematical resolution . . . . . 118

**3.8** Background estimate . . . . . 122

**3.9** Deuterium-target purity . . . . . 126

**3.10** Data stability . . . . . 128

**3.11** Fermi-motion correction . . . . . 129

**3.12** Radiative corrections . . . . . 134

**3.12.1** Lepton corrections . . . . . 136

**3.12.2** Hadron-vertex corrections . . . . . 138

**3.12.3** Electroweak correction . . . . . 138

**3.12.4** Overall radiative corrections . . . . . 138

**3.13** Analysis of the systematic uncertainties . . . . . 140

**3.14** Summary . . . . . 143

**Chapter 4 Final results** . . . . . 147

**Conclusion** . . . . . 156

**Appendix A** Statistical methods . . . . . 157

**References** . . . . . 166

## List of Tables


1.1. Quark quantum numbers . . . . . 14

2.1. Composition of deuterium target . . . . . 34

3.1. LAT correlation tables . . . . . 90

3.2. Electronic efficiency of the large-angle trigger . . . . . 94

3.3. $\mu_a.\mu_b$ efficiency . . . . . 96

3.4. Overall $\epsilon_3$ using SMS latches for various cuts . . . . . 100

3.5. SMS1 latch efficiencies in quadrant 3 . . . . . 100

3.6. SMS1 latch efficiencies in quadrant 1 . . . . . 101

3.7. Trigger efficiency as a function of $x_{bj}$ using SMS latches . . . . 101

3.8. Trigger efficiency as a function of $x_{bj}$ . . . . . 106

3.9. Trigger corrections to cross-sections . . . . . 107

3.10. Reconstruction efficiency as a function of $x_{bj}$ . . . . . 116

3.11. Ratio of deuterium to hydrogen $\mu e$ cross-sections . . . . . 142

3.12. Correction factors . . . . . 144

4.1. Final results . . . . . 151

## List of Figures


**1.1** One-photon exchange diagram . . . . . 10

**1.2** Absorption of virtual photon by parton . . . . . 17

**1.3** Effect of Gaussian momentum on scaling variable $x_{bj}$ . . . . . 19

**1.4** QCD splitting functions . . . . . 25

**2.1** Synoptic view of the Muon beamline . . . . . 29

**2.2** Top view of the beam tagging system . . . . . 31

**2.3** SBT counters . . . . . 32

**2.4** Target vessel for $H_2$ and $D_2$ . . . . . 33

**2.5** Top view of the E665 forward spectrometer . . . . . 35

**2.6** Array structure of the muon scintillator planes . . . . . 38

**2.7** Muon system . . . . . 39

**2.8** Array structure of the SMS planes . . . . . 40

**2.9** Logical diagram of the LAT trigger . . . . . 41

**2.10** Synoptic diagram of the online data acquisition system . . . . 42

**3.1** Kinematical quantities in Monte Carlo and data . . . . . 59

**3.2** Kinematical angles in Monte Carlo and data . . . . . 60

**3.3** Reconstructed vertex in Monte Carlo and data . . . . . 61

**3.4** Vertex fit in Monte Carlo and data ($H_2$). . . . . 62

**3.5** Vertex fit in Monte Carlo and data ($D_2$) . . . . . 63

**3.6** Number of planes on muon track in Monte Carlo and data ($H_2$). . 64

**3.7** Number of planes on muon track in Monte Carlo and data ($D_2$). . 65

**3.8** Muon position at PCV in Monte Carlo and data . . . . . 66

**3.9** Muon position at PC in Monte Carlo and data . . . . . 67

**3.10** Muon position at PCF5 in Monte Carlo and data . . . . . 68

**3.11** Muon position at DCA in Monte Carlo and data . . . . . 69

**3.12** Muon position at DCB in Monte Carlo and data . . . . . 70

**3.13** Muon position at SPM1 in Monte Carlo and data . . . . . 71

**3.14** Muon position at SPM4 in Monte Carlo and data . . . . . 72

**3.15** Distance of muon to SMS veto in Monte Carlo and data . . . . 73

**3.16** $n_{dof}$ for muon track in Monte Carlo and data . . . . . 74

**3.17** RBEAM prescale powers . . . . . 78

**3.18** Beam losses . . . . . 79

**3.19** RBEAM phase space . . . . . 81

**3.20** LAT acceptance . . . . . 84

**3.21** Superveto acceptance . . . . . 86

**3.22** Venn diagrams of LAt-efficiency measurement . . . . . 89

**3.23** $y_\mu$ and $z_\mu$ dependence of LAT electronic efficiency . . . . . 92

**3.24** SMS1 latch efficiency . . . . . 97

**3.25** SMS4 latch efficiency . . . . . 98

**3.26** Self-veto insensitivity of the LAT. SMS latches . . . . . 99

**3.27** Self-veto insensitivity of the LAT in first quadrant . . . . . 100

**3.28** Self-veto insensitivity of the LAT . . . . . 103

**3.29** Ratio of trigger efficiencies . . . . . 104

**3.30** Time-dependence of $\varepsilon_3$ . . . . . 105

**3.31** Reconstruction efficiency as a function of $y_\mu$ and $z_\mu$ . . . . . 110

**3.32** $y_\mu$ resolution . . . . . 111

**3.33** Reconstruction efficiency as a function kinematical variables . . 112

**3.34** Neutron-to-proton cross-section ratios . . . . . 114

**3.35** Impact of beam energy mis-measurement on cross-sections . . . 117

**3.36** Impact of beam energy mis-measurement on cross-sections . . . 118

**3.37** $x_{bj}$ resolution . . . . . 119

**3.38** $Q^2$ resolution . . . . . 120

**3.39** Empty-target vertex distribution . . . . . 124

**3.40** Distributions of empty-target events . . . . . 126

**3.41** Time-dependence of uncorrected event yield . . . . . 129

**3.42** Time-dependence of corrected event yield . . . . . 130

**3.43** Time-dependence of $Q^2$ . . . . . 131

**3.44** Time-dependence of $\nu$ . . . . . 132

**3.45** Time-dependence of $x_{bj}$ . . . . . 133

**3.46** Radiative-correction diagrams . . . . . 134

**3.47** Radiative correction for $H_2$ and $D_2$ . . . . . 139

**3.48** $x_{bj}$ distribution of $\mu e$ events in LAT . . . . . 141

**4.1** Hydrogen and deuterium cross-sections . . . . . 148

**4.2** Neutron-to-proton cross-section ratios. . . . . 149

**4.3** LAT and SAT cross-section ratios . . . . . 150

**4.4** Deuterium $F_2$ structure functions. . . . . 151

# Introduction

The purpose of this work is to make a modest contribution to our knowledge of the constituents of matter by presenting measurements obtained from scattering 490 GeV/c muons off nucleons. The experiment was carried out at Fermi National Accelerator laboratory from 1987 to 1988. More specifically, we shall investigate the difference between the quark content of the proton and the neutron. These two particles, known collectively as nucleons, are the building blocks of nuclei. Their mass, size, charge, and magnetic moment have been known for some time, but experiments in the last 25 years revealed that, unlike the electron for instance, they have an internal structure. The latter is currently understood in the framework of a model and a field theory. The model is the quark-parton picture, the field theory is Quantum Chromodynamics (QCD). The quark-parton model postulates that nucleons are composed of "elementary particles" called quarks. The field theory assumes that the Lagrangian $L$ describing the nuclear interaction between quarks is given by :

$$L = \overline{\psi}_f^{\alpha}(i\gamma_\mu\partial^\mu - m_f)\psi_f^{\alpha} + g_s\overline{\psi}_f^{\alpha}\gamma_\mu\left(\frac{\lambda_i}{2}\right)_{\alpha\beta}\psi_f^{\beta}G_i^{\mu}(x) - \frac{1}{4}F_{\mu\nu}^{i}(x)F_i^{\mu\nu}(x)$$

$$F_{\mu\nu}^{i} = \partial_\mu G_\nu^i(x) - \partial_\nu G_\mu^i(x) + g_s f_{ijk}G_\mu^j(x)G_\nu^k(x)$$

where $\psi_f^a$ are the quark fields and $G_\mu^i$ the gluon fields. It postulates that the quark fields $\psi_f$ belong to the fundamental (three-dimensional) representation of the SU(3) flavour group. The $\lambda_i$ are the Gell-Mann matrices and form a basis of the Lie algebra of SU(3). The fields $G_\mu^i$ belong to the eight-dimensional representation of the SU(3) Lie algebra and are associated with the gluons, the mediators of the strong force, the strength of which is given by $g_s$ in the previous equation. Deviations from the predictions of the quark-parton model per se, where nucleon quarks are assumed to be free, are interpreted as manifestations of QCD corrections. In deeply inelastic muon scattering, the comparison between QCD predictions and experimental measurements is rendered difficult by the fact that, in general, experiments access kinematical regions (low $Q^2$) where QCD perturbative expansions break down. The high-$Q^2$ range, where it is believed that QCD expansions are valid, suffers, from an experimental standpoint, from low statistics, due to the $1/Q^4$-dependence characterising the charged lepton scattering cross-section.

Our results on the ratio of the neutron-to-proton deeply inelastic cross-sections do not validate or invalidate QCD, but test one aspect of the quark-parton model, namely the identity of the parton distributions in each nucleon for low values of the scaling variable $x_{bj}$. This scaling variable can be interpreted, as we shall see, as the fraction of the nucleon momentum carried by the parton in the so-called infinite momentum frame. The lack of statistics near $x_{bj} = 1$ precludes any statement from this experiment as to the limit reached by this cross-section ratio when $x_{bj}$ approaches 1, but other experiments have shown that the probablity of an up quark in the neutron being near $x_{bj} = 1$ is much less than the comparable probability in a proton.

Our work will be divided as follow. In the next chapter, we shall present a brief overview of the historical landmarks that led to our current understanding of the structure of the nucleon, followed by an introduction to the structure functions describing the internal structure of the nucleon, an outline of the

quark-parton model and a brief overview of the features of QCD relevant to lepton scattering. The spectrometer used by E665 will be described in chapter 2. We shall not go into the details of this apparatus, since it has been described at some length elsewhere, but rather we shall emphasise those aspects of our detector which are crucial to the extraction of our results. The limitations imposed by the spectrometer and systematic uncertainties thereof will be the subject of Chapter 3, where we shall present the analysis of the data that allowed us to extract the aforementioned ratio. The significance of our results will then be explored in chapter 4 and comparisons with measurements done prior to those obtained here will be made.

Throughout our analysis, we shall use a right-handed coordinate system where the x-axis points along the nominal beam direction (to the north) and the z-axis is vertical, oriented upward. The y-axis points therefore to the west. Chamber and hodoscope planes are characterised by the coordinate they measure. A $z-$ plane, therefore measures a $z-$ coordinate, which means that the corresponding wires or hodoscopes are parallel to the $y-$ axis. Similarly considerations apply to $y-$ planes.

When there is no ambiguity, we shall denote a differential cross-section by $\sigma$ when it is immaterial to which kinematical cell we refer.

# *Chapter 1*

# Lepton Deep Inelastic Scattering : a Survey

## 1.1 Historical overview

### *1.1.1 From atoms to nuclei*

Until 1911, it was thought that atoms were uniformly-charged balls in which electrons were located. This picture of the structure of matter came to be known as the Thomson model of the atom. In 1909, Hans Geiger, Ernst Marsden and E. Rutherford conducted experiments in which $\alpha$-particles, of an energy between 4 and 9 MeV were scattered off thin gold foils. The measured cross-section was inconsistent with that predicted by the Thomson model. To explain the experimental results, Rutherford, in 1911, conjectured that most of the mass of the atom was concentrated in a very small, positively charged nucleus of radius less than $10^{-12}$ cm around which electrons orbit. The cross-section calculated by Rutherford using this model agreed well with the observed cross-section.

It is an elementary exercise, using Newtonian mechanics and Coulomb's law to show that, under the assumption that the nucleus does not recoil against

the incident particle, the expression of the differential scattering cross-section is given by :

$$\frac{d\sigma}{d\theta} = \frac{1}{4}\left(\frac{zZe^2}{8\pi\epsilon_0 E}\right)^2 \frac{1}{\sin^4\frac{\theta}{2}} \tag{1.1}$$

where $\theta$ is the scattering angle between the incident $\alpha$-particle and the outgoing $\alpha$-particle, $z$ the charge of the $\alpha$-particle, in units of the proton charge, $e$ ($z = 2$), $Z$ the charge of the target nucleus and $E$ the kinetic energy of the incident $\alpha$-particle.

At small values of the impact parameter (corresponding to large values of the scattering angle), the interaction between the incident $\alpha$-particle and the target ceases to be purely electromagnetic, the short-ranged, attractive strong interaction taking over, causing the $\alpha$-particles to be absorbed and therefore the measured cross-section to decrease faster with $\theta$ than described by Eq. 1.1 (Valentin, 1981). A probe that did not interact strongly with the nucleus was desirable. Electrons, undergoing purely electromagnetic interactions were suggested in 1948 (Rose, 1948). As early as 1929, Mott (Mott, 1929) calculated the cross-section of elastic electron scattering off a point, spinless nucleus, taking into account the spin of the electron. The expression for the differential cross-section is approximately given by :

$$\left(\frac{d\sigma}{d\theta}\right)_M = \left(\frac{zZe^2}{8\pi\epsilon_0 E}\right)^2 \frac{\cos^2\frac{\theta}{2}}{\sin^4\frac{\theta}{2}} \tag{1.2}$$

with the same notations as in Eq. 1.1.

It is important to realise that the Mott cross-section is derived under the assumption that the nucleus is a point particle. If one assumes that its charge has a spatial density $\rho(\vec{r})$, then the cross-section becomes

$$\frac{d\sigma}{d\theta} = \left(\frac{d\sigma}{d\theta}\right)_M \left|F(q^2)\right|^2 \tag{1.3}$$

The quantity $F(q^2)$, where $q^2$ is the squared magnitude of the three-momentum transfer of the electron, is the Fourier transform of the charge distribution $\rho(\vec{r})$ and is called the electric form factor of the nucleus. Specifically, if the charge distribution has spherical symmetry, then

$$F(q) = \frac{4\pi}{q} \int_0^{+\infty} r\rho(r) \sin qr \, dr \tag{1.4}$$

In the 1950's, experiments at Darmstadt, Kartov, Orsay, Yale, and particularly at SLAC (Hofstadter,1964) were undertaken to determine the charge distributions of various nuclei by measuring the electron elastic-scattering cross-section. The main results obtained at that time were that the charge distributions of spherical nuclei having $A > 30$ could be represented by Fermi functions of the form

$$\begin{aligned} \rho_F &= \frac{\rho_0}{1 + e^{\frac{r-c}{a_0}}} && \text{two-parameter Fermi function} \\ \rho_{F'} &= \rho_0 \frac{1 + \frac{wr^2}{c^2}}{1 + e^{\frac{r-c}{a_0}}} && \text{three-parameter Fermi function} \end{aligned} \tag{1.5}$$

and $c$ (which, in the case of the two-parameter Fermi distribution, is the half-maximum radius) was found to be nearly proportional to $A^{1/3}$.

The case of the proton and the neutron is particularly interesting. Rosenbluth showed (Rosenbluth, 1950) that the cross-section of scattering of an electron off a spin-1/2 object is given by

$$\frac{d\sigma}{d\theta} = \left(\frac{d\sigma}{d\theta}\right)_M \left( \left( F_1^2(q^2) + \frac{\kappa^2 q^2}{4M^2} F_2^2(q^2) \right) + \frac{q^2}{2M^2} \left( F_1(q^2) + \kappa F_2(q^2) \right)^2 \tan^2 \frac{\theta}{2} \right) \tag{1.6}$$

Here, $\kappa = 1.79$ for the proton and $\kappa = -1.91$ for the neutron, $q^2$ is the square of the four-momentum transfer and $M$ is the mass of the target nucleon. $F_1(q^2)$ and $F_2(q^2)$ are called the Pauli-Dirac form factors. Eq. 1.6, unlike Eq. 1.3,

takes into account not only the spatial charge distribution of the nucleon, but also its magnetic distribution through the phenomenological form factors $F_1$ and $F_2$. In fact, under the assumption that the contribution comes from the charge and current densities of the nucleus, $F_1$ and $F_2$ can be related to the Sachs electric and magnetic form factors $G_E$ and $G_M$ by

$$G_E(q^2) = F_1 + \frac{\kappa q^2}{4M^2} F_2$$

$$G_M(q^2) = F_1 + \kappa F_2$$

It was found experimentally that the following relations hold between the electric and magnetic form factors :

$$G_{E_p} = \frac{G_{M_p}}{\mu_p} = -\frac{G_{M_n}}{\mu_n}$$

$$G_{E_n} = -\mu_n \frac{\frac{q^2}{4M^2}}{1 + 5.6\frac{q^2}{4M^2}} G_{E_p}$$

and futhermore $G_{E_p}$ had a dipole dependence on $q^2$ of the form

$$G_{E_p} = \frac{1}{\left(1 + \frac{q^2}{0.761}\right)^2}$$

where $q^2$ is expressed in $GeV^2/c^2$ and the indices $n$ and $p$ refer to the neutron and the proton respectively.

Thus, by the mid 1960's, *elastic* electron scattering experiments had provided valuable information on the spatial extent and the electromagnetic properties of the nucleus. But to those reductionists who would not admit that the nucleon was an elementary particle, elastic scattering was silent as to a possible sub-structure of the nucleon.

### *1.1.2 From nucleon to quarks*

The electron-scattering experiments performed until the mid-1960s were termed elastic. The nucleus remains intact or at worst, only low energy resonances were excited.

In 1968, the availability of a 20 GeV electron-beam at SLAC made it possible to probe the nuclear structure in the *inelastic* region. In such a kinematic regime, the mass of the hadronic final state is greater than that of the target nucleus. The cross-section for such a process, can be expressed in terms of two form factors $F_1$ and $F_2$ (different from those of Eq. 1.6) called *structure functions*. Unlike the elastic form factors, which depend only on the square of the four-momentum transfer, the inelastic structure functions depend a priori on two independent Lorentz invariants characterising the final state of the interaction. These can be taken as the square of the four-momentum transfer $Q^2$ and the energy transfer $\nu$. Measurements were reported on electron-proton inelastic scattering for beam energies between 7 and 17 GeV and four-momentum transfers $Q^2$ up to 7.4 GeV (Bloom, 1969). The striking result was that the structure functions have almost no dependence on $Q^2$ and depend only on the ratio $x_{bj} = Q^2/2M\nu$. This experimental result came to be known as scaling. An explanation of the phenomenon was given by Bjorken (Bjorken,1969). Using the infinite-momentum frame and assuming that the commutator of the hadronic currents vanishes outside the lightcone, Bjorken showed that the inelastic form factors, in the limit of large $Q^2$ and large energy transfer $\nu$ , with $Q^2/2\nu$ fixed, did not depend on $Q^2$ but rather on a single variable $x_{bj} = Q^2/2M\nu$. The idea of scaling was also suggested by Feynman (Feynman,1969), based on the idea of the existence of partons in the nucleons.

A few years before the experimental results obtained at SLAC, Gell-Mann and Zweig, in order to explain the "hadronic" table, postulated the existence of quarks, based on an SU(3) symmetry group.

In 1971, Kuti and Weisskopf (Kuti and Weisskopf,1971), combining the

hypothesis of quarks, formulated earlier by Gell-Mann and Zweig and Feynman's idea of partons suggested that most of the results from deep-inelastic scattering experiments could be explained on the the basis of the *quark-parton model.* In such a model, it is assumed that the nucleon is composed of three valence quarks and a core of an indefinite number of quark-antiquark pairs. This model reproduced most of the results of deep-inelastic scattering, including scaling, with one exception. It predicted that at high $x_{bj}$ the ratio of the neutron structure function to that of the proton should go to 2/3. Experimentally, it appears that this ratio is approaching 1/4.

To map out the behaviour of the structure functions over a wider $Q^2$ range and determine to which level scaling holds, it is necessary to make use of probes of higher energy. When electrons are accelerated, they lose energy through synchrotron radiation. The smaller the mass, the higher the synchrotron losses. The way out of this limitation is the use of a heavier beam particle, with the same properties as the electron. The muon turned out to be the most obvious candidate. Its mass is about 200 times the mass of the electron, but otherwise behaves identically to the electron in interactions. And so the 1970's saw the birth of *high-energy muon* deep-inelastic scattering experiments. In addition to smaller radiative contributions to the deeply inelastic cross-section, muons are easier to identify than electrons among all the particles produced in the interaction. These advantages are however offset by two factors. On the one hand, it is difficult to produce muon beams with intensities comparable to those available at electron machines, and on the other hand, the spatial extent of the beam is fairly broad in comparison to that of an electron beam. This imperfect collimation of the beam results in an undesirable "halo" accompanying a useful beam core. On this basis, it is traditional to divide muon experiments into two generations. In the first generation of experiments, such as CHIO, which can be said to have begun with the operation of the 270-GeV muon beam at Fermilab, emphasis was on high incident muon energy at the cost of good collimation of the beam. In the second generation, halo-reduction schemes led

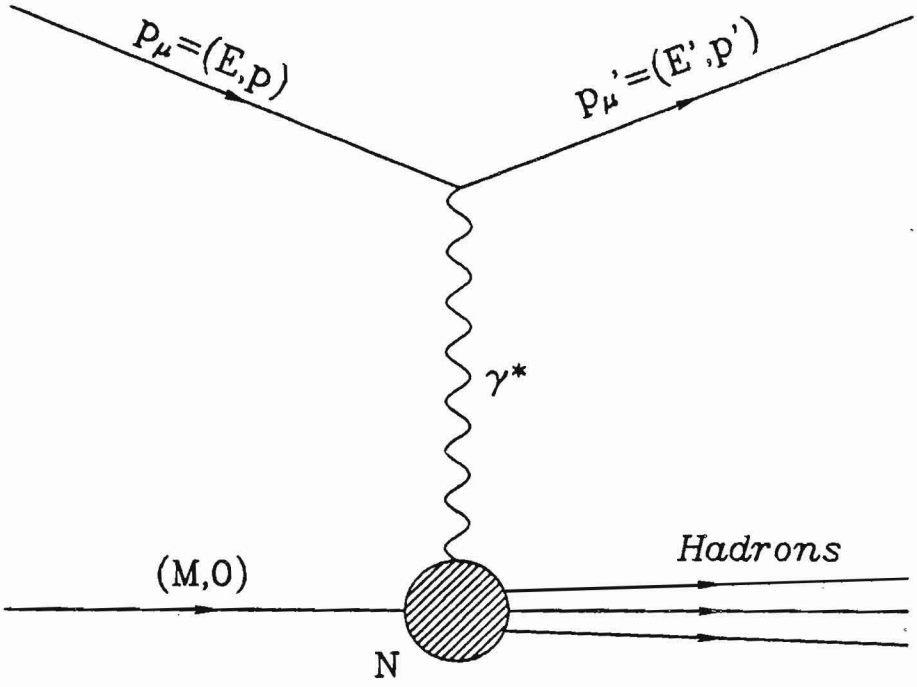


**One-photon exchange diagram.**
**Fig. 1.1**

to higher-quality muon beams, such as the 280-Gev beam used at CERN by the European Muon Collaboration (EMC) and the Bologna-Cern-Dortmund-Moscow-Saclay group (BCDMS) and the 490-GeV beam used at Fermilab by the E665 collaboration. Out of these experiments came the measurements of the structure functions of the neutron and the proton, the study of the A-dependence of these structure functions (EMC effect) and the analysis of hadronic final states.

It should not be forgotten that deeply inelastic neutrino scattering experiments have produced important results on structure function measurements. For a review on this topic, we refer to (Diemoz et al.,1985)

## 1.2 Deeply Inelastic Scattering and the Structure of the Nucleon

### *1.2.1 Kinematical variables of DIS*

Before we proceed to outline our current understanding of the structure of the nucleon, it is worth presenting the relevant kinematical variables used to describe muon scattering. To lowest order, this process is described by the one-photon exchange diagram of Fig. 1.1. A muon, having four-momentum $p_\mu$ exchanges a virtual photon of four-momentum $q$ with a nucleon of four-momentum $P$ and emerges with momentum $p'_\mu$. In such a process, it is traditional to use the following Lorentz scalars :

$$Q^2 = -(p'_\mu - p_\mu)^2 = -q^2$$

$$\nu = \frac{p.q}{M}$$

$$x_{bj} = \frac{Q^2}{2M\nu}$$

$$y = \frac{q.P}{p_\mu.P}$$

$$W^2 = (P+q)^2 = M^2 + 2M\nu - Q^2$$

In the laboratory frame, that is, in the frame of reference where the target is at rest, $\nu$ is simply the energy lost by the muon and $y$ is the ratio of that energy lost, $\nu$, to the energy of the incident muon. $W$ is the invariant mass of the hadronic final state. The meaning of the scaling variable $x_{bj}$ will be discussed in the next section.

The most general expression for the cross-section for unpolarised targets and beams, neglecting the lepton mass, is given by

$$\frac{d\sigma}{dQ^2 dx_{bj}} = \frac{4\pi\alpha^2}{Q^2 x_{bj}}\left(y^2 x_{bj} F_1(x_{bj}, Q^2) + (1 - y - M x_{bj} y/2E) F_2(x_{bj}, Q^2)\right)$$

The functions $F_1$ and $F_2$ describe phenomenologically the hatched blob of Fig. 1.1 and represent the unknown dynamics of the nucleon with which the muon interacts electromagnetically. This dynamics is governed, on the one

hand by the constituents of the nucleons, and on the other hand by the nature of their mutual interactions. It is clear that if these were known it would be possible, at least theoretically, to calculate $F_1$ and $F_2$. This however is not the case. $F_1$ and $F_2$ are determined experimentally, and from such measurements, one attempts to gain some insight into the dynamical structure of the nucleon. The situation is similar to that of electron elastic scattering, where one measures the electromagnetic form factors and infers the charge and current distribution of the nucleon.

### *1.2.2 QCD and the quark-parton model*

The earliest attempt made to understand the behaviour of the strong force was that of Heisenberg with the concept of isospin. It had been known for a while from *pp* and *pn* scattering data and the energy levels of mirror nuclei that, as far as the strong interaction is concerned, the proton and the neutron interact with similar strength. Hence it is possible to regard them as two different states of the same particle, the *nucleon.* The state space of the nucleon should then be taken to be $\mathcal{W} \otimes \mathcal{S} \otimes \mathcal{I}$, where $\mathcal{W}$ is the spatial part of the state space, S its spin part and $\mathcal{I}$ is a two-dimensional vector space, with a basis given by $|p>, |n>$. If the strong force does not distinguish between the proton and the neutron, then its Hamiltonian commutes with all operators acting on $\mathcal{I}$ and in particular with the unitary transformations acting on $\mathcal{I}$. The latter form a three-dimensional Lie group called SU(2), and the space $\mathcal{I}$ carries a two-dimensional representation of SU(2). Furthermore, the generators of SU(2) form a set of conserved observables, and we can choose three such generators :

$$I_3 = \frac{1}{2}\begin{pmatrix} 1 & 0 \\ 0 & -1 \end{pmatrix} \quad I^+ = \begin{pmatrix} 0 & 1 \\ 0 & 0 \end{pmatrix} \quad I^- = \begin{pmatrix} 0 & 0 \\ 1 & 0 \end{pmatrix}$$

and the Casimir operator $I^2 = I^+I^- + I_3^2 - I_3$ acting on $|p>$ and $|n>$ gives

$$I^2|p>=\frac{1}{2}(\frac{1}{2}+1)|p>$$

$$I^2|n>=\frac{1}{2}(\frac{1}{2}+1)|n>$$

In analogy with spin, one can therefore attribute isospin $I = 1/2$ to the nucleon, $|p>$ having $I_3 = 1/2$ and $|n>$, $I_3 = -1/2$. The charge operator $Q$ is given by

$$Q = I_3 + \frac{1}{2}$$

Extending this to all other hadrons, one can classify them into isospin multiplets. For instance, the pions form an isospin triplet ($I = 1$) under SU(2). But it was realised that some processes involving heavier hadrons discovered in the post World War II era, even though conserving isospin, did not occur. Gell-Mann and Nishijima postulated that in addition to isospin, another quantum number (called strangeness) had to be conserved. This led to enlarging the original isospin group SU(2) to SU(3). The fundamental representation of SU(3) is three-dimensional and has a basis of three state vectors corresponding to particles named quarks and denoted by $u$, $d$ and $s$ (respectively up, down and strange).In this classification, SU(3) is referred to as flavour SU(3). The new relation between the charge operator $Q$ and $I_3$ involves a new quantity $Y$ called hypercharge.

$$Q = I_3 + \frac{1}{2}Y$$

where, in the fundamental representation of SU(3)

$$I_3 = \frac{1}{2}\begin{pmatrix} 1 & 0 & 0 \\ 0 & -1 & 0 \\ 0 & 0 & 0 \end{pmatrix} \quad Y = \frac{1}{3}\begin{pmatrix} 1 & 0 & 0 \\ 0 & 1 & 0 \\ 0 & 0 & -2 \end{pmatrix}$$

**Table 1.1**

| | Charge | Isospin | $I_3$ | Baryon number | Strangeness |
|---|---|---|---|---|---|
| u | $\frac{2}{3}$ | $\frac{1}{2}$ | $\frac{1}{2}$ | $\frac{1}{3}$ | 0 |
| d | $-\frac{1}{3}$ | $\frac{1}{2}$ | $-\frac{1}{2}$ | $\frac{1}{3}$ | 0 |
| s | $-\frac{1}{3}$ | 0 | 0 | $\frac{1}{3}$ | $-1$ |

Similarly, the conjugate of the fundamental representation of SU(3) (denoted $\overline{3}$ has a basis $(\overline{u}, \overline{d}, \overline{s})$ corresponding to the antiparticles of $(u, d, s)$. Hadrons are then built from tensorial products of the fundamental representation of SU(3) and its conjugate, and in order to reproduce their correct quantum numbers, quarks are assigned charge,isospin,baryon number and strangeness as given in Table 1.1.

Mesons are supposed to belong to the $3 \otimes \overline{3}$ representation and baryons to the $3 \otimes 3 \otimes 3$ representation of SU(3). The decomposition of these tensorial representations into irreducible representations gives :

$$3 \otimes \overline{3} = 1 \oplus 8$$

$$3 \otimes 3 \otimes 3 = 1 \oplus 8 \oplus 8 \oplus 10$$

For instance the spin-0 octet of $3 \otimes 3$ contains $\pi^0, \pi^+, \pi^-, K^0, K^+, K^-, \overline{K^0}$. The singlet representation contains the $\eta'$ particle. The spin-1/2 octet contains among other particles the proton and the neutron. The spin-3/2 decuplet representation contains the $\Omega^-$, which at the time flavour SU(3) was formulated was not known. It was discovered in 1964.

If flavour SU(3) were exact, then the multiplets would be degenerate. This is clearly not the case, since the particles have different masses. It might be tempting to attribute the removal of degeneracy to the electromagnetic inter-

action, but this does not work and for more details we refer to (Gasser and Leutwyler,1982). Originally Gell-Mann and Okubo assumed an octet component to the Hamiltonian of the strong interaction, which lead to a formula relating the masses of particles belonging to a given multiplet (Gell-Mann Okubo formula). Baryons are made up of three quarks and mesons of a quark-antiquark pair. But since quarks are spin 1/2 particles, it is necessary to assume that they possess an additional degree of freedom, in order to respect the Pauli principle. This new quantum number is now called colour. Later, the measurement of $R$, the ratio of hadron to muon production in $e^+e^-$, confirmed that the number of colours is equal to three. Therefore, a new three-dimensional state space $\mathcal{C}$, the colour space, must be taken into account, and the full state space of a quark is given by $\mathcal{W} \otimes \mathcal{S} \otimes \mathcal{I} \otimes \mathcal{C}$. Operators acting on $\mathcal{C}$ commute with the Hamiltonian of the strong interaction and therefore $\mathcal{C}$ carries a three-dimensional representation of SU(3). The latter group is referred to as colour SU(3). However, this colour degree of freedom has never been observed in hadrons in the visible world. It is therefore postulated that quarks combine to form hadronic colour singlet states. So far, we have not discussed any dynamical aspect of hadrons, but merely presented symmetry arguments to group them into multiplets and determine their quark content. Beyond this, we need to describe quantitatively the strong force responsible for their observed behaviour. The *field* theory that attempts to do just this is Quantum Chromodynamics. Quantum Chromodynamics is a Yang-Mills gauge field theory of strong interactions the symmetry group of which is colour SU(3). The matter fields $\psi_f^\alpha$ ($1 \leq \alpha \leq 3$, for each flavour $f$) are the quark fields, belonging to the fundamental representation of $SU(3)_c$. Following the principle of gauge invariance, one declares strong interactions to be invariant under local $SU(3)_c$ transformations. This implies that the covariant derivative must depend on fields belonging to the octet representation of colour SU(3). Eight

such fields can be chosen to form a basis for the eight-dimensional representation of $SU(3)_c$ and are called gluons. In contradistinction with Quantum Electrodynamic (QED), where there is no interaction between the photons, one has to include a contribution from a self-interaction of the gluons, and the QCD Lagrangian can eventually be written as :

$$L = \overline{\psi}_f^{\alpha}(i\gamma_\mu\partial^\mu - m_f)\psi_f^{\alpha} + g_s\overline{\psi}_f^{\alpha}\gamma_\mu\left(\frac{\lambda_i}{2}\right)_{\alpha\beta}\psi_f^{\beta}G_i^{\mu}(x) - \frac{1}{4}F_{\mu\nu}^{i}(x)F_i^{\mu\nu}(x)$$

$$F_{\mu\nu}^{i} = \partial_\mu G_\nu^i(x) - \partial_\nu G_\mu^i(x) + g_s f_{ijk}G_\mu^j(x)G_\nu^k(x)$$

The non-linear character of the QCD field equations makes the task of solving them difficult. Two approaches have been taken in this direction. The first one is the application of standard perturbative techniques. In the second approach, the space-time continuum is digitised to form a lattice and the field equations are solved numerically. The limitation of this method is imposed by the CPU time needed for a fine-grained lattice that approximate the continuum reasonably well. For a review of the development and some successful predictions of QCD, we refer the reader to (Wilczek,1982). If indeed such is the structure of the nucleon, then an electromagnetic probe (electron or muon) with a high enough resolution should be able to resolve it into its quark constituents. Similarly, a weak probe, such as a neutrino should also be able to interact with the partons in the nucleons, via the exchange of a $W$ or a $Z$ boson. A naïve argument can be presented to give some justification to this quark picture. Consider the elastic scattering of an electron off a particle. The cross-section of this process is given by the Rosenbluth formula

$$\frac{d\sigma}{d\theta} = \left(\frac{d\sigma}{d\theta}\right)_M\left(\left(F_1^2(q^2) + \frac{\kappa^2 q^2}{4M^2}F_2^2(q^2)\right) + \frac{q^2}{2M^2}\left(F_1(q^2) + \kappa F_2(q^2)\right)^2\tan^2\frac{\theta}{2}\right) \tag{1.7}$$

We have seen that the form factors $F_1$ and $F_2$ or equivalently $G_E$ and $G_M$ tend to 0 as the magnitude of the four-momentum transfer $q$ goes to infinity.

Now $G_E$ and $G_M$ can be interpreted as the Fourier transforms of the electric and magnetic distributions of the aforementioned particle. The main result found at SLAC was that in *inelastic* scattering the form factors (or structure functions) are non-zero and nearly independent of $Q^2$. If they are interpreted as combinations of Fourier transforms of the charge and magnetic distributions, this means that the latter are proportional to delta functions. The scattering occurs off point-like particles. The problem is now to identify these point particles with the quarks. For this purpose, it is necessary to identify the spin and charge of these constituents and the numbers of such partons in a nucleon.

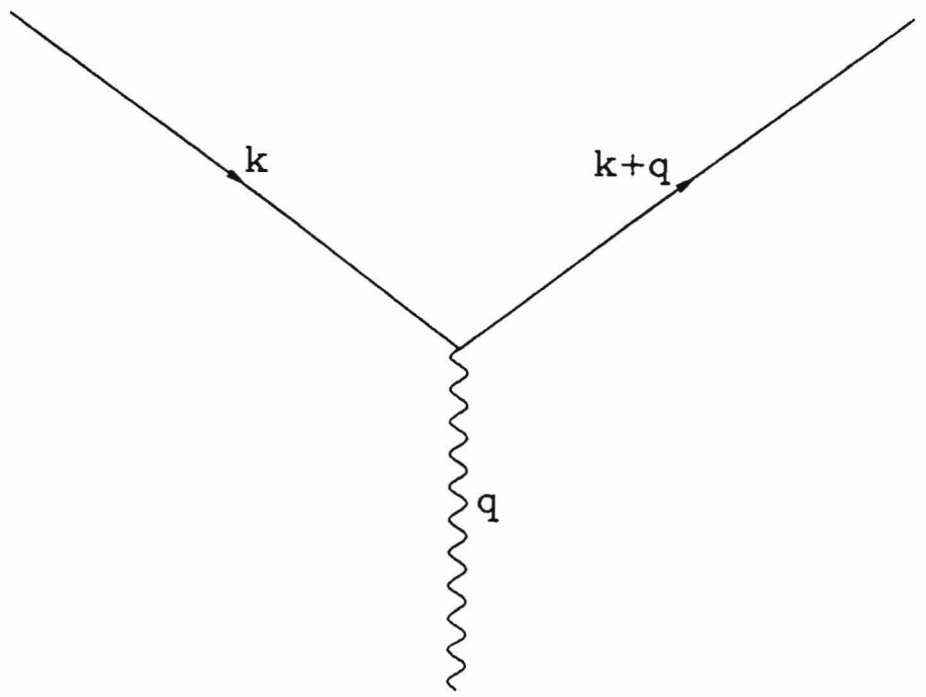


**Absorption of vitrual photon by a single parton in the laboratory frame.**
**Fig. 1.2**

Consider first a simple picture in which, in the laboratory frame, the virtual photon interacts with a parton in the nucleus (Fig. 1.2). Immediately

before the interaction, the parton has four-momentum $k$. It absorbs the virtual photon and then is scattered with four-momentum $k+q$. We assume that this first-order diagram is the only one of relevance. Let $\theta$ be the angle of the parton three-momentum with respect to the virtual-photon three-momentum and $m_p$ the mass of the parton. Then from the relation $(k+q)^2 = m_p^2$ we find that the scaling variable $x_{bj}$ obeys

$$M^2 x_{bj} - 2M(\frac{\kappa^2 \cos^2\theta}{\nu} + \sqrt{\kappa^2 + m_p^2})x + \kappa^2 \sin^2\theta + m_p^2 = 0 \qquad (1.8)$$

where $\kappa$ is the magnitude of the parton three-momentum vector. The first observation we can make is that if $\kappa = 0$, then $x_{bj}$ reduces to $\frac{m_p}{M}$. If there were three equal-mass partons in the nucleon adding up to $M$, then $x_{bj} = \frac{1}{3}$. In such a picture, the elastic scattering off a parton would be characterised by a fixed value of the scaling variable. If the parton has a non-zero momentum, the elastic scattering would still be characterised by a fixed value of $x_{bj}$, but the latter would now depend on $k$ and the energy $\nu$ of the virtual photon. If $\nu \gg \kappa$ then Eq. 1.8 reduces to

$$M^2 x_{bj} - 2M\sqrt{\kappa^2 + m_p^2}x + \kappa^2 \sin^2\theta + m_p^2 = 0 \qquad (1.9)$$

and now Eq. 1.9 shows that $x_{bj}$ is related only to the momentum of the parton. In fact, in the high $\nu$ limit,

$$x_{bj} = \frac{1}{M}(\sqrt{\kappa^2 + m_p^2} - \kappa\cos\theta)$$

Now, the interaction between the partons in the nucleon will give rise to a distribution in $k$. To get a feeling for the influence of this distribution on $x_{bj}$, let us assume that the components of $k$ follow a Gaussian distribution of mean 0 and standard deviation $\bar{\sigma}_\kappa$. The resulting $x_{bj}$ distribution will of course

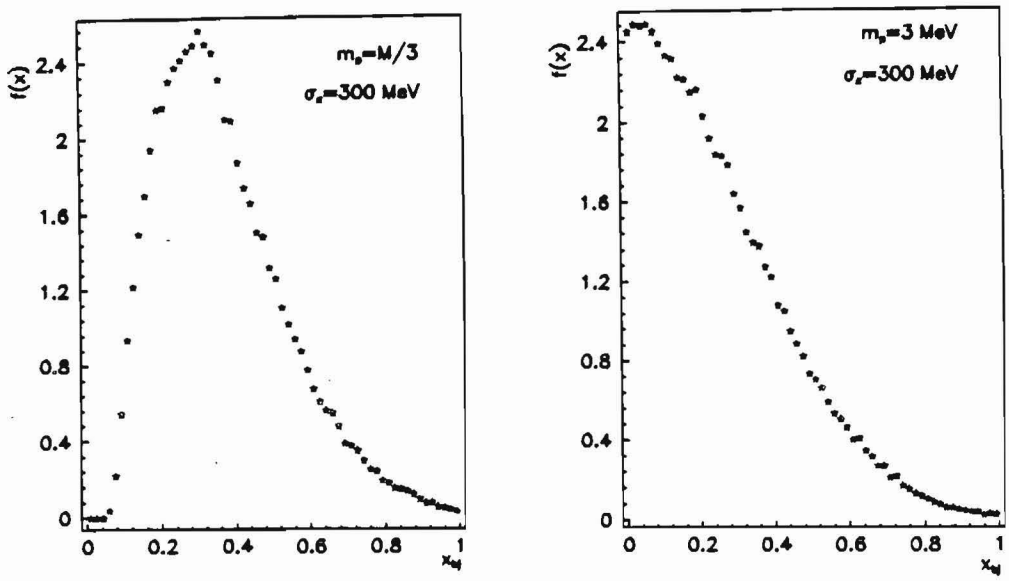


(a) (b)

**Effect of Gaussian distribution of parton momentum in the nucleon on the scaling variable.(a) Three equal-mass partons ($m_p = M/3$) and a Gaussian distribution of width 0.3 GeV. (b) Three equal-mass partons of mass 3 MeV and Gaussian of width 0.3 GeV. These plots are for illustrative purposes only.**

**Fig. 1.3**

depend on $m_p$ and $\sigma_\kappa$. Fig. 1.3 shows the effect of such a momentum smearing on the original $\delta$-function at $x_{bj} = \frac{m_p}{M}$.

It is important to realise that in such a naïve model, the main assumption is that the virtual photon has interacted with a single parton and that during the time of this interaction the nucleon system has not had time to change. In other words, we have assumed that the time it takes for the virtual photon to be absorbed by the parton is much shorter than the time scale of the dynamical evolution of the partons. There is of course no guarantee that such a hypothesis be true in the laboratory frame. Let us boost the nucleon along the direction of the virtual photon into a reference frame such that the momentum of the nucleon is very high. In the limit where $\beta$ goes to 1, we shall call such a reference frame the *infinite-momentum frame*. In such a frame, from the Heisenberg uncertainty relationship, the time of interaction of the virtual

photon with the parton is negligible. The photon couples to only one parton and the nucleon system is frozen in a given state. The diagram of Fig. 1.2 is now valid, with the difference that the longitudinal (i.e. along the direction of the virtual photon) momentum distribution of the parton is not centered around 0 but around the average fraction of longitudinal momentum carried by the quark to the momentum of the nucleon. Let $P$ be the four-momentum of the nucleon and $k$ be the four-momentum of the quark. Our aim is to relate $\xi = \frac{k_z}{P}$ to the scaling variable $x_{bj}$. By definition, our infinite-momentum frame is such that $P \gg M$. If we set

$$a = \frac{M}{P}$$

$$b = \frac{M}{\nu}$$

then the components of the four-momentum of the virtual photon in the infinite momentum frame will be

$$\begin{pmatrix} 0 \\ 0 \\ \frac{M}{ab}\left(\sqrt{1+b^2}\sqrt{1+2ax_{bj}}-1\right) \\ \frac{M}{ab}\left(\sqrt{1+b^2}-\sqrt{1+2ax_{bj}}\right) \end{pmatrix}$$

If we keep only terms of order $i+j$ less than or equal to 2 in $a^i b^j$, the components are approximately

$$\begin{pmatrix} 0 \\ 0 \\ \frac{M\nu}{2P} - xP\left(1-\frac{M^2x_{bj}^2}{Q^2}\right) \\ \frac{M\nu}{2P} + xP\left(1-\frac{M^2x_{bj}^2}{Q^2}\right) \end{pmatrix}$$

and now the relation $(k+q)^2 = m_p^2$ in the infinite momentum frame will yield

$$-Q^2 + 2\left(\sqrt{\xi^2 P^2 + m_t^2}\left(\frac{M\nu}{2P} - x_{bj}P(1 - \frac{x_{bj}^2 M^2}{Q^2})\right) + \right.$$
$$\left. \xi P\left(\frac{M\nu}{2P} + x_{bj}P(1 - \frac{x_{bj}^2 M^2}{Q^2})\right)\right) = 0 \tag{1.10}$$

where we have set $m_t^2 = k_t^2 + m_p^2$, $k_t$ being the transverse momentum of the parton. If we assume that $\xi P \gg m_t$ then a simple algebra shows that Eq. 1.10 will yield

$$\xi = \frac{Q^2}{2M\nu} = x_{bj}$$

In such a case, the interpretation of the scaling variable in quite simple; it is the fraction of longitudinal momentum carried by the quark in the infinite momentum frame.

### *1.2.3 The Parton Model*

The parton model assumes that lepton nucleon scattering occurs off point-like, charged partons. These partons are further assumed to be free. Under this assumption, the deeply inelastic cross-section can be written as an incoherent sum of elastic scattering off each parton making up the nucleon. In what follows, we shall assume that these partons have spin 1/2, an assumption that, as we shall see, is supported by experimental measurements. The charged-lepton elastic scattering cross-section off a structureless spin$-1/2$ particle is given by

In this case, the structure functions are simply proportional to delta functions, that is

$$F_1(Q^2,\nu) = \frac{1}{2}\frac{Q^2}{2M\nu}\delta\left(\frac{Q^2}{2M\nu} - 1\right)$$
$$F_2(Q^2,\nu) = \delta\left(\frac{Q^2}{2M\nu} - 1\right)$$

Now, let us assume that there is a probability density $f_i(x_i)$ of finding a parton in the nucleon carrying a fraction $x_i$ of the momentum of the said nucleon.

The momentum of the parton is given by

$$p_i = x_i P$$

where $P$ is the momentum of the proton (in the infinite-momentum frame).

Then it can be shown that

$$F_2(x) = \sum_i e_i^2 x f_i(x)$$

where the summation is done over the types of partons making up the nucleon. The relation between $F_1$ and $F_2$ is given by

$$F_2(x) = 2xF_1(x)$$

This identity is known as the Callan-Gross relation. It is equivalent to saying that the ratio $R$ of the of the longitudinal to the transverse cross-section vanishes. If the partons have spin zero, then $R = +\infty$. Experimentally, it was found that $R$ was consistent with 0, which supports the hypothesis that the partons have spin 1/2, but does not exclude the possibility that they have higher spin.

It is tempting to identify the partons with quarks, the mathematical objects postulated by Gell-Mann and Zweig. Stronger evidence for this model is provided by an experimental verification of a number of sum rules that we shall briefly discuss now.

### *1.2.4 Sum rules*

For the sake of convenience, we shall denote the probability functions by $u(x)$, $\overline{u}(x)$, $d(x)$, $\overline{d}(x)$, etc... instead of $f_u(x)$,...

The structure functions of the proton and the neutron can be written

$$\begin{aligned} F_2^{\mu p} &= \frac{4}{9}(xu(x) + x\overline{u}(x)) + \frac{1}{9}(xd(x) + x\overline{d}(x)) + \frac{1}{9}(xs(x) + x\overline{s}(x)) + \cdots \\ F_2^{\mu n} &= \frac{4}{9}(xd(x) + x\overline{d}(x)) + \frac{1}{9}(xu(x) + x\overline{u}(x)) + \frac{1}{9}(xs(x) + x\overline{s}(x)) + \cdots \end{aligned} \tag{1.11}$$

where the subscripts identify the proton and the neutron structure functions as measured in deeply inelastic muon scattering. The parton distributions are those of the proton, and those for the neutron are deduced from those of the proton by an isospin transformation.

Two elementary sum rules can be derived from the fact that the charge of the proton is 1 and the charge of the neutron is 0.

$$\int_0^1 (u(x) - \overline{u}(x))\, dx = 2$$

$$\int_0^1 (d(x) - \overline{d}(x))\, dx = 1$$

The first relation expresses the fact that there are two u-quarks in the proton and the second one that there is one d-quark in the proton.

In our discussion, we have emphasised the use of charged-lepton scattering, but important tests of the quark-parton model have been performed by neutrino scattering. Because of parity non-conservation in such an interaction, the deeply inelastic neutrino cross-section will depend on three structure functions $F_1^{\nu N}$, $F_2^{\nu N}$ and $F_3^{\nu N}$, where the superscripts identify the probe and the target. From charged-current interactions above charm threshold, one can derive the so-called Adler sum rules

$$\int_0^1 (F_1^{\overline{\nu}p}(x) - F_1^{\nu p}(x))\, dx = 1$$

$$\int_0^1 (F_1^{\overline{\nu}n}(x) - F_1^{\nu n}(x))\, dx = -1$$

and the Gross and Llewellyn-Smith sum rules

$$\int_0^1 (F_3^{\overline{\nu}p}(x) + F_3^{\nu p}(x))\, dx = 6$$

$$\int_0^1 (F_3^{\overline{\nu}n}(x) + F_3^{\nu n}(x))\, dx = 6$$

The above sum rules have been tested experimentally and found to be consistent with the values predicted by the quark parton model.

An important sum rule, due to Gottfried, relates the deeply inelastic muon scattering structure functions of the proton and the neutron. In the framework of the quark-parton model, it translates to

$$\int_0^1 \frac{(F_2^{\mu p} - F_2^{\mu n})}{x}\, dx = \frac{1}{3} + \frac{2}{3}\int_0^1 \left(\overline{u}(x) - \overline{d}(x)\right) dx$$

If one assumes that the sea is SU(2) symmetric, that is

$$\overline{u}(x) = \overline{d}(x)$$

then we get

$$\int_0^1 \frac{(F_2^{\mu p} - F_2^{\mu n})}{x}\, dx = \frac{1}{3}$$

This sum rule can be related to the neutrino structure functions. Below charm threshold, in charged-current interactions, one has

$$F_3^{\overline{\nu} p} - F_3^{\nu p} = 12\,(F_1^{\mu p} - F_1^{\mu n})$$

If

$$F_2 = 2xF_1$$

and if the Gottfried sum rule holds, then we get

$$\int_0^1 \frac{\left(F_3^{\overline{\nu} p} - F_3^{\nu p}\right)}{x}\, dx = 2$$

Recent high-precision measurements performed by the New Muon Collaboration (NMC) ((Amaudruz,1991)) show that actually the value of the Gottfried integral is significantly smaller than the value predicted by the quark-parton model with the assumption that $\overline{u}(x) = \overline{d}(x)$ Various theoretical attempts are made to explain the origin of the violation of the Gottfried sum rule. Historically, Feynman and Field incorporated a violation of the Gottfried sum rule in their parton distributions. The argument invoked was based on the Pauli-exclusion principle. Since the proton is made up of two up quarks and one

down quark, the extraction of a $u\bar{u}$ pair from the sea is less favorable then the extraction of a $d\bar{d}$ pair, since the Pauli exclusion principle restricts the quantum states available to the additional $u$ quark. However, a detailed calculation by Ross and Sachradja (Ross,Sachradja,1979) within a QCD framework does not support this conjecture.

### *1.2.5 Scaling violations*

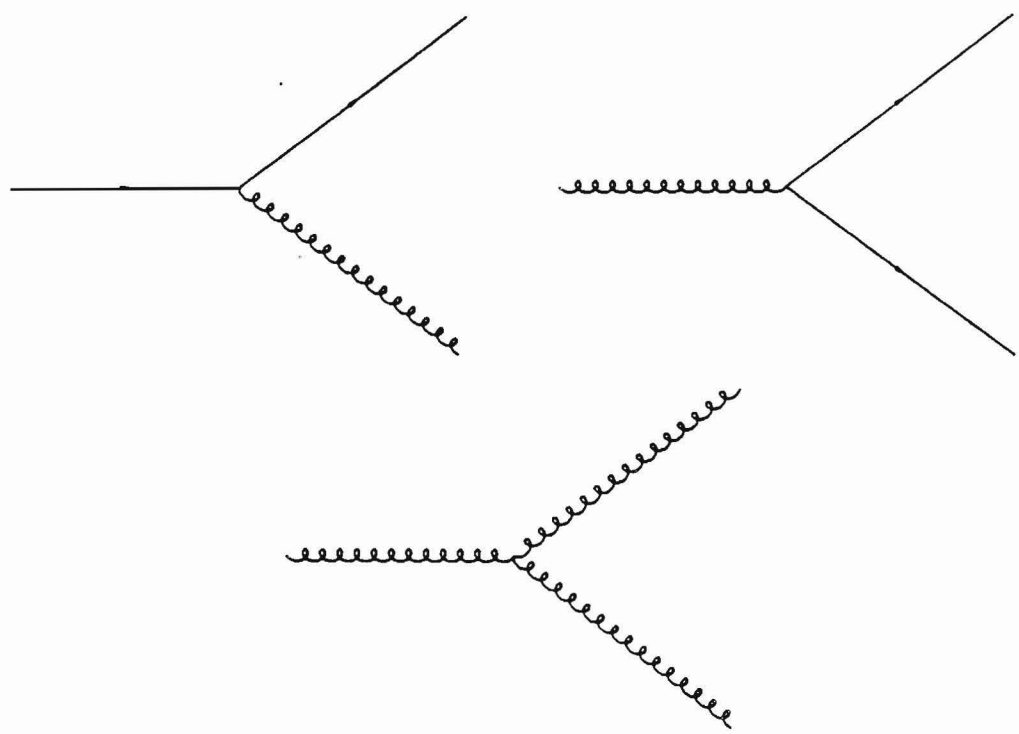

**The QCD splitting-function diagrams contributing to the scale breaking of the structure functions.**
**Fig. 1.4**

Although the simple parton picture presented in the previous section accounts for the bulk of the results observed in charged-lepton scattering, it is still an approximation. The European Muon Collaboration has shown clearly, as have earlier lepton experiments, that the hypothesis of scaling was only approximate. The structure functions do not depend only on $x_{bj}$ but also on

$Q^2$. This scaling violation can be understood in the framework of QCD in the following way (Collins et al.,1989). The quarks and the gluons inside the nucleon can undergo the processes shown in Fig. 1.4. In other words, as the $Q^2$ of the probe increases, more and more partons can be resolved. This implies that the parton distributions $f_i(x)$ are now a function of the scaling variable *and* $Q^2$. This statement can actually be made quantitative in the framework of QCD by the Altarelli-Parisi equations. These equations give the evolution of the structure functions as a function of $\log Q^2$ by considering the diagrams of Fig. 1.4 representing the so-called splitting functions. The Altarelli-Parisi equations do not determine the parton distributions, but if the quark and gluon distributions are known at a given $Q^2$, then they can be determined at any other value of $Q^2$.

### *1.2.6* $F_2^n/F_2^p$

Assuming that the ratio of longitudinal to transverse cross-sections in the proton and the neutron are the same, the ratio of the neutron structure function to the proton structure function is the same as the ratio of the corresponding cross-sections, that is

$$\frac{\sigma_n}{\sigma_p} = \frac{F_2^n}{F_2^p}$$

Because all distributions in Eq. 1.11 are positive, it can be shown that Eq. 1.11 implies that

$$\frac{1}{4} \leq \frac{F_2^{\mu n}}{F_2^{\mu p}} \leq 4$$

These inequalities have been confirmed by all muon and electron scattering experiments, including this one, as we shall see in Chapter 4. In fact, mea-

surements done so far seem to suggest that

$$\frac{1}{4} \leq \frac{F_2^{\mu n}}{F_2^{\mu p}} \leq 1$$

The upper limit is appears to be reached when $x_{bj}$ approaches 0 and the lower limit seems to be reached when $x_{bj}$ approaches 1.

# *Chapter 2*

# Experiment 665 at Fermilab

## 2.1 Generalities

The purpose of this chapter is to give an overview of the E665 spectrometer. Its goal, as stated in the original proposal and carried out in the data-taking period from 1987 to 1988, is to study deeply inelastic muon scattering with an emphasis on hadronic final states. It consists of two main components : a muon beam line, in which muons are generated and tagged, and a spectrometer built around two superconducting dipole magnets the purpose of which is to detect and tag the particles resulting from interactions in a target. The selection of desired events is performed by a main triggering system based on hodoscopes located behind a three-meter thick iron absorber.

The E665 apparatus has been described at some length in (Adams et al.,1990). In what follows, we shall emphasise the elements of the experimental setup which are directly related to our analysis.

## 2.2 The muon beamline and the beam spectrometer

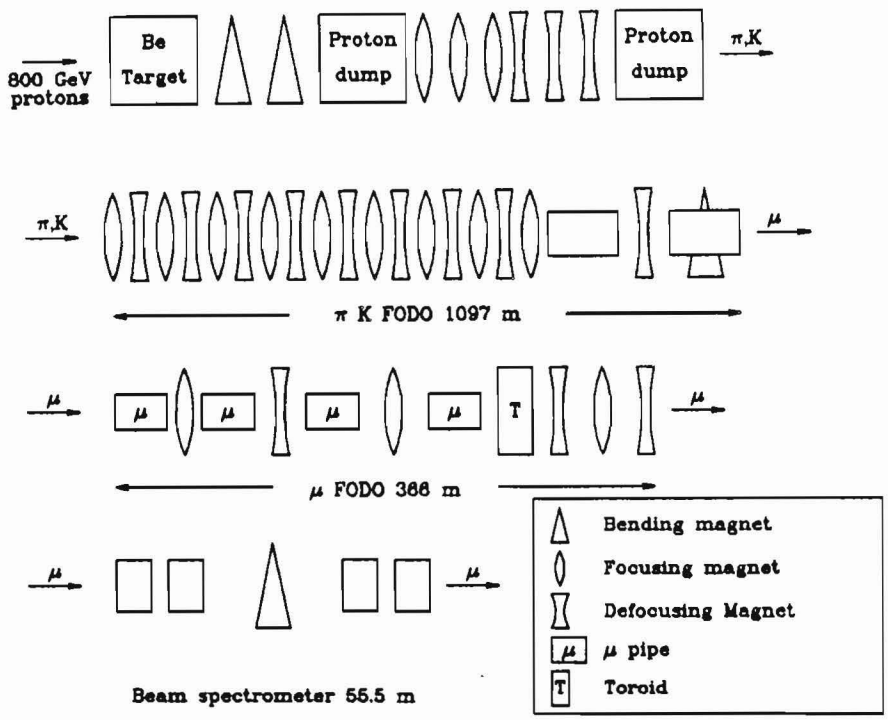


Synoptic view of the Muon beamline.
**Fig. 2.1**

The high-energy muons used by Experiment 665 originate from the weak decay of hadrons. 800 GeV protons, extracted from the Fermilab Tevatron, interact with a 48.5 cm beryllium target (Fig. 2.1). The resulting secondary particles, mostly pions and kaons, and the non-interacting primary protons are then deflected by a pair of dipole magnets, either into a dump absorber if their momentum is below 480 GeV, or into a system of quadrupole magnets if their momentum is above 480 GeV. The function of these quadrupole magnets is twofold. Firstly, they focus, and therefore contain the hadron beam, and secondly, they deflect and thus separate the particles according to their momentum. Those having momentum greater than 700 GeV end up in a secondary dump where they are absorbed. The remaining hadrons go through

a collimator and enter a 1.1 km beamline where they will be transported by a succession of focusing and defocusing quadrupole magnets (FODO) and allowed to decay into muons. The pions and kaons which, at the end of the FODO line have not decayed, are absorbed in 12 m of beryllium. The muons traverse the beryllium, undergoing limited multiple scattering, get momentum-selected by a final bending magnet and enter a 366-meter long transport line labelled as $\mu$–FODO in Fig. 2.1. At this stage, the muon beam consists of a well-collimated core surrounded by an undesirable halo. Therefore, the function of the $\mu$FODO line is, in addition to transporting the muons, to reduce the amount of halo present in the beam. This is achieved by the presence of $\mu$–pipes and toroids around the beam line. The $\mu$–pipes are high magnetic permeability steel sheaths, of inner diameter 12.7 cm and outer diameter 19 cm and length 6 to 10 meters. They are traversed by an electrical current which generates an 18 Tesla circular magnetic field strong enough to deflect any halo muon entering the pipe outward and prevent it from multiple-scattering back inside the beam pipe. The toroids have a magnetic field which increases with distance from their axis, and therefore, the further away the muons from the beam axis, the more they get deflected outward. The net effect of the toroids and the $\mu$-pipes is to bring down the beam/halo ratio from 1/1 to 0.15/0.85.

The last leg of the journey of the beam, which now has an average energy of about 500 GeV, takes it through a tagging system consisting of a diople magnet labelled NMRE in Fig. 2.1 and four hodoscope and wire-chamber stations. The purpose of the tagging system is twofold. On the one hand the hodoscopes allow the experiment to trigger on a desired subset of the beam phase space as a prerequisite to any physics trigger, and on the other hand wire chambers make it possible to determine the momentum of each beam muon by measuring the deflection it undergoes when traversing NMRE; the latter imposes a 1.53

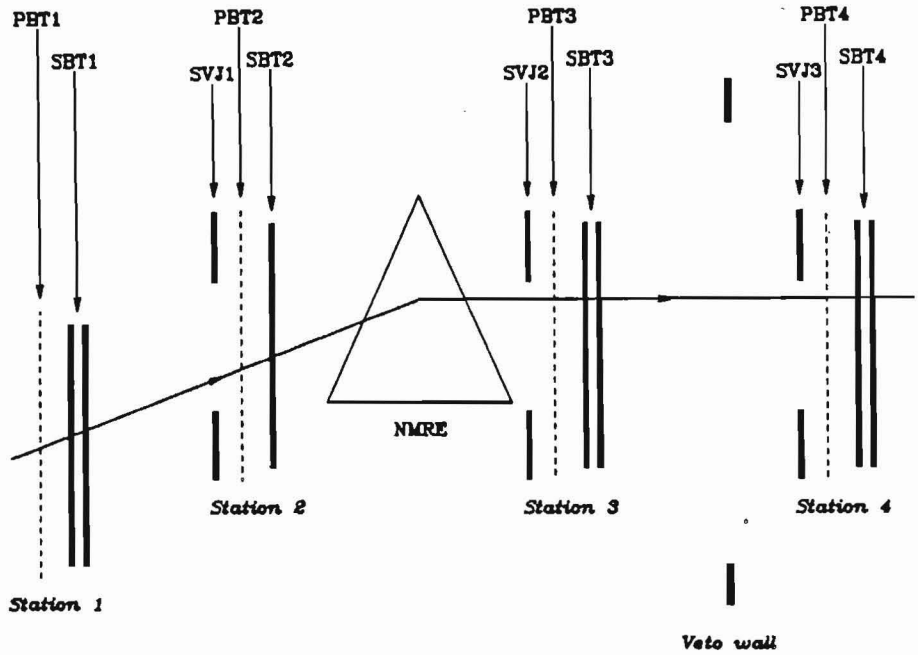


**Top view of the beam tagging system.**

**The layout is not to scale. Elements labelled SBT1 through SBT4 are scintillator arrays, those labelled SVJ1 through SVJ3 are veto counters, and PBT1 through PBT4 are six-plane wire chambers. NMRE is a six-meter long bending magnet which allows momentum determination of the beam muons.**

**Fig. 2.2**

GeV/c transverse kick to the beam particle, which at 500 GeV corresponds to a 3 mrad bending. A detailed view of the tagging spectrometer is shown in Fig. 2.2. It consists of two stations before the NMRE bending magnet and two stations after NMRE.

The elements labelled SBT1 through SBT4 are 17.8 cm×17.8 cm scintillator arrays and are shown in Fig. 2.3. Each station has a $Y$ and $Z$ array, except for SBT2 which has only a $Y$ hodoscope. PBT1 through PBT4 are groups of six-plane wire chambers. The Y and Z PBT planes consist of 128 wires 1 mm apart, whereas the U and V PBT planes have 64 wires, also 1 mm apart. The vetoing of the muon halo is achieved by a set of veto jaws (SVJ1 through

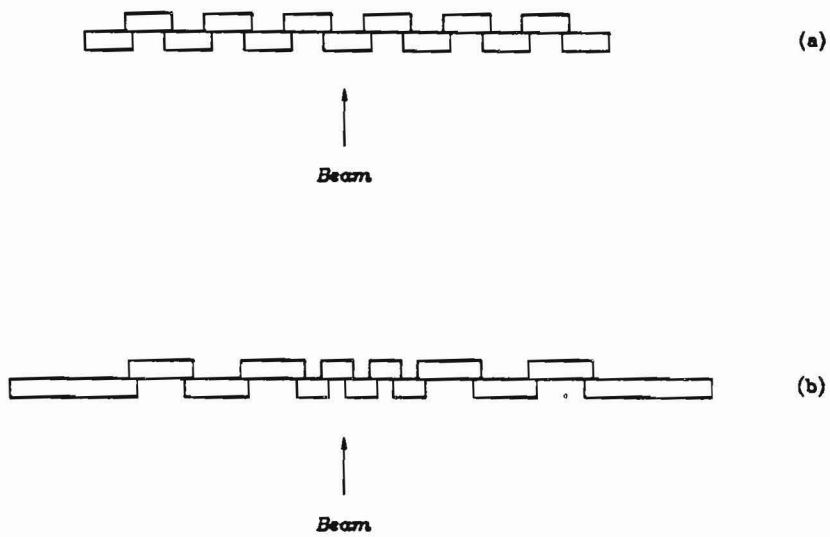


SBT counters.

(a) Finger arrangement of SBT1Z. (b) Finger arrangement of all other SBT counters. The fingers in the central region, where the beam density is the highest, have a narrower width.

**Fig. 2.3**

SVJ3) and a veto wall. The veto jaws have a 9.5 cm× cm aperture and their signal is used to inhibit the halo close to the beamline axis. The veto wall has a 25 cm× 25 cm aperture and an active area of 3 m× 3 m and guards the forward spectrometer against halo muons far from the beamline axis.

## 2.3 Targets

The target with which the incident muon beam interacts is located inside a superconducting dipole magnet (CVM). The vessel for hydrogen and deuterium is schematically represented in Fig. 2.4. It has a length of 1.15 m and a diameter of about 9 cm, and is made out of 250$\mu$–thick mylar, surrounded by a Rohacell insulation jacket, inside which a vacuum is maintained.

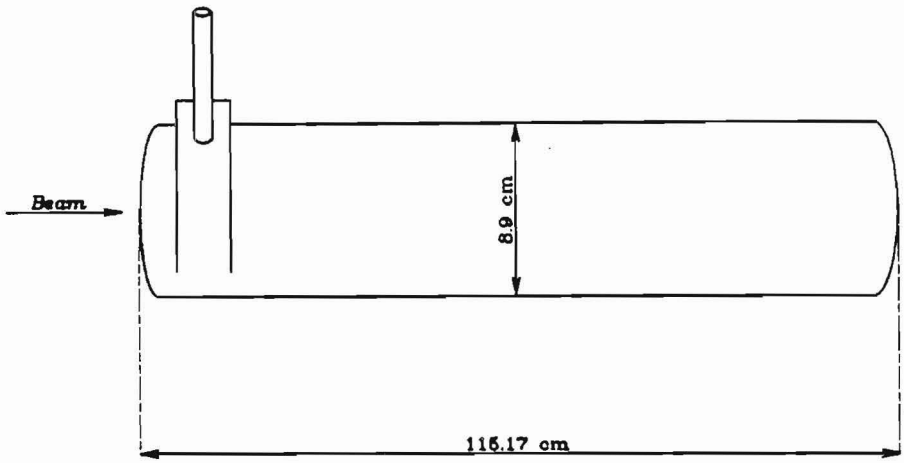


**Target vessel for $H_2$ and $D_2$.**
**Fig. 2.4**

The density of the hydrogen and deuterium targets have been reported in (Ecker,1988). The density of the hydrogen target is

$$0.07065(1 \pm (8 \pm 67) \times 10^{-}5)\,\mathrm{g/cm^3}$$

and the density of the deuterium target is

$$0.16246(1 \pm (5 \pm 310) \times 10^{-}5)\,\mathrm{g/cm^3}$$

However, the deuterium target contains a certain number of contaminants. Table 2.1 shows the composition, in volume, of the deuterium target. We can see that the dominant contaminant is HD. If one tries to compare neutron and proton cross-sections, this target composition will be the source of a small correction which will be discussed in the next chapter.

**Table 2.1**

| Compound | % volume |
|---|---|
| $H_2$ | 0.2±0.02 |
| HD | 5.1±0.2 |
| $D_2$ | 94.6±0.5 |
| $T_2$ | 0.1±0.04 |
| | in ppm |
| $H_2O$,HDO | < 200 |
| $N_2$,CO | 200±100 |
| $O_2$ | < 40 |
| Ar | < 30 |
| $CO_2$ | < 50 |

## 2.4 Forward spectrometer

The purpose of the forward spectrometer is to record the particles resulting from the interaction in the target. This main function can be conveniently subdivided into three sub-functions : triggering, which select the desired events, tracking, which is a prerequisite for charged-particle momentum analysis and particle identification of charged and neutral particles. Of the latter, we shall say very little since we do not make any use of this capability of the spectrometer in our work, and we refer the interested reader to (Adams,1990a)

### *2.4.1 Tracking system*

The heart of the E665 tracking system consists of 26 wire-chamber modules at the center.

built around two superconducting dipole magnets (Fig. 2.5). The first magnet (CVM) has a 1.5 Tesla field and generates a field integral of 1.29GeV/c Inside the second magnet (CCM) located 10.5 m downstream of the CVM and the field of which, oriented along the positive $z$–axis, has an intensity of 1.39 Tesla, five three-plane wire chambers (PCF) permit the following of charged-particle tracks in the region of the magnetic field. In principle, the measurement of

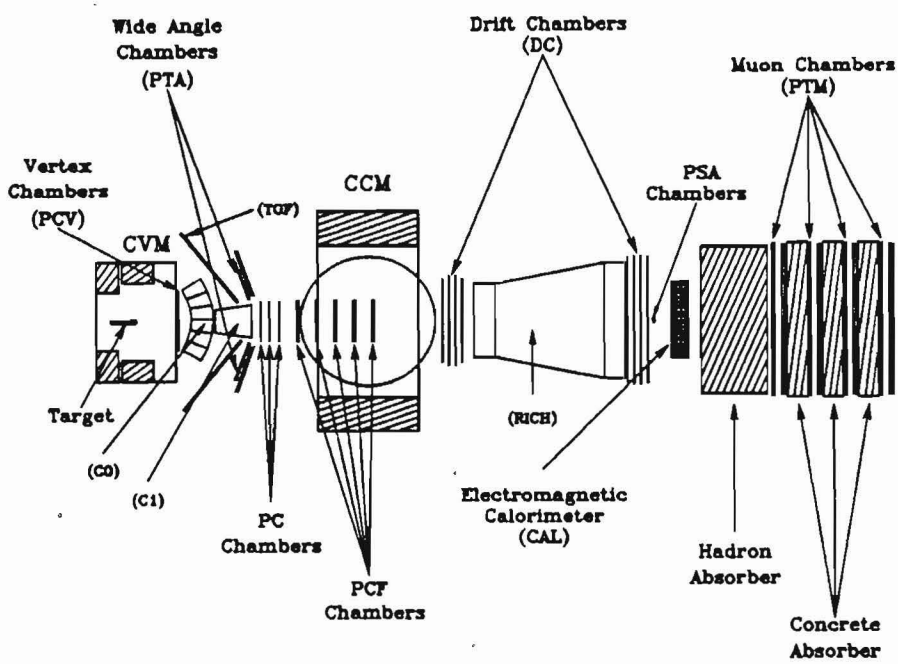


Top view of the E665 forward spectrometer.
**Fig. 2.5**

the curvature of a track using the PCF chambers alone is possible, but better resolution is achieved by the presence of two three-plane wire chambers (PCV) and three four-plane chambers (PC) located between the CVM and the CCM, and eight drift chambers downstream of the CCM. The central region of the drift chambers has been made insensitive, and is covered by a small additional chamber (PSA). The muon, which is the only particle to traverse a three-meter thick iron absorber (ABS) located behind the last set of drift chambers, is tracked by four proportional wire chambers (PTM). In addition, two sets of chambers in the wings of the spectrometer (PTA), between the CVM and the CCM intercept wide-angle tracks at their exit from the CVM.

### *2.4.2 Particle identification*

A particle can be identified once its charge and its mass are known. The only characteristic of a particle that the forward-spectrometer tracker provides is the sign of its charge. Since the momentum of a charged particle is known, its mass can be determined if its velocity is known. This is achieved in two ways. Two threshold Cerenkov counters (C0 and C1), running with gases at different indices of refraction permit the separation between particles, and a Ring-Imaging Cerenkov counting, by measuring the opening angle of the Cerenkov radiation emitted by the charged particle, allows the determination of its velocity and therefore its mass. The other method used for low momentum particles is the measurement of their time of flight since the instant of the interaction in the target. Specifically, a start signal is generated by a counter located in the beam spectrometer and a stop signal is sent by scintillator planes (TOF) in the wings of the spectrometer, between the CVM and the CCM. The distance between the start and stop counters being known, this time of flight will give the velocity of a particle resulting from he interaction and therefore its mass, the momentum being known from the bending induced by the CVM.

The direct identification of neutral particles is not possible by the tracker, and this function is delegated to an electromagnetic calorimeter (CAL) situated behind the last set of drift chambers.

## 2.5 Triggering system

In a high-energy scattering experiment, the number of "good" events is usually much smaller than the total number of events resulting from the incident beam traversing the target. The latter is usually too large to allow the data-taking system to record them all. This calls for an electronic filter, the trigger, which selects only the events of interest to the experiment. The

E665 triggers can be divided into two classes : the normalisation triggers and the physics triggers. The purpose of the normalisation triggers is to allow the measurement of the beam flux by a random sampling of the beam used in the physics triggers. The latter consist of the large-angle trigger (LAT), which has good acceptance for those events in which the muon emerges from the target with an angle with respect to its original direction greater than 3 mrad; the small-angle trigger (SAT) which uses about 12% of the beam and has good sensitivity for events in which the scattering angle is above 0.5 mrad.

### *2.5.1 LAT trigger*

The large-angle trigger (LAT) is formed by requiring the presence of a beam in a given event and the presence of an outgoing muon the trajectory of which does not intercept a central veto region.

The first requirement is realised by the beam hodoscopes (SBT, SVJ and SVW). It is required that 7 out of 7 SBT planes generate a signal, that neither the SVJ planes nor SVW register a hit.

The second requirement is constructed by demanding the presence of hits in three out of four scintillator stations (SPM) and the absence of hits in small companion scintillators (SMS). The layout of the muon system is shown in Fig. 2.7. Each SPM plane (Fig. 2.6) consists of an array of 30 scintillator paddles. All counters are 50-cm wide and 1.5-m high, except the central counters which are 20-cm wide and 1.5-m high. This gives the muon system an aperture of about 7 m in $y$ and 3 m in $z$.

The SMS planes (Fig. 2.8) are formed by the juxtaposition of 16 fingers of a length of 21.59 cm and a width of 1.32 cm (for the 14 central fingers) or

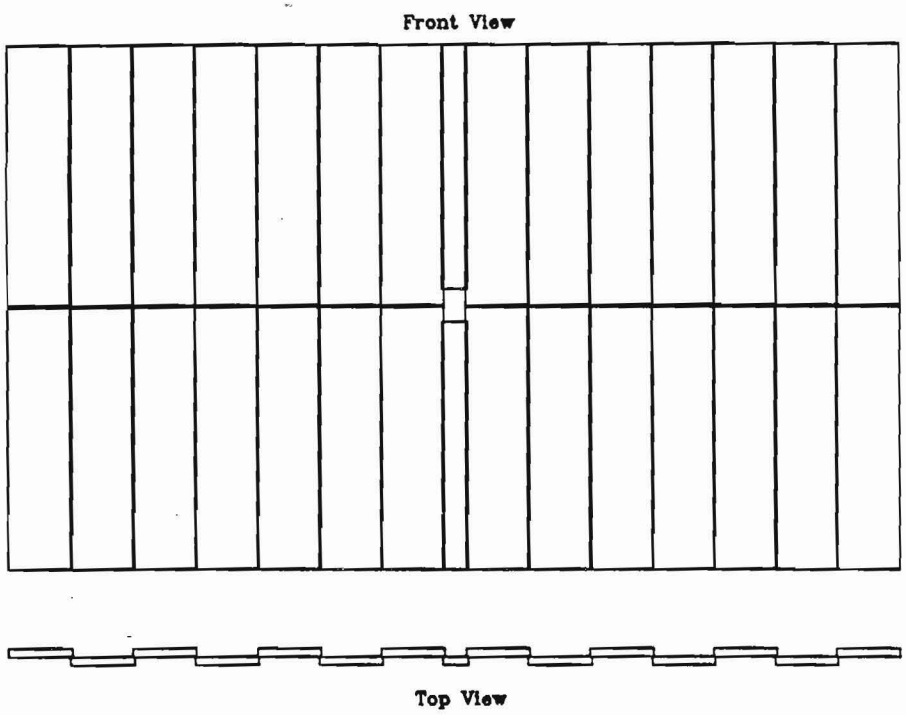


Array structure of the muon scintillator planes.
**Fig. 2.6**

1.96 cm (for the two outer fingers) and define a central area which overlaps with the central SPM planes. Each SMS station consists of a $z$ and a $y$ view.

The logic of the large-angle trigger is shown in Fig. 2.9. The signals originating from the SPM stations are discriminated and put in coincidence to produce a positive signal if at least three out of four SPM stations at the top or threee out four SPM stations at the bottom have a hit. The signals generated by the first and fourth SMS stations act as a veto against events which might otherwise be accepted, being either non-interacting beams or very small-angle scatters. The radio-frequency (RF) from the accelerator strobes the signals arriving at the main coincidence module.

Associated to the LAT trigger, the RBEAM trigger requires that 7 out of 7 SBT planes register a hit, that neither the veto jaws nor the veto wall register

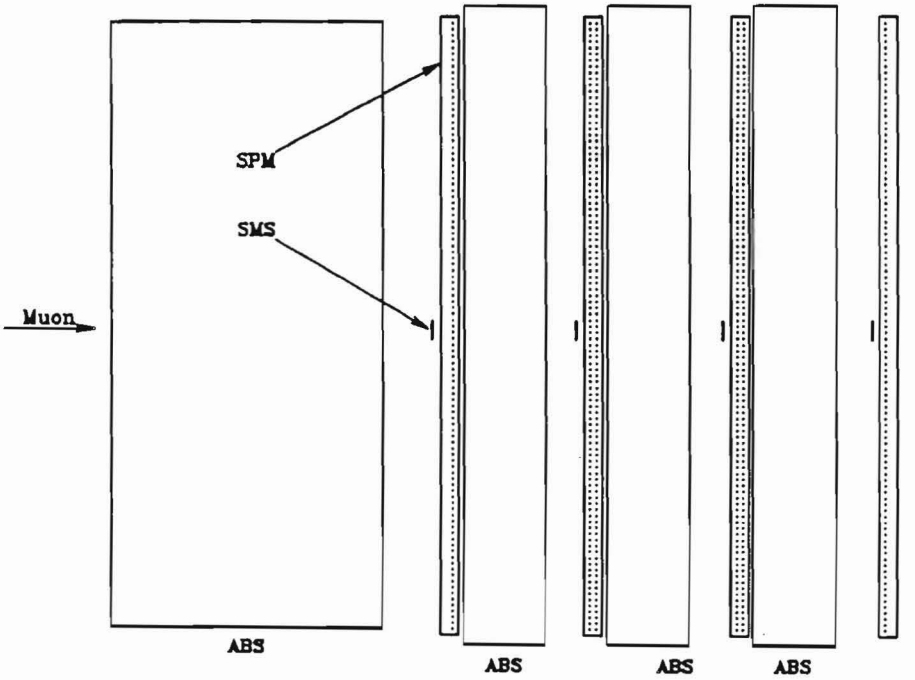


**Layout of the muon system, showing the four large scintillator walls (SPM) and their companion central hodoscopes (SMS). The stations are separated by three concrete absorbers.**

**Fig. 2.7**

a signal. This definition is similar to the beam part of the LAT trigger, but the RBEAM trigger is performs a random sampling of the beam through a hardware random generator : on the average, every $2^{19}$ (for the hydrogen run) or $2^{18}$ (for the deuterium run) beam is selected and recorded on tape.

### *2.5.2 SAT trigger*

The small-angle trigger (SAT) has been described in detail in (Magill,1990). It is a floating-veto trigger. A fraction of the beam (12%) is projected to the absorber and the predicted impact point is compared with the actual muon position. If the latter falls outside a window centered around the beam projection, the beam is accepted. The window is defined by an appropriate

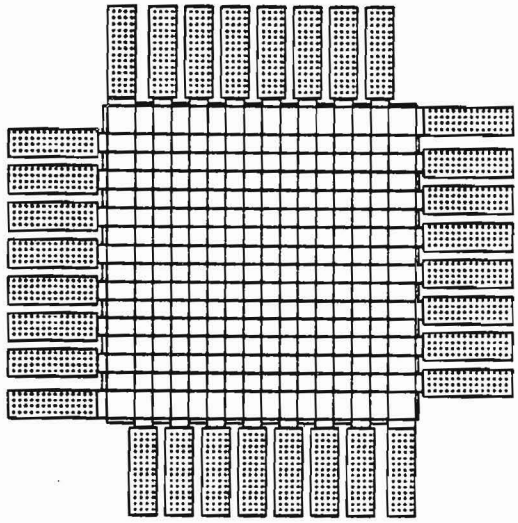

**Array structure of the SMS planes.**
**Fig. 2.8**

combination of SMS fingers. The minimun scattering angle to which this trigger has good acceptance is 0.5 mrad.

## 2.6 Data-acquisition system

The signals originating from the detectors are read out through CAMAC modules, then sent to three PDP11/34. The signals from the calorimeter are read out through a Fastbus processor Fig. 2.10 These four event segments are transferred to a $\mu$–VaxII which concatenates events and then transmits them to the tape logger or, for a fraction of the events, to a Vax11/780 for analysis and monitoring.

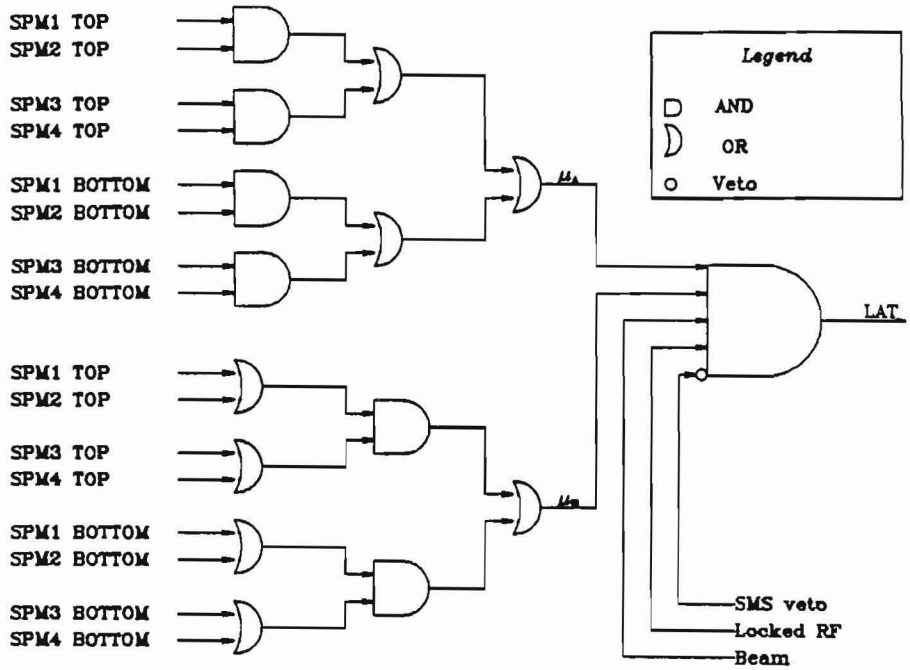


Logical diagram of the LAT trigger.

**Fig. 2.9**

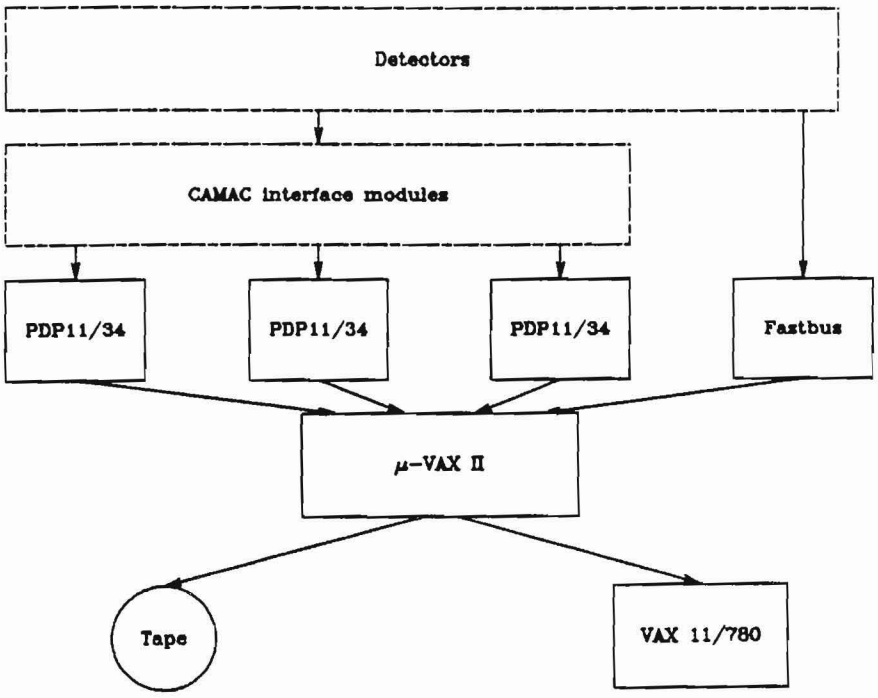


Synoptic diagram of the online data acquisition system.

**Fig. 2.10**

# *Chapter 3*

# Data analysis

## 3.1 Generalities

As stated in the Introduction, our goal is to compare the quark content of the proton and that of the neutron. We have seen in Chapter 1 that these are related to the nucleon structure functions, these being phenomenological quantities in the expression of the deeply inelastic scattering cross-sections. Thus, from an experimental standpoint, our approach will be to compare the proton and the neutron cross-sections and then relate those to the quark contents of these nucleons, This has been done in the past by other muon experiments (CHIO,EMC,BCDMS,NMC), but the fact that the E665 muon beam has an energy of 500 GeV allows it to cover a wider kinematical range than covered so far.

Cross-section measurements involve essentially a counting of the number of scattering events produced per incident beam flux per unit number of scattering centers in a unit area in an elementary cell of the kinematical phase space.

Specifically, if the apparatus registers $\Delta N$ events in an elementary cell $\Delta\Omega$ of the kinematical domain, the expression of the experimental cross-section $(\frac{\Delta\sigma}{\Delta\Omega})_m$ is given by

$$\left(\frac{\Delta\sigma}{\Delta\Omega}\right)_m = \frac{A}{\mathcal{N} n_b \rho l} \frac{\Delta N(\Omega)}{\Delta\Omega} \tag{3.1}$$

where $A$ is the number of nucleons in the target nucleus, $\rho$ is the density of the target, $l$ its length, $n_b$ the number of beams necessary to produce $\Delta N$ interactions and $\mathcal{N}$ is the Avogadro number.

The quantity we seek is not $(\frac{\Delta\sigma}{\Delta\Omega})_m$ but the deeply inelastic part of it. Because of its imperfection, the apparatus will, on the one hand, accept events which are not those of interest and to which we generically refer to as *background*, and on the other hand fail to register deeply inelastic events because of its non-unit acceptance. This can be expressed as

$$\Delta N(\Omega) = \varepsilon(\Omega) \times \Delta N_1 + \Delta N_b \tag{3.2}$$

where $N_1$ is the actual number of inelastic events and $N_b$ is the number of background events. The quantity $\varepsilon(\Omega)$, the overall probability for observing a deeply-inelastic event when one actually occurred, can be written as the product of three three efficiencies.

$$\varepsilon(\Omega) = \varepsilon_a(\Omega)\varepsilon_t(\Omega)\varepsilon_s(\Omega)$$

$\varepsilon_a(\Omega)$ is the acceptance of the spectrometer, $\varepsilon_t(\Omega)$ is the trigger efficiency, that is, the probability for the trigger to register an event given that it falls within the acceptance of the spectrometer, and finally, $\varepsilon_s(\Omega)$ is the probability of reconstructing an event given that it has been accepted by the trigger.

Consideration of the steps involved in the software chain allow us to decompose $\varepsilon_s(\Omega)$ into a product of efficiencies. Events from raw tapes are written

out on separate output streams according to their trigger type. In a second step, a filter is applied on the events in order to reject those which are obviously not deeply-inelastic scattering events. The efficiency of this process to retain good events will be denoted by $\varepsilon_f(\Omega)$. Next, the events that have been passed by the filter are run through a pattern recognition program in order to reconstruct the forward-spectrometer trajectories of the particles resulting from the interaction. The efficiency of the pattern recognition for finding the muon in the forward spectrometer is $\varepsilon_p(\Omega)$. Once the tracks have been found, they are fitted in order to determine their momentum. The fitting procedure has a probability $\varepsilon_{tf}(\Omega)$ of succeeding in performing the fit.

At this stage, it is still unknown which track in the forward-spectrometer is actually the scattered muon. This ambiguity is resolved by a muon-matching program which determines which forward spectrometer track should be labelled "scattered muon" by making use of the projection lines found in the PTM stations. The efficiency of the muon matching will be denoted by $\varepsilon_m(\Omega)$. Finally, once the muon has been identified, the vertex reconstruction program attempts to find the primary interaction vertex. This code has an efficiency $\varepsilon_v(\Omega)$. Then we can write

$$\varepsilon_s(\Omega) = \varepsilon_f(\Omega)\varepsilon_p(\Omega)\varepsilon_{tf}(\Omega)\varepsilon_m(\Omega)\varepsilon_v(\Omega)$$

It should be understood that the efficiencies defined above are to be interpreted as conditional probabilities. For instance, $\varepsilon_m(\Omega)$ is the probability of identifying the muon given that an event has successfully passed all the criteria required by the muon matcher to perform identification.

Efficiencies are diagonal operators in the kinematical domain. The finite resolution of the detector induces a non-diagonal resolution operator $K(\Omega, \Omega')$

which relates the true number of events to the observed number of non-background events

$$\frac{dN_2}{d\Omega} = \int_{\mathcal{D}} \varepsilon(\Omega')\, K(\Omega, \Omega')\, \frac{dN_1}{d\Omega'}\, d\Omega' \tag{3.3}$$

We shall see that, in this analysis, resolution effects are negligible.

All the aforementioned effects can be attributed to the apparatus and the reconstruction software. There are two other corrections that need to be done in order to extract the cross-section resulting from the one-photon exchange diagram. The first one, called radiative correction, originates from higher-order electromagnetic diagrams contributing to the single-photon exchange cross-section. The second correction, called *Fermi motion*, comes about when one tries to extract the neutron cross-section. Since there is no source of free neutrons in nature, one has to use deuterium as a target and it is then assumed that

$$\sigma_n = \sigma_D - \sigma_p \tag{3.4}$$

Such a relation, as we shall see, is only approximate and the neutron cross-section so extracted must be corrected for the distorsion resulting from the fact that the deuteron is a bound system.

The situation when one measures cross-section ratios becomes somewhat simpler. If we assume that the resolution kernel is nearly diagonal, then the convolution operator of Eq. 3.3 is the identity, in which case the smeared and true cross-sections are nearly equal. As a consequence of this, the ratio of the observed cross-sections is equal to the ratio of the true cross-sections, provided that the efficiency $\epsilon$ is the same for both target runs.

In our data analysis, we must therefore check the consistency of the running conditions for the different target periods, and if they happen to change, we

must correct for such variations, which will necessarily induce an uncertainty on the value of the final result.

The rest of this chapter will be dedicated to the study of the apparatus effects on the cross-sections and the uncertainties thereof. It is however appropriate to present an overview of the software that led to our final data sample. As mentioned earlier, the software should be regarded as an extension of the apparatus, and henceforth its effects should be included in our analysis.

## 3.2 Analysis software

### *3.2.1 Reconstruction software*

The raw data are split according to their trigger type, then filtered in order to remove useless events, and finally reconstructed.

#### *3.2.1.1 Event splitting*

This data processing phase is straightforward. Raw data tapes contain a mixture of events which originate from different triggers. In order to make further processing more manageable, events are streamed according to their trigger type. At the same time, event counters are updated.

#### *3.2.1.2 Event filtering*

Two requirements must be made in any trigger design. Firstly, the trigger should always accept those events the experiment is looking for, in our case deeply inelastic events, and secondly, it should reject those events which are regarded as background. If the second condition were met exactly, no offline filtering would be necessary. In reality, complications arise which prevent the trigger from rejecting background events. The purpose of the software filter

is to remove those triggers which are obviously bad in order to reduce the amount of data that needs to be reconstructed and analysed at a later stage. We can distinguish two classes of unwanted events that are not rejected by the large-angle trigger. The first class contains physical muon interactions in the target, such as muon-electron scattering or muon bremsstrahlung, that the trigger cannot distinguish from deeply inelastic scattering events. Those events are not rejected by the filtering program and are handled at a later stage of the analysis. The second class is composed of events in which no interaction occurred but in which a fake coincidence is formed between the beam signal and the signal resulting from the outgoing muon. In a first step, the filter program requires that all of the 7 SBT hodoscopes register a hit. If this condition is not satisfied, the event is rejected. For an event that passes this first step, the beam track is reconstructed using the PBT chambers. If the track cannot be reconstructed, the event is discarded. If more than one beam track is reconstructed, again the event is rejected. If exactly one beam track is found, it is required that it be an in-time beam. Furthermore, if the beam has a momentum less than 300 GeV and the $\chi^2$ probability of the fit is greater than 1% the event is not accepted. Once an event has passed the aforementioned beam quality criteria, tracks in the central region of the forward spectrometer are reconstructed. The main goal at this stage is to determine whether the event is a non-interacting beam muon. If no track traverses the PSA chamber or if at least two tracks are found to traverse the PSA chamber, the event is accepted. In the case where exactly one track is found to cross PSA, the beam track is extrapolated to the point where the fit parameters of the forward track are reported and a geometrical match is attempted between the latter and the beam track. The event is declared a straight-through muon and rejected if all

the following conditions are satisfied :

$$|\Delta y| < 1\,\mathrm{mm}$$

$$|\Delta z| < 1\,\mathrm{mm}$$

$$|\Delta y'| < 3.9 \times 10^{-4}$$

$$|\Delta z'| < 3.9 \times 10^{-4}$$

$$|\Delta p| < 50\,\mathrm{GeV}$$

$$|\Delta \theta| < 0.29\,\mathrm{mrad}$$

where the above quantities are respectively the difference in y-position, z-position, y-slope, z-slope, momentum and angle between the extrapolated beam track and the forward-spectrometer track. The above cuts were determined from a study of random-beam events.

#### *3.2.1.3 Pattern recognition*

The details of the pattern-recognition software have been described elsewhere (Ryan,1990), and in this section we shall only give a brief overview of the steps involved in finding tracks in the forward spectrometer.

In a first stage, lines are found in the PC and the DC chambers. These segments are linked through the CCM by hits collected in the PCF chambers. Next, the unpaired PC segments are extrapolated into the PCF chambers where unused hits are claimed in order to construct a PC-PCF orbit. These PC-PCF orbits are extrapolated in turn into the PSA chambers where the hits are associated to the original PC-PCF track. In this process, the extrapolation is based on a parabolic fit of the PC-PCF orbit using a singular-value decomposition method. At this stage, there still remain PCF hits which have not been associated to any track. Space points are formed in the PCF chambers, parabolic fits are attempted on the found space points and the corresponding

orbit is extrapolated to the DC and the PC chambers to collect unused hits. Hits in the PCV chambers are associated to tracks by extrapolating from the PC chambers back into PCV.

#### *3.2.1.4 Track fitting*

The fundamental purpose of the track-fitting code is to estimate the momentum of the tracks found by the pattern-recognition code. The fitting of the beam tracks is accomplished by performing a straight-line fit in the $(x, z)$ plane of the space points found in the four PBT stations and a fit, in the $(x, y)$ plane of two straight lines constrained to meet at the center of the NMRE analysing magnet. This is justified by the fact that the bending induced by NMRE is in the $(x, y)$ plane and no deflection of the beam muon occurs in the $(x, z)$ view. The momentum resolution achieved in the beam spectrometer is 0.5% at 500 GeV.

The algorithm used to fit the tracks found in the forward spectrometer is more involved since the full CCM magnetic field map is taken into account. In a first pass, point fits are made in the PCV, PCF and PSA chambers and straight-line fits are made in the PC and DC chambers. The resulting local fits allow then to perform a cubic-spline fit which yields slope information about the tracks. This information is used to perform a quintic-spline fit to the coordinates and the reciprocal of the momentum of the trajectory resulting from a solution of the Lorentz equation. It is at this stage that the CCM field map is used. This first fit yields new values for the slopes, values which are used to repeat the quintic-spline fit. This iterative procedure is stopped when convergence is achieved. It is to be pointed out that multiple scattering is taken into account by modifying the weight matrix used in the $\chi^2$ minimisation (Salvarani, 1991).

For more details on the track-fitting method, we refer to (Salvarani,1991).

#### *3.2.1.5 Muon identification*

All particles except muons are stopped by the iron absorber. This gives us the possibility to identify the muon by matching the $y$ and $z$ projections of its trajectory as reconstructed in the PTM chambers with one of the tracks found in the spectrometer upstream of the absorber.

The matching algorithm has been described in (Anthony,1989a) and (Anthony,1989b). It proceeds in two phases. First it attempts a match by solely taking into account the amount of multiple scattering experienced by the muon in the lead of the calorimeter and the iron absorber; this is the multiple-scattering match. However, the muon may undergo catastrophic scattering in the lead or the iron, in which case its slope in the PTM system will be significantly different from its slope as measured by the forward chambers. In this case, the multiple scattering match will fail, and the second phase of the matching algorithm takes over. This is the intersection-match pass.

In the multiple-scattering stage, each PTM projection line is extrapolated to the back of the iron absorber. Then, for each PTM extrapolation, each forward track (FS) is extrapolated to the same $x$-position and for each (FS,PTM) couple two figures of merit are calculated, namely

$$\chi^2_u = \frac{(u_{fs} - u_{PTM})^2}{\sigma^2_u + \tau^2_u}$$

$$\chi^2_{u'} = \frac{\left(\arctan u'_{fs} - \arctan u'_{PTM}\right)^2}{\sigma^2_{u'} + \tau^2_{u'}}$$

where the subscript $u$ refers to the $y$ or the $z$ coordinate, depending on the PTM view, and $u'$ to the slope in the corresponding view. $\tau$ is the error due to

multiple scattering and $\sigma$ the error due to the resolution of the PTM chambers.

Now, a pair (FS,PTM) is declared to be a candidate for a match if

$$\chi^2_u < 40$$

$$\chi^2_{u'} < 40$$

for both the $y$ and $z$ view. If, for a given PTM projection, several FS tracks satisfy the above constraint, the pair for which both $\chi^2_u$ and $\chi^2_{u'}$ are the smallest is taken (a condition which, from a logical standpoint, might not be fullfilled). The three-dimensional PTM line is constructed by the $y$ and $z$ PTM projections which are associated to the same FS track.

If, at this stage, no muon has been identified, an intersection match is attempted. The steps are conceptually the same as in the case of the multiple scattering match. However, for a given pair (FS,PTM), the $x$-position of the intersection of the PTM projection and the FS track is calculated. For this pair to be a candidate link, the $x$-coordinate of its kink must be no further upstream then 0.5 m of the front face of the calorimeter and no further downstream than 0.1 m from the back face of the iron absorber. If an FS track is found to intersect more than one PTM projection in a given view in the absorber, the pair with the smallest scattering angle in that view is chosen. Conversely, if a PTM projection can be associated to more than one FS track in the absorber, again the pair with the smallest scattering angle is selected. The $y$ and $z$ PTM projections which are associated to the same FS track together form a three-dimensional muon track if in each view, the $x$-coordinates of their intersections with the FS track are within 8 cm of each other.

#### *3.2.1.6 Vertex search*

Once the momenta of the tracks are known, it is possible to search for

the vertices from which they originate. The method used in this experiment proceeds as follow. A first estimate of the position of the primary vertex is found by determining the point of closest approach of the beam track and the scattered-muon track. In a second pass, the processor searches for those tracks which are compatible with the vertex previously found. When no more tracks can be associated to the primary vertex, a global fit is performed on its position, using the beam, the scattered muon and the tracks associated so far. The vertex-search procedure can be summarised by the following algorithm.

```
procedure vertex_search;
begin
    primary_tracks := {beam,scattered_muon};
    remaining_tracks := all_tracks - {beam,scattered_muon }
    primary_vertex :=closest_approach(primary_tracks);
    while track in remaining_tracks and compatible with primary_vertex
    do
        primary_tracks := primary_tracks∪ {track};
        remaining_tracks := remaining_tracks - {track};
    end while;
    primary_vertex := closest_approach(primary_tracks);
    if primary_vertex not accepted then
        while bad_track in primary_tracks
        and primary_vertex not accepted do
            primary_tracks := primary_tracks - {bad_track};
            remaining_tracks := remaining_tracks∪ {bad_track};
            primary_vertex :=closest_approach(primary_tracks);
        end while;
    end if;
    while track in remaining_tracks and primary_vertex accepted do
        primary_tracks := primary_tracks∪ {track};
        remaining_tracks := remaining_tracks - {track};
        primary_vertex :=closest_approach(primary_tracks);
    end while;
end vertex_search.
```

### *3.2.2 Simulation software*

It has been the philosophy, in E665, to divide the Monte Carlo simulation into two phases : event generation (first-stage Monte Carlo) and detector simulation (second-stage Monte Carlo).

The purpose of the first-stage Monte Carlo is to simulate the interaction of a beam muon in the target of the experiment and track the resulting particles through the E665 spectrometer. The tracking is handled by the GEANT code (Brun,1978) which, in addition, has the capability of simulating various secondary processes throughout the material of the apparatus. The E665 interface to the GEANT system consists of a set of routines the purpose of which is, on the one hand, to inform GEANT of the geometry of the spectrometer and its physical characteristics (materials, magnetic field,...), and on the other hand, to control the tracking and retrieve the particles resulting from secondary processes in order to store them in the E665 data banks. The overall behaviour of GEANT can be partially controlled externally by a parameter file.

The Monte Carlo program consists of three main sections : initialisation, event generation and finalisation. The finalisation is trivial and does not deserve any comment. The function of the initialisation phase is to read GEANT parameters from a control file, to setup the materials and media characteristic of the apparatus, and to define of the geometry of the detector.

The event generation can be divided into three steps, namely beam gen-

eration, kinematical generation of the deeply inelastic process, hadronic final state generation and tracking.

The beam generation consists of reading the beam phase space at PBT1 and PBT4 from a file containing reconstructed RBEAM events. This beam is then tracked up to an $x$–position which is chosen randomly between the upstream and downstream faces of the target and determines the interaction point.

The next phase is the generation of the scattered muon kinematics. A $(Q^2, \nu)$ point is chosen in the kinematical plane by the acceptance-rejection method according to a parametrisation of the deeply inelastic cross-section. This kinematical point along with the beam and the target four-momenta is given to the LUND hadron generator (Sjöstrand,1982) to create a hadronic final state.

Th resulting particles are transferred to the GEANT tracking system. This phase of the event simulation has a dual purpose. On the one hand, it swims the particles through the spectrometer taking into account the magnetic field of the CVM and of the CCM. On the other hand, as a track is being propagated through the spectrometer, it may undergo a decay or an interaction with the materials of the apparatus. The secondary processes made available by the GEANT package and activated in the E665 simulation are : bremsstrahlung, pair creation, particle decay, hadronic interaction via the GEISHA simulator and energy loss. Additional particles resulting from interaction of parent

particles in the material of the spectrometer are transferred from GEANT to the E665 data banks. Geometrical tracking information is stored in so-called key planes, which contain the intersections of the track with planes typically located in front of detector modules. This information will be the main input to the second-stage Monte Carlo the function of which is to digitise these hits into wire-chamber hits, taking into account wire-chamber efficiencies. A detailed description of the efficiency measurement of the chambers and their implementation in the second-phase of the simulation can be found in (Ryan, 1991) and (Schmitt,1990). Once the wire hits have been generated, the reconstruction code is run on the simulated data to generate *reconstructed* Monte Carlo data.

Reliance on a Monte Carlo program always raises the question as to how well the detector has been simulated. Clearly, a poor simulation of the performance of the apparatus will result in an incorrect estimate of whatever correction factor one attempts to determine. It is our philosophy that only a minimal use of the Monte Carlo shall be made to correct the data. We will use the simulation program to calculate the acceptance of the trigger and to determine the efficiency of the pattern-recogniser to identify the muon. In addition to this, we shall use only a domain of the spectrometer where the muon has a high probability of being reconstructed; specifically we shall cut out any region of the apparatus where the probability for reconstructing the muon falls below 90%. In addition to this intrinsic problem, our Monte Carlo simulation suffers from a problem that was found too late to be rectified for this analysis.

The radiation lengths of the targets were implemented incorrectly, and were too small by a factor of a 100. This affected only the amount of multiple scattering in the target, and we shall argue later that this error does not impact the measurement of the reconstruction efficiency; it does affect the resolution in $Q^2$ and $x_{bj}$, but as we shall see later, this effect is negligible.

To overcome this difficulty, we check that the Monte Carlo reconstructed distributions are similar to the measured data distributions. Even so, we should in principle check that the *multivariate* reconstructed distribution is the same as the multivariate data distribution. Since this is also impossible in practice, we shall be comparing one-dimensional marginal distributions. Of course if the multivariate distributions are identical, then the marginal distributions will be equal. But the converse is not true, as can be easily seen by considering the marginal distributions of the following two-dimensional distributions defined on the unit square $[0,1] \times [0,1]$:

$$f(x,y) = \frac{3}{2}(x^2 + y^2)$$

$$g(x,y) = \frac{1}{2}(9x^2y^2 + 1)$$

We shall nevertheless follow an inductive approach and assume that if all one-dimensional data distributions agree with the corresponding one-dimensional reconstructed Monte Carlo distributions, then we can be confident that the Monte Carlo simulation mocks up the observed data reasonably well.

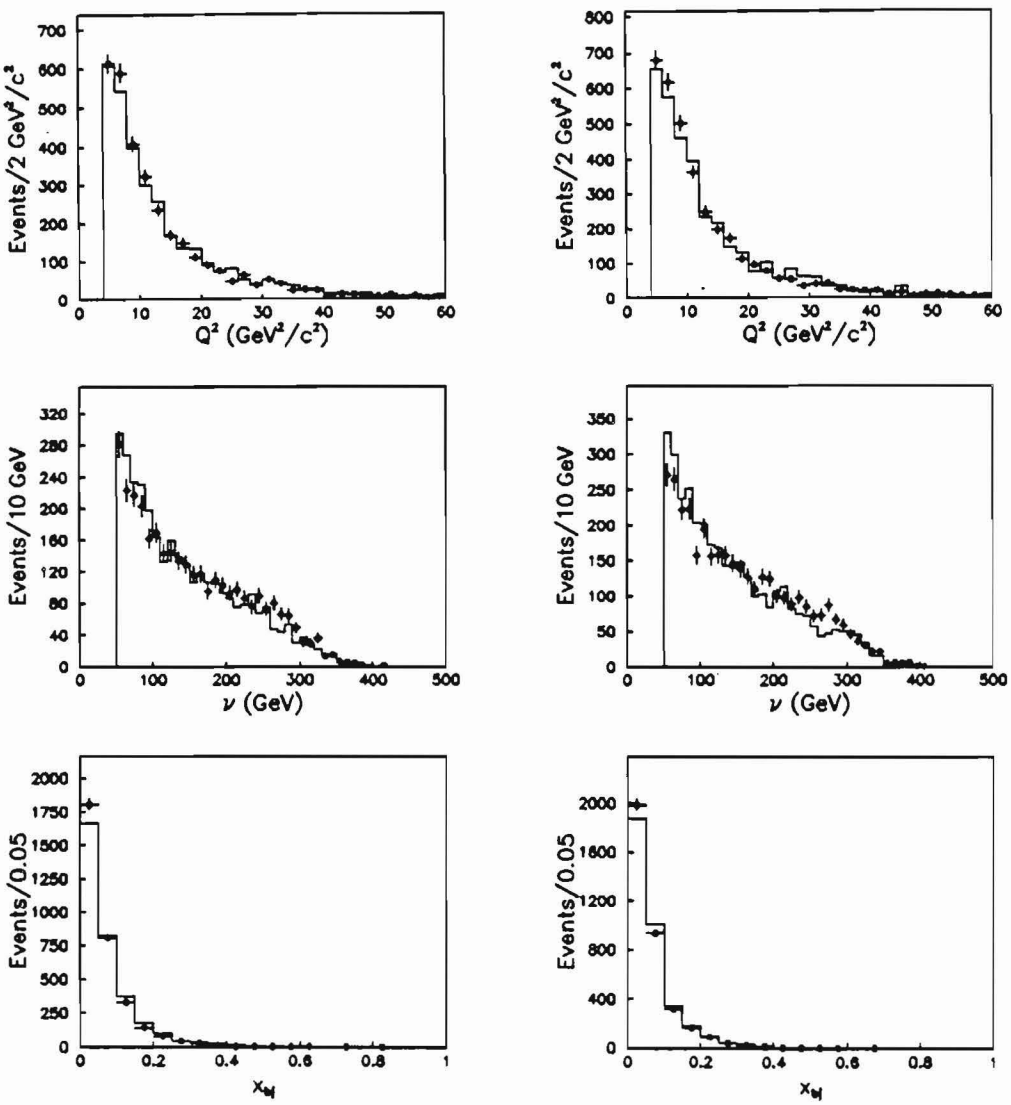


(a) (b)

Comparison between reconstructed Monte Carlo kinematical quantities (solid line) and observed kinematical quantities (solid circles) for (a) hydrogen and (b) deuterium.

**Fig. 3.1**

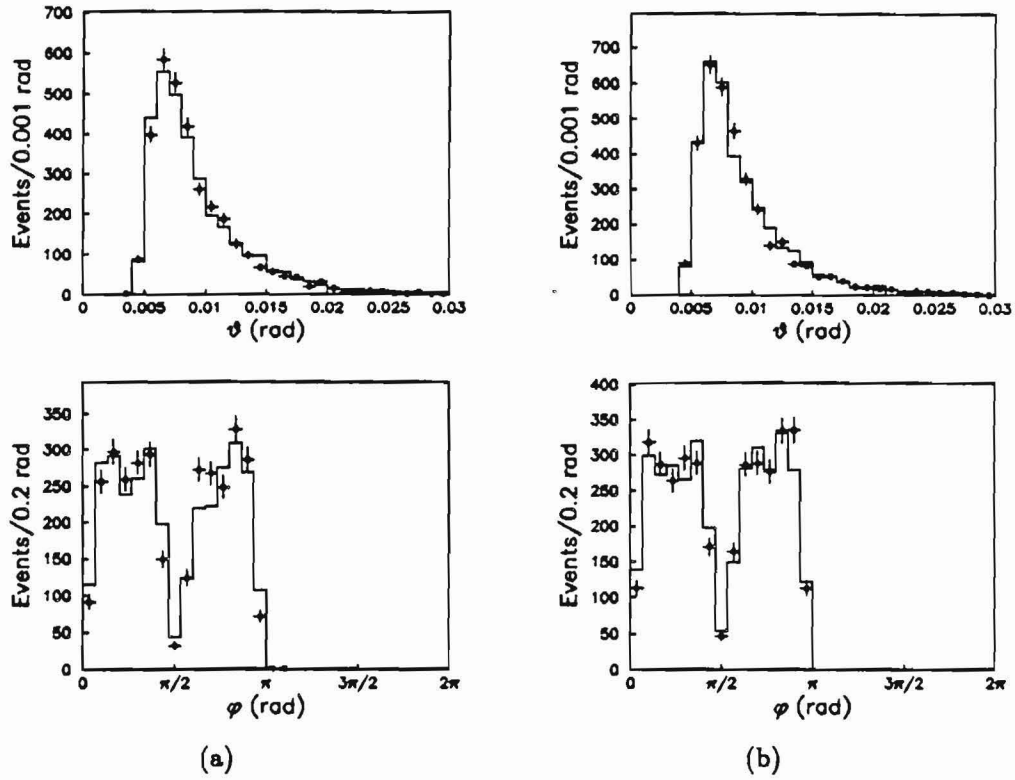


Comparison between reconstructed Monte Carlo kinematical angles (solid line) and observed kinematical angles (solid circles) for (a) hydrogen and (b) deuterium.

**Fig. 3.2**

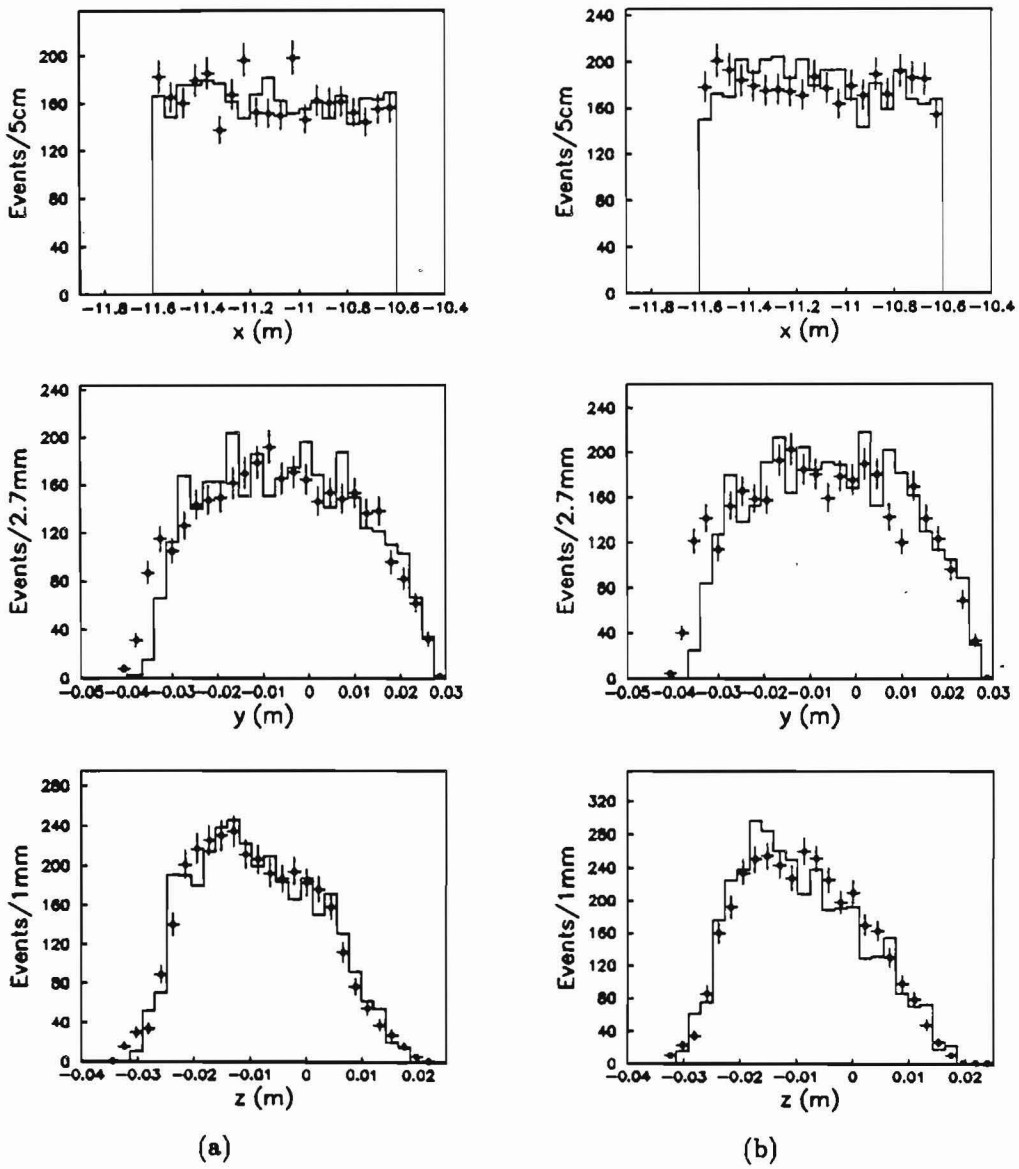


**Comparison between reconstructed Monte Carlo vertex position (solid line) and observed vertex position (solid circles) for (a) hydrogen and (b) deuterium.**

**Fig. 3.3**

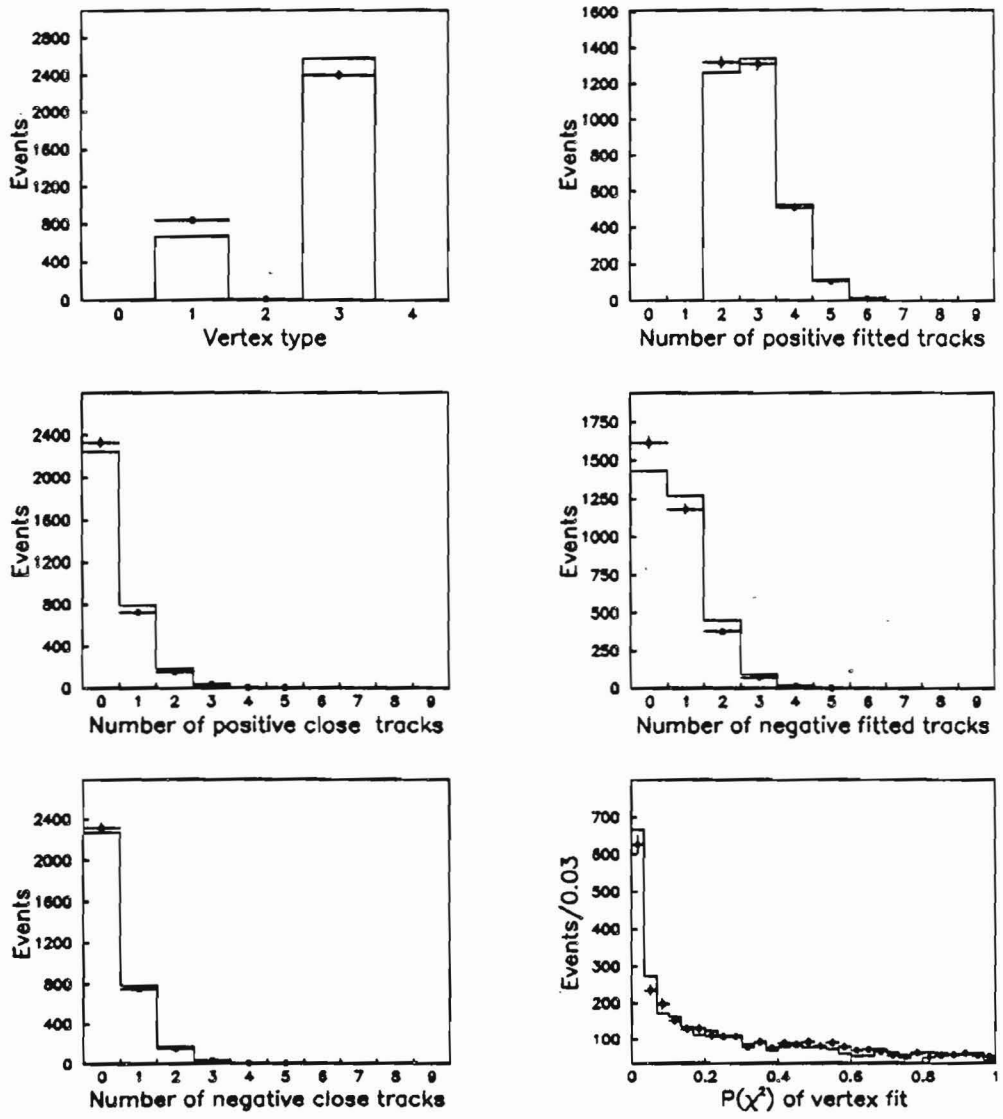


**Comparison between the vertex fit in Monte Carlo (solid line) and data (solid circles) for hydrogen.**

**Fig. 3.4**

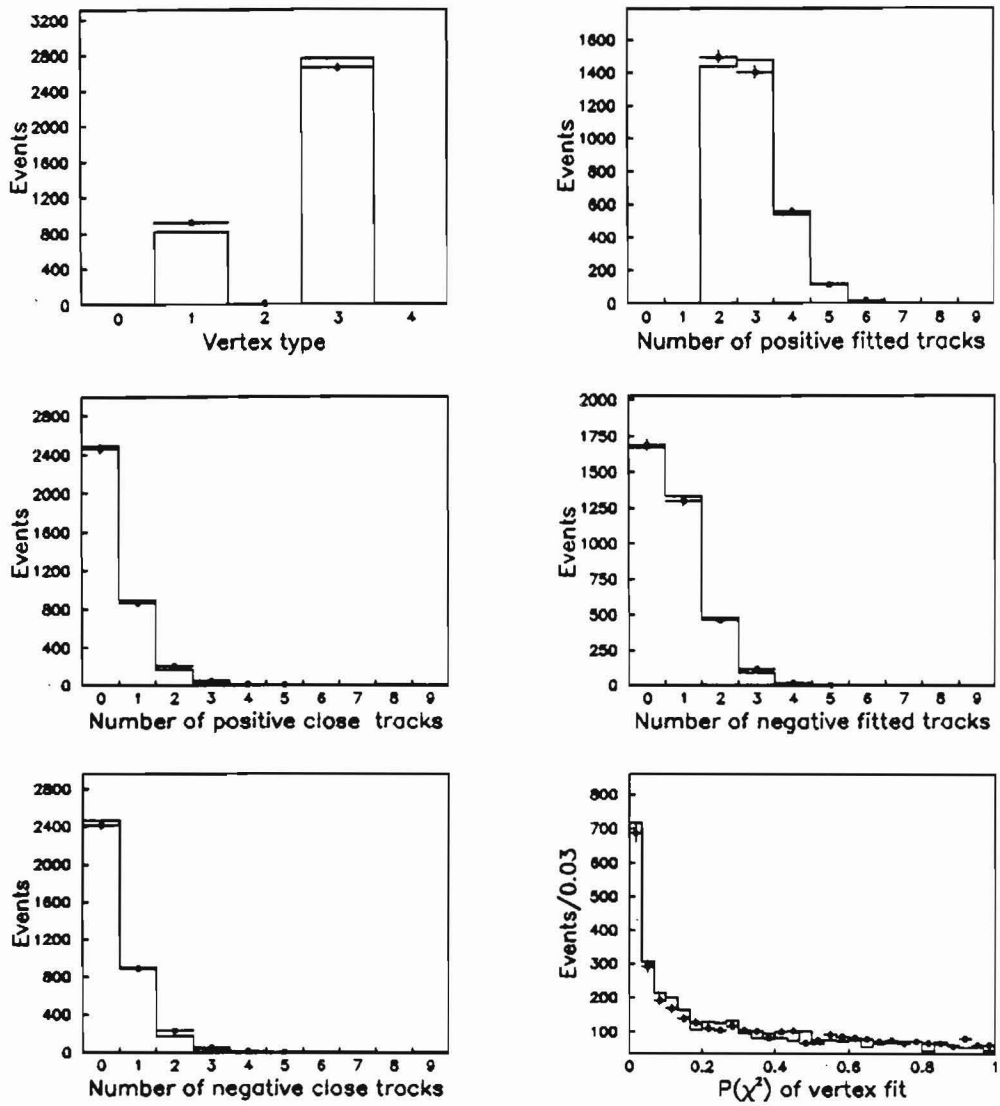


Comparison between the vertex fit in Monte Carlo (solid line) and data (solid circles) for deuterium.

**Fig. 3.5**

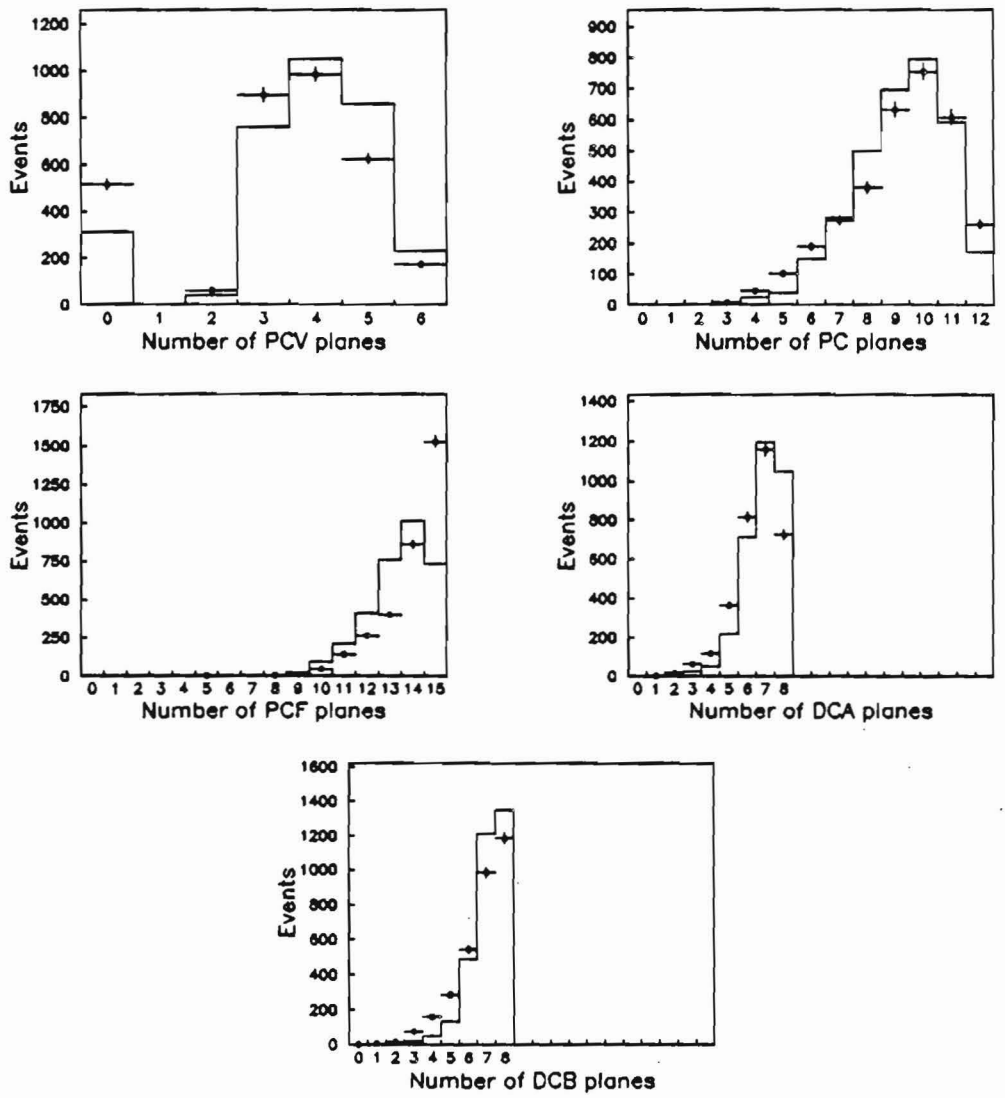


Number of chamber planes on the muon track in data (solid circles) and Monte Carlo (solid line) for hydrogen

**Fig. 3.6**

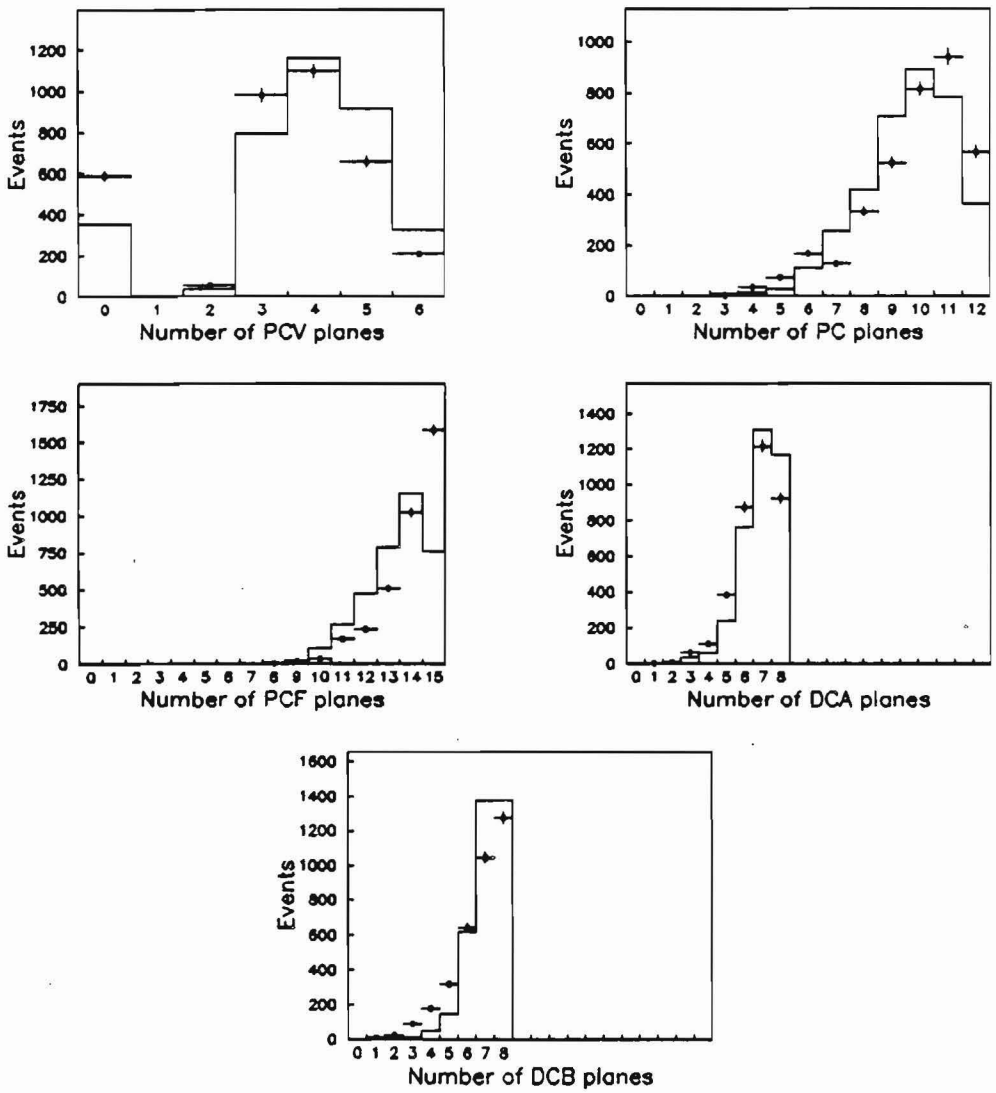


Number of chamber planes on the muon track in data (solid circles) and Monte Carlo (solid line) for deuterium

**Fig. 3.7**

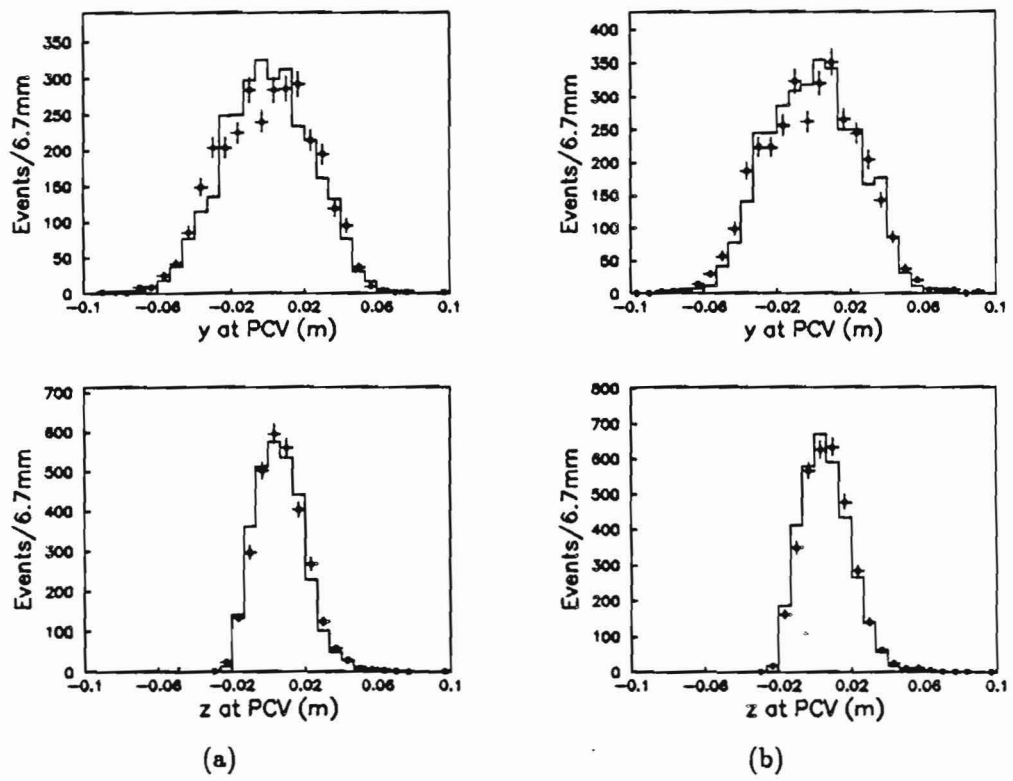


Data and reconstructed Monte Carlo position of the muon track at PCV. The solid line is reconstructed Monte Carlo and the solid circles are data. (a) Hydrogen. (b) Deuterium.

**Fig. 3.8**

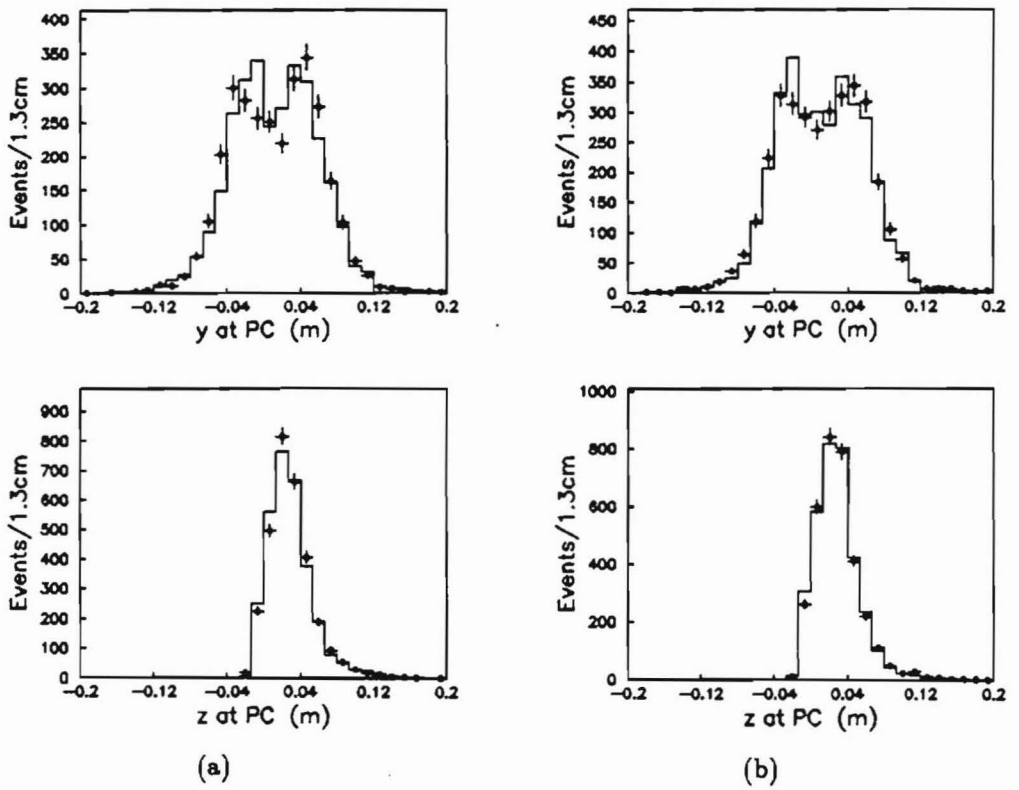


Data and reconstructed Monte Carlo position of the muon track at PC. The solid line is reconstructed Monte Carlo and the solid circles are data. (a) Hydrogen. (b) Deuterium.

**Fig. 3.9**

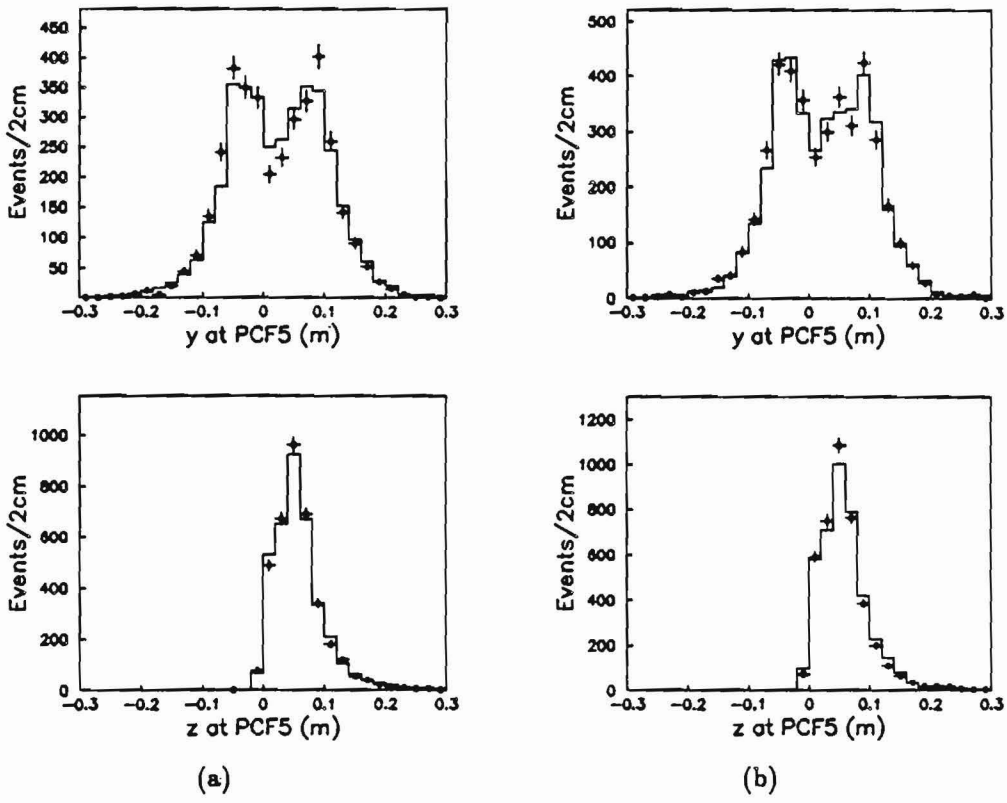


Data and reconstructed Monte Carlo position of the muon track at PCF5. The solid line is reconstructed Monte Carlo and the solid circles are data. (a) Hydrogen. (b) Deuterium.

**Fig. 3.10**

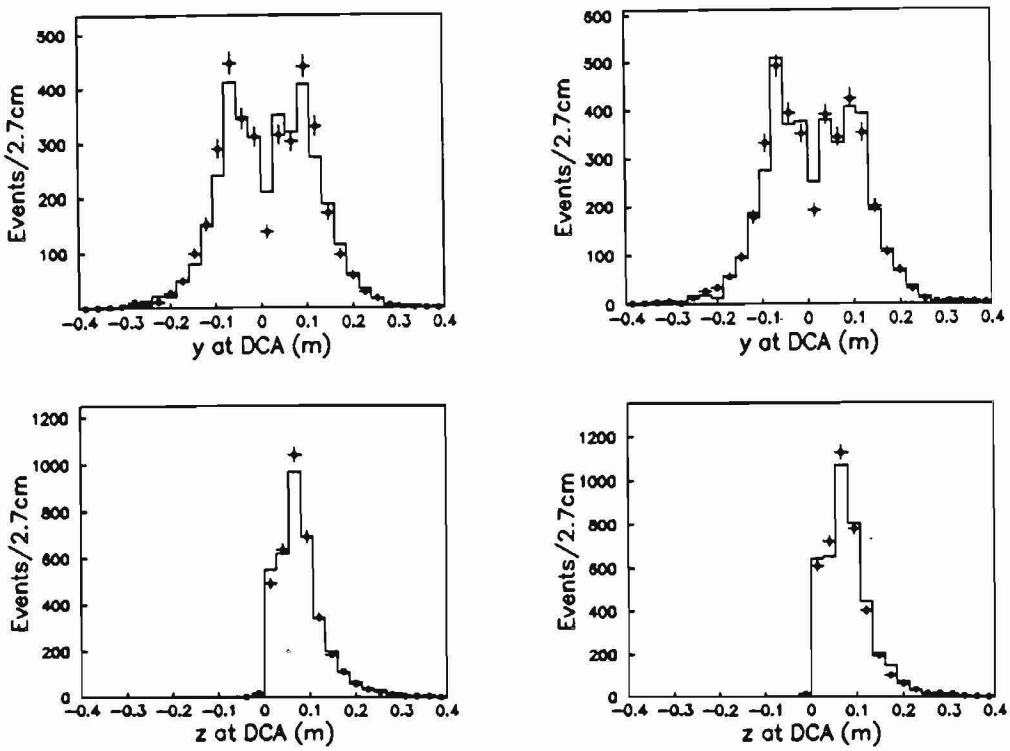


(a) (b)

Data and reconstructed Monte Carlo position of the muon track at DCA. The solid line is reconstructed Monte Carlo and the solid circles are data. (a) Hydrogen. (b) Deuterium.

**Fig. 3.11**

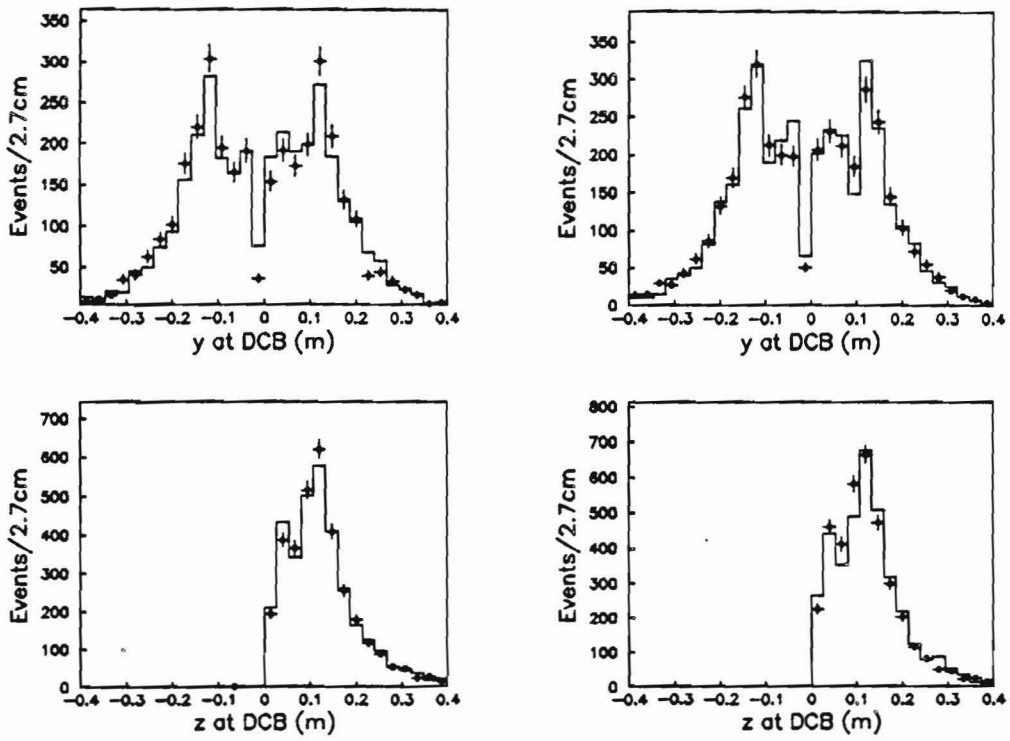


(a) (b)

Data and reconstructed Monte Carlo position of the muon track at DCB. The solid line is reconstructed Monte Carlo and the solid circles are data. (a) Hydrogen. (b) Deuterium.

**Fig. 3.12**

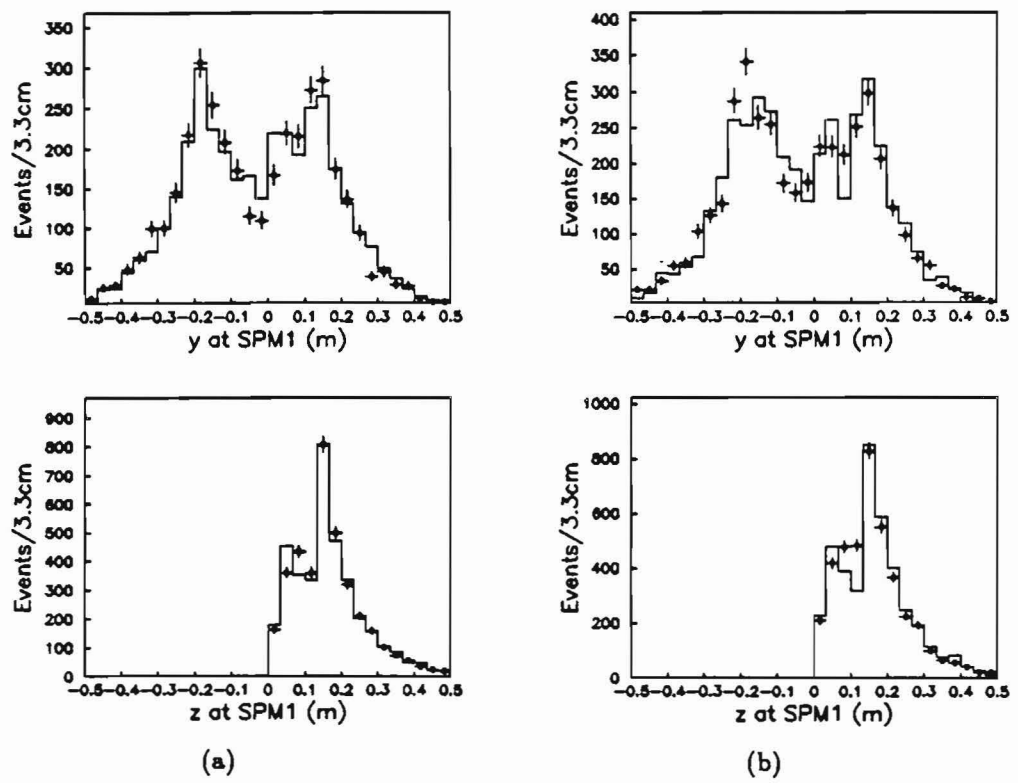


Data and reconstructed Monte Carlo position of the muon track at SPM1. The solid line is reconstructed Monte Carlo and the solid circles are data. (a) Hydrogen. (b) Deuterium.

**Fig. 3.13**

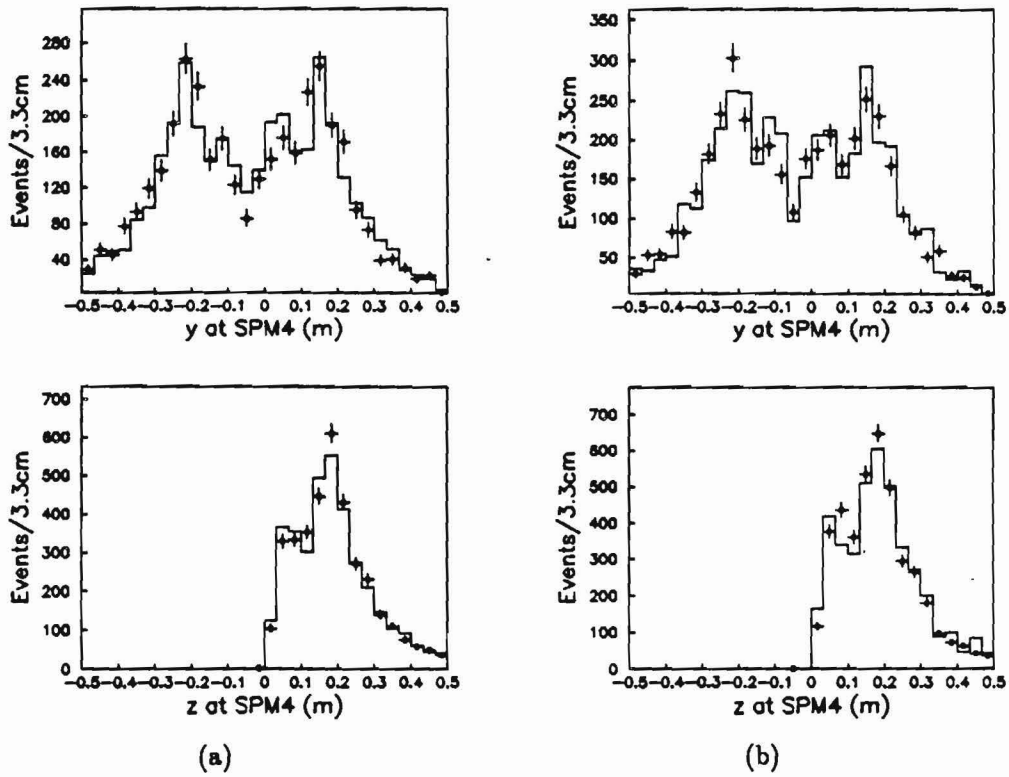


(a) (b)

Data and reconstructed Monte Carlo position of the muon track at SPM4. The solid line is reconstructed Monte Carlo and the solid circles are data. (a) Hydrogen. (b) Deuterium.

**Fig. 3.14**

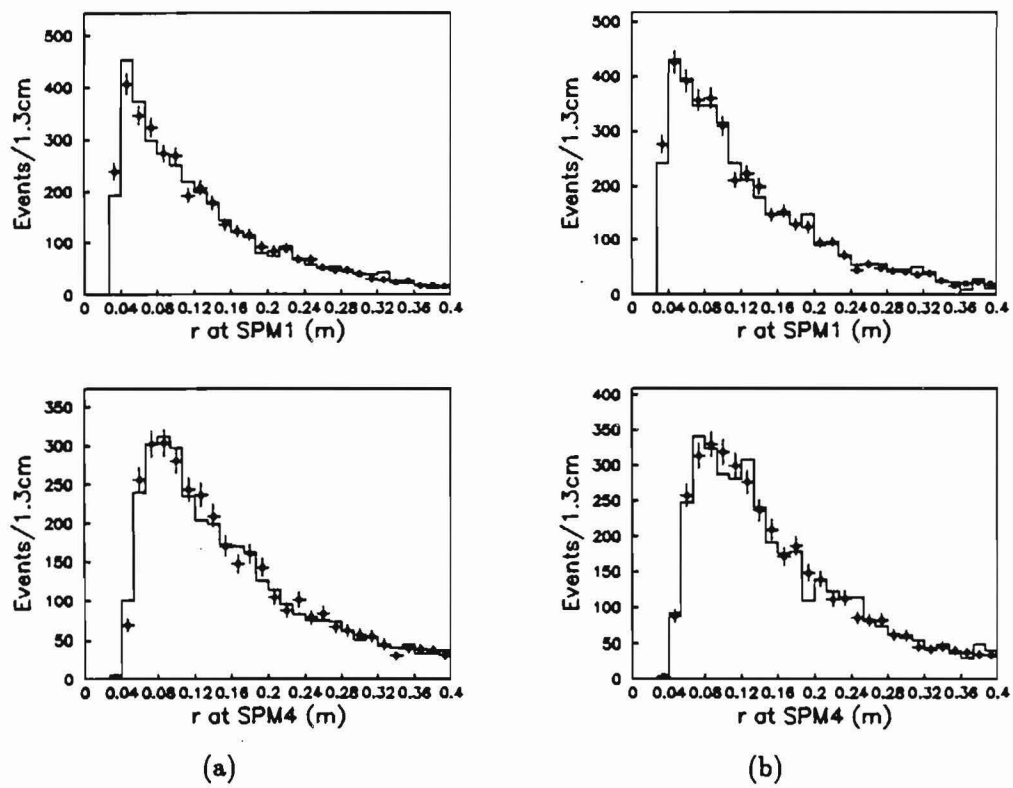


Data and reconstructed Monte Carlo distance of the muon track to the SMS veto region at SPM1 and SPM4. The solid line is reconstructed Monte Carlo and the solid circles are data. (a) Hydrogen. (b) Deuterium.

**Fig. 3.15**

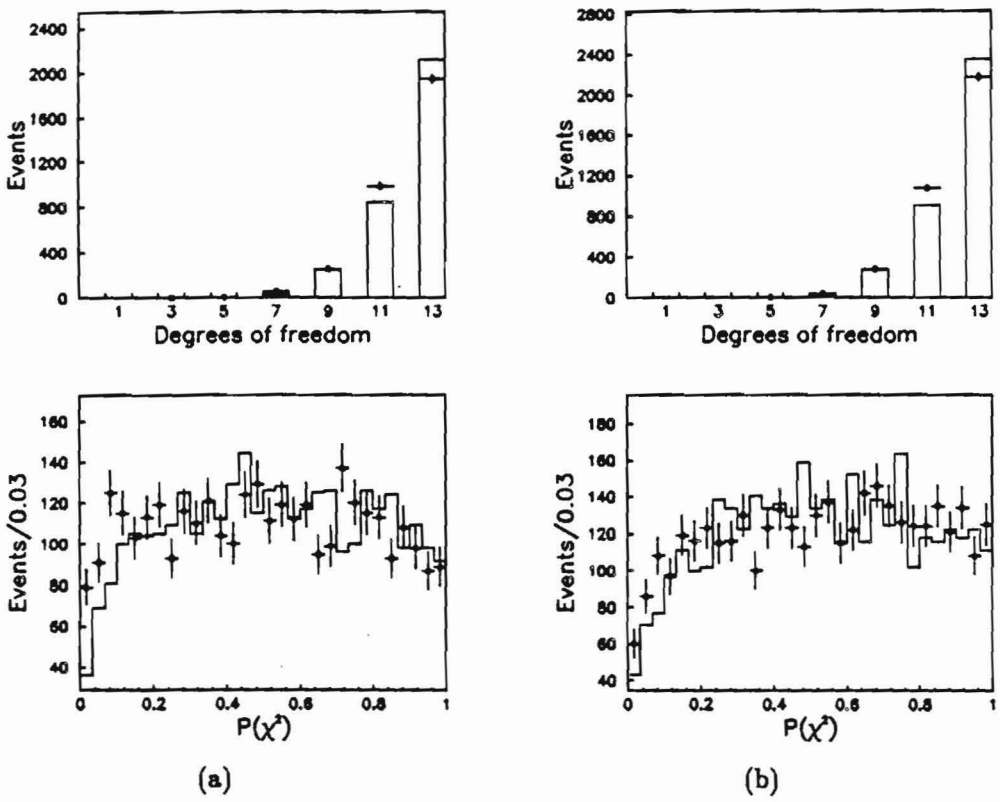


Number of degrees of freedom and $\chi^2$ probability of the fit on the muon track in data (solid circles) and Monte Carlo(solid line) for (a) hydrogen and (b) deuterium.

**Fig. 3.16**

Fig. 3.1 through Fig. 3.16 show detailed comparisons between Monte Carlo and data. More precisely, we compare *uncorrected* data against *reconstructed* Monte Carlo events. For each quantity under consideration, and for purpose of comparison, the Monte Carlo distribution and the corresponding data distribution are normalised to the number of entries in the histogram. The cuts applied to the data are the same as those applied to the reconstructed Monte Carlo sample. The only trigger requirement imposed on the Monte Carlo sample is that of the LAT acceptance. No simulation of the triggering system has been attempted, since the trigger efficiency can be extracted from SAT data.

When we compare basic kinematical quantities (Fig. 3.1 and Fig. 3.2), we can see that the agreement between Monte Carlo and data is reasonable. The data $\nu$ distributions have a small excess around 280 GeV compared to Monte Carlo. This is due to radiative events, present in the data but absent in Monte Carlo. The high $\nu$ excess in data will reflect itself in an excess of events in data at low $x_{bj}$.

The coordinates of the Monte Carlo primary vertex (Fig. 3.3) also agree reasonably well with the data primary vertex, and the quality of its fit (Fig. 3.4 and Fig. 3.5) is roughly the same in Monte Carlo and data.

Next we come to the muon track in the forward spectrometer. In Fig. 3.6 and Fig. 3.7, we show the number of detector planes at PCV, PC, PCF, DCA and DCB contributing to the muon track. It is clear that the data have, in comparison to the Monte Carlo, a higher frequency of absence of PCV planes on the muon trajectory. This is due to a PCV decoder problem that was present in the reconstruction of the LAT data but was absent in the reconstructed Monte Carlo sample.

The coordinates of the muon trajectory at each detector module is shown

in Fig. 3.8 through Fig. 3.15. It is noticeable that the the lower half of the detectors are missing. This is a consequence of our having imposed that the $z$–coordinate of the muon at SPM1 be greater then 0.02 m. The agreement between data and Monte Carlo is acceptable but not perfect.

Finally in Fig. 3.16, we present the goodness-of-fit of the muon trajectory in the forward spectrometer. First it should be pointed out that the number of degrees of freedoms (equal to the number of contributing detectors minus the five parameters necessary to parametrise the muon trajectory) is on the average smaller in data than in reconstructed Monte Carlo.

The $\chi^2$ probability (Fig. 3.16) of the muon-track fit should in principle be flat, both in data and in Monte Carlo (see the Appendix for a justification of this statement). But because of pattern-recognition problems, the track fitting procedure attempts to rescue tracks the $\chi^2$ probability of which is very low by dropping outlier hits (see (Salvarani,1991)). This results in a migration of the low probability tracks into the higher probability range. This is present both in Monte Carlo and in data, with a moderate agreement.

Having compared our reconstructed simulated data to that taken in 1987, we must come to the conclusion that the agreement is reasonable but not perfect. We shall nevertheless use our simulation program to extract correction factors to be applied to the data, but we shall be cautious as to the accuracy of these corrections. We shall come back to this point later, when we attempt at performing a cross-check of the reconstruction efficiency as obtained from the Monte Carlo program.

### 3.3 Beam normalisation

The determination of the beam flux is done by counting the number of

beams available for interaction during the live-time of the experiment. For this purpose, two techniques have been employed.

The first technique relies on event scalers which sum up the number of beam triggers without any consideration as to whether a large-angle trigger occurs. This number is the total number of beams available to the experiment, independent of time structure or phase space.

Since in our data analysis, it is required that the beam be reconstructed, it is clear that the above number will be an overestimate of the actual flux available. Clearly the reconstruction efficiency of the beam will be a function of the efficiency of the beam chambers. One method to get around this problem would be to estimate the beam losses by a Monte Carlo simulation where one would incorporate the beam-chambers efficiencies. We have not chosen this route, but instead we extracted the loss factor from the data themselves. This is the second technique, and it is based on the RBEAM trigger as described in the previous chapter. We recall that every $2^{\alpha}$ beam is recorded on a random basis by putting the beam signal in coincidence with a signal originating from a random generator. The power $\alpha$ is 18 for the hydrogen run and 19 for the deuterium run.

Our first check of the number of random beam triggers is to compare it with the event scalers. If we measure the quantity

$$\log_2 \left( \frac{\text{number of beams from events scalers}}{\text{number of RBEAM triggers}} \right)$$

then we must find it to be equal to the prescale power $\alpha$. This can be seen in Fig. 3.17.

The next step is to extract the beam-loss factor. RBEAM events are run through the same reconstruction chain as LAT events. In particular, the beam

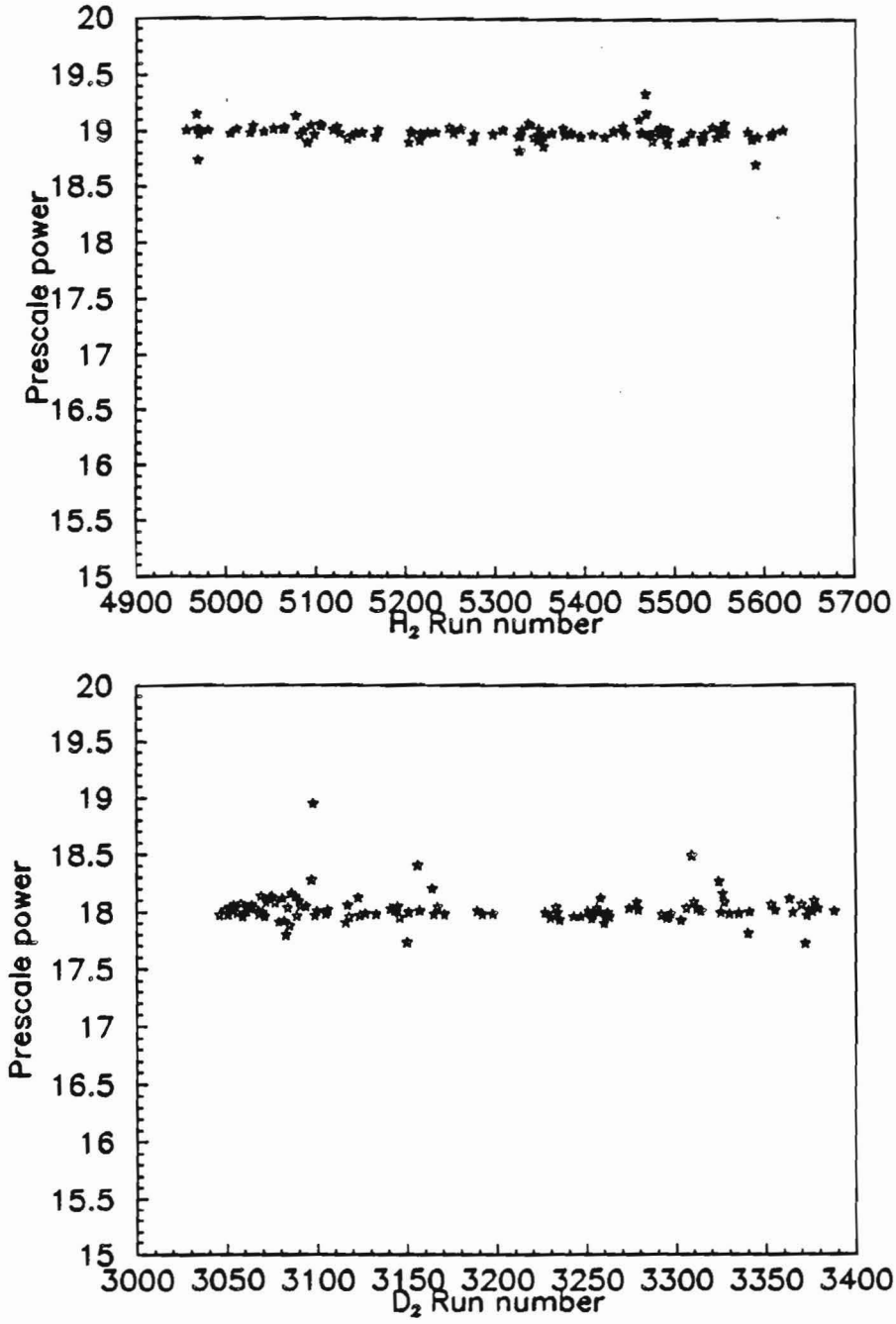


**RBEAM prescale powers for hydrogen and deuterium. The values are 19 for hydrogen and 18 for deuterium).**

**Fig. 3.17**

part of the filter program described earlier has been applied to RBEAM events

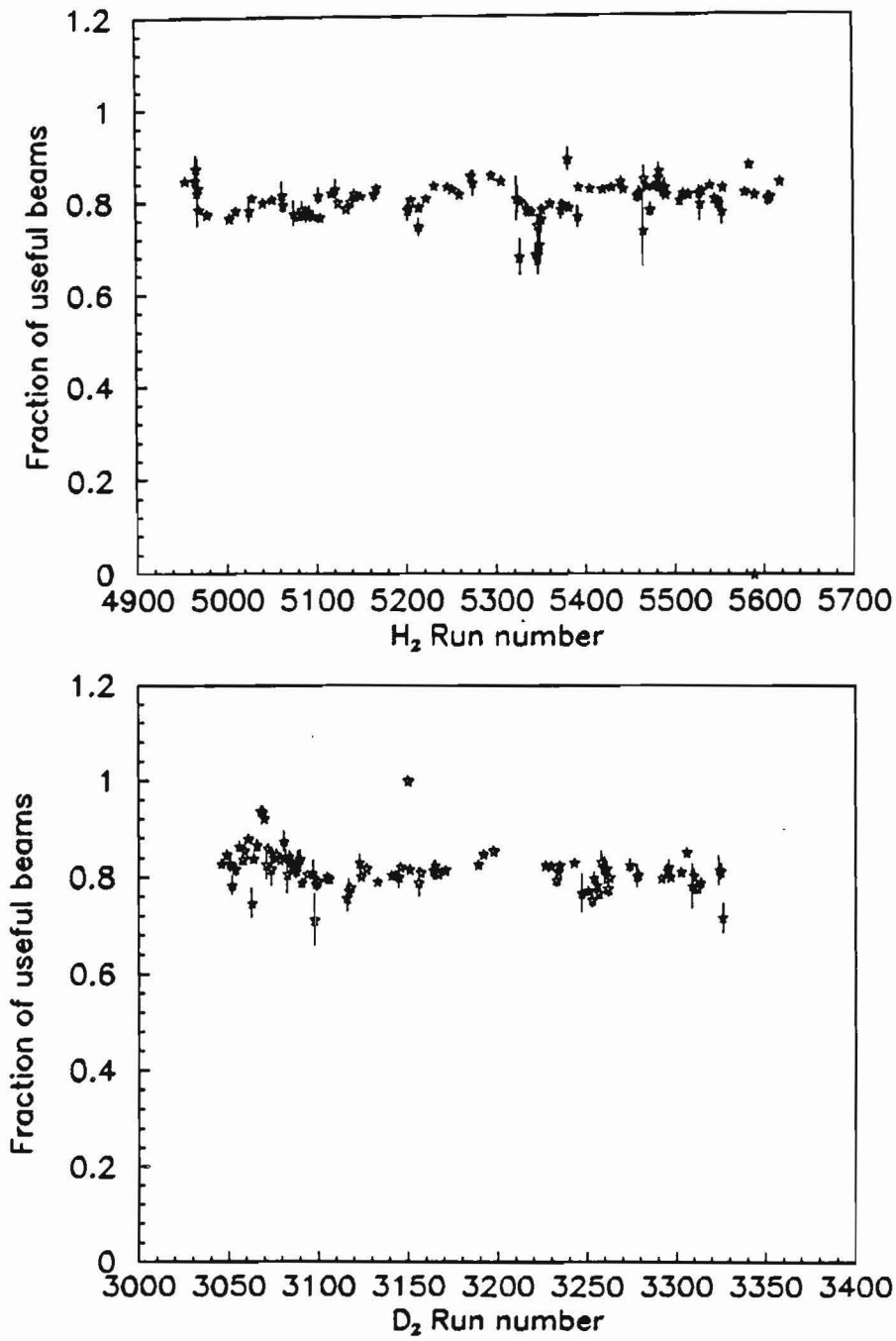


**Fraction of RBEAM events accepted by the filter as a function of run number.**

**Fig. 3.18**

and the latter are tested for acceptance or rejection. In Fig. 3.18, we have plotted the fraction of beams rejected by the filter as a function of run number.

The main source of losses of beams in the filter program is due to the presence of multibeam triggers.

In addition to this, we have checked the fraction of beams that do not fully traverse the target. This is achieved by projected the beam from beam station 4 to the upstream and downstream face of the target, along a straight line in the $xz$ plane and along a parabola in the $xy$ plane. Since the target is in a region of the CVM where the field changes rapidly, a parametrisation of an "effective field" has been done and the extrapolation taken as

$$y = y_{PBT4} + y'_{PBT4}(x - x_{PBT4}) + \frac{x^2}{2\alpha^3 R}$$

where

$$\alpha = \frac{p_z}{\sqrt{p_z^2 + p_y^2}}$$

$$R = \frac{p_{xy}[GeV]}{0.29972\, B_{eff}[Tesla]}$$

$$B_{eff} = 0.2305\, x + 2.805 \quad [Tesla]$$

We have found that among those beams which have been accepted by the filter, 0.56% do not traverse the full target, i.e. either miss the target altogether or miss the upstream face or the downstream face of the vessel. This number is comparable to the fraction of LAT events (0.5%) the beam of which fails to traverse the target. Since this is a small correction, we shall ignore it altogether.

Finally, for completeness, we show in Fig. 3.19, the distributions of the positions, slopes and momentum of the full beam available to the large-angle trigger.

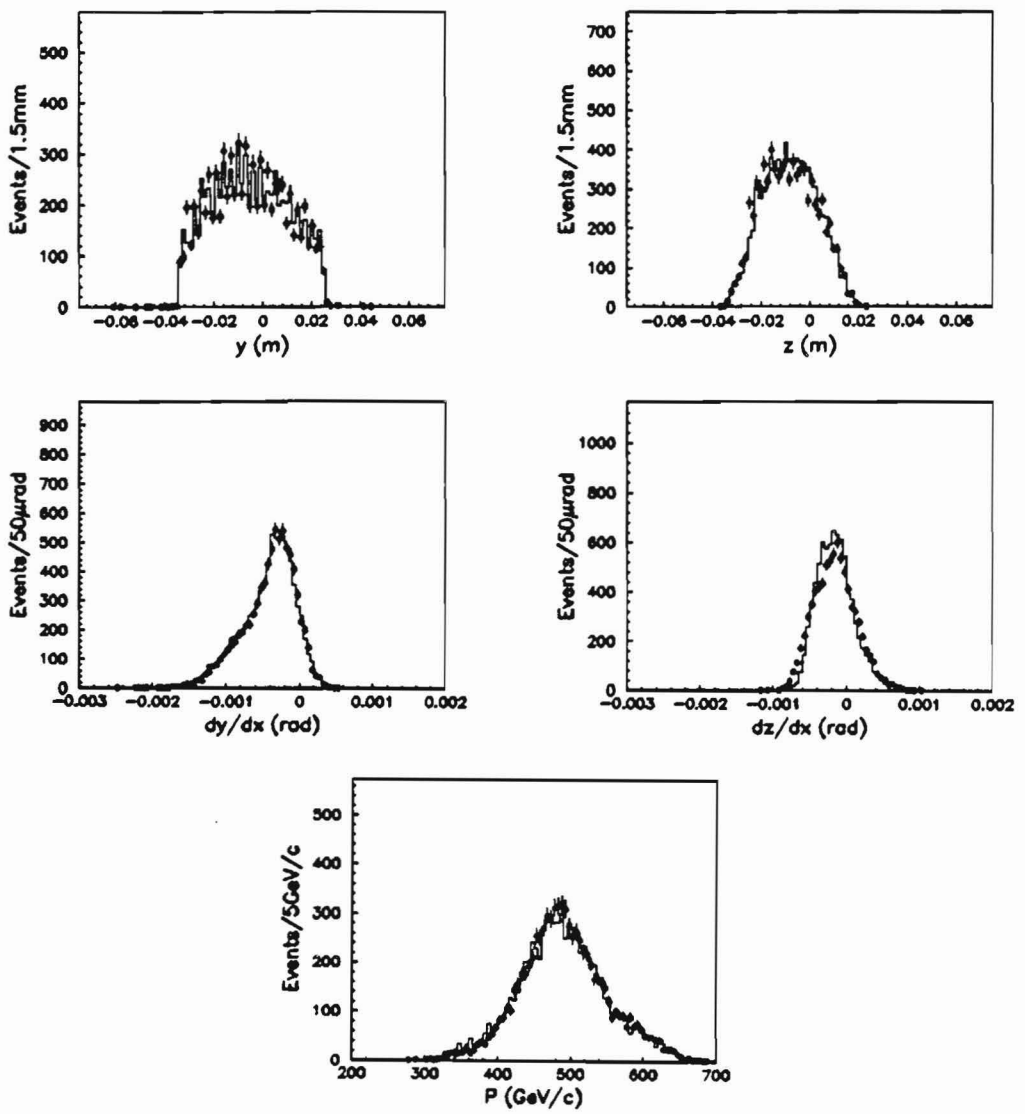


The positions, slopes and momentum of the beam at PBT4 for hydrogen (solid line) and deuterium (solid circles). These distributions are those of the RBEAM trigger.

**Fig. 3.19**

## 3.4 Trigger efficiency and trigger acceptance

The acceptance of the large-angle trigger in a given kinematical cell is the fraction of events it can register if the hardware works perfectly to the number of deeply inelastic events available in that cell. We make a distinction between trigger acceptance and trigger efficiency. The former is an intrinsic limit imposed by the geometry of the apparatus and depends mainly on the SMS veto system and the aperture of the SPM walls, whereas the latter is a measure of the performance of the hardware. In other words, it is defined as the probability that, given that an event is within the acceptance of the trigger, it is registered. This efficiency is limited mostly by the efficiency of the scintillators, the presence of noise, the timing of the signals and the vetoing caused by showers in the steel absorber.

We shall first discuss the acceptance of the large-angle trigger, then proceed to its efficiency.

### *3.4.1 Trigger acceptance*

We recall, from Chapter 2, that the large-angle trigger is defined by the following requirements :

- At least three out of four SPM walls should register hits (in reality three out of the four top walls or three out of the four bottom walls should be present; the occurrence of a muon which would fire say, two top walls and two bottom walls is almost impossible).

- There must be no hit in any of the planes of SMS1 and no hit in any the SMS4 planes.

The first requirement will tend to reject very high $\nu$ events for two rea-

sons. Firstly, such events are likely to have very oblique incidence on the first SPM station and therefore miss two or more the SPM walls. Secondly, if the scattered muon has too low an energy, it may never emerge from the steel absorber.

The second requirement will, on the other hand, reject small scattering-angle events. As a matter of fact, a crude estimate can give us an idea of the minimum scattering angle the muon must have in order to not traverse the SMS veto. Assume that the beam is exactly along the normal at the center of the veto, that the interaction occurs in the middle of the target and that the focusing is perfect. Then the minimum scattering angle that will bring the muon outside the SMS veto is the ratio of half the width of the veto to the distance between the center of the target and the first SMS veto, that is about 3.5 mrad.

A more accurate calculation of the acceptance of the large-angle trigger has been made with a Monte Carlo integration. Deeply inelastic events have been generated according to the cross-section in the kinematical range

$$Q^2 > 2.5\,\mathrm{GeV}^2/c^2$$

$$\nu > 40\,\mathrm{GeV}$$

We then require that

$$\nu > 50\,\mathrm{GeV}$$

$$\frac{\nu}{E} < 0.65$$

$$x_{bj} > 0.005$$

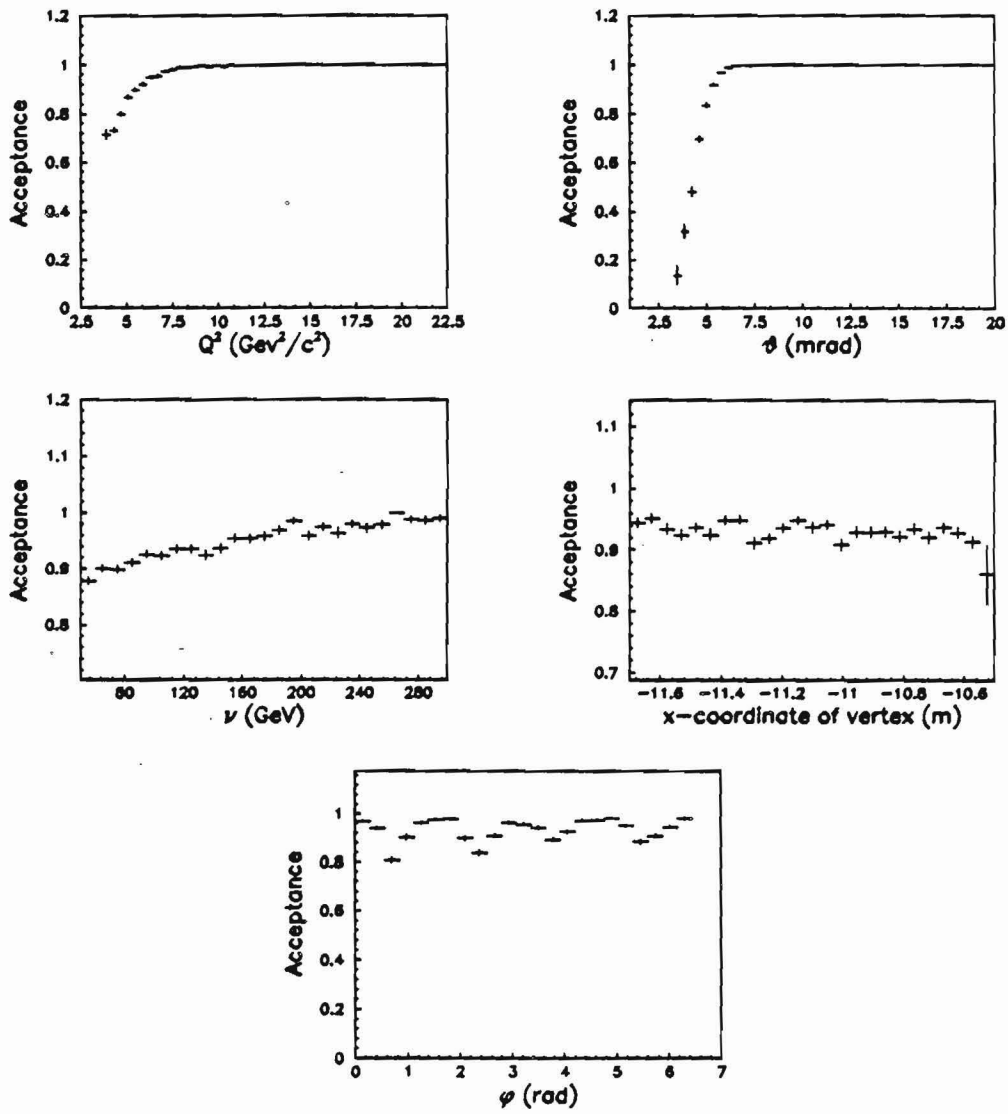


LAT acceptance as a function of kinematical variables, vertex position and asimuthal angle of the scattered muon around the beam.

**Fig. 3.20**

In the above kinematical range, we declare an event as accepted by the large angle trigger if all the following requirements are satisfied :

- The muon reaches SPM station three
- Its path does not traverse any of the SMS planes at station one and does not traverse any of the SMS planes at station four.

The full acceptance of the trigger is shown in Fig. 3.20. For each variable, we relax the corresponding range in order to show the behaviour of the acceptance on a wider range of the kinematical variable. The dependence on the scattering angle $\theta$ is very clear; the acceptance of the trigger is non-zero for scattering angles $\theta$ above 3 mrad and increases as $\theta$ increases, to reach 100% at $\theta = 6.5$ mrad.

There is a small dependence on $\nu$ and virtually no dependence on the vertex position, which leads to a primary kinematical dependence on $Q^2$.

The dependence of the acceptance on $\varphi$, the azimuthal angle of the scattered muon direction around the beam direction, reflects the simple fact that the beam veto region is a square.

Additional cuts will be applied in our analysis in order to select a clean sample of events. Because of self-vetoing in the SMS planes, events where the muon has a closest distance of approach to the SMS veto stations ($r_\mu$) less than 0.03 m are rejected. Moreover, the behaviour of the lower half of the SPM walls was found to be faulty, and this forces us to reject events where the z-coordinate of the muon trajectory at SPM1 ($z_\mu$) is less then 0.02 m. Finally, the efficiency for reconstructing the muon when its trajectory traverses a central vertical stripe of the drift chambers is very low, which leads us to discard events where the y-coordinate of the muon impact point at SPM1 ($z_\mu$) is between $-0.08$ m

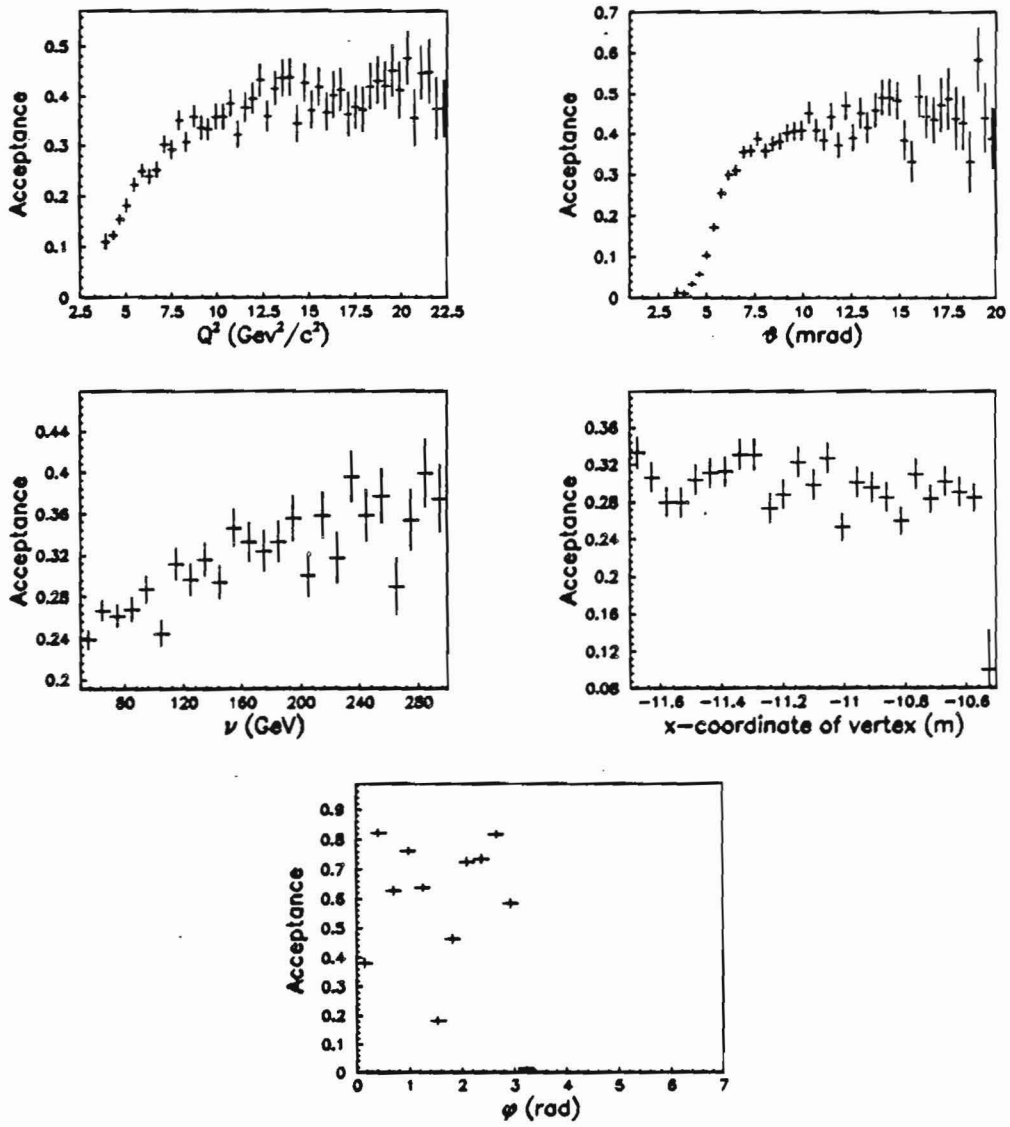


**Acceptance of the LAT with superveto software as a function of kinematical variables, vertex position and asimuthal angle of the scattered muon around the beam.**

**Fig. 3.21**

and 0.02 m. These cuts will be discussed in subsequent sections, but for now we wish to show the acceptance that we obtain when the superveto so defined is applied. In Fig. 3.21, we have plotted the fraction of events surviving the superveto to the number of events generated. If we consider the $\theta$-dependence of this acceptance, we can see that it reaches a plateau of 0.5. This is due

to the fact that we are accepting events only in the upper half of the muon system. The $\phi$-dependence shows a dip at $\phi = \pi/2$ refecting the removal of the vertical stripe we mentioned earlier.

### 3.4.2 *Trigger efficiency*

In this section, we shall investigate the performance of the large-angle trigger. It stands to reason that the efficiency of the large-angle trigger should be defined as the ratio of the number of events it accepts to the number of events it should accept. The events that should be accepted by the trigger are those which fall within its acceptance. Indeed, if the hardware worked perfectly, this efficiency should be equal to one. Reduction of the efficiency can occur when, for instance, the scintillation counters have a low efficiency. In the 1987-1988 data-taking period, an unusually low efficiency resulting from a mis-timing of the scintillator signals led to a substantial loss of those events for which the scattered muon traverses the bottom SPM paddles. A measurement of the trigger efficiency will be made and a strategy for dealing with this problem will be presented. We recall, from Chapter 2, that the LAT is constructed by an SMS veto requirement and a demand that at least three out of four SPM walls be present. The latter requirement will be referred to as $\mu_a.\mu_b$.

In order to perform a measurement of the LAT efficiency, we must have a sample of events, independent of those accepted by the trigger under study, from which we can select a subset in which the events satisfy the appropriate requirements of the large-angle trigger. This sample will consists of two classes : those events in which the LAT was actually registered and those for which it was not registered. The actual registration of the large-angle trigger is indicated by the presence of a hardware trigger bit recorded during the data-taking phase.

The reference sample is provided by a selected set of SAT events on which quality constraints have been imposed. More precisely, we reject those SAT events in which the beam leaves hits in the SVJs or the SVW, or fails to traverse the full length of the target, or is accompanied by another beam

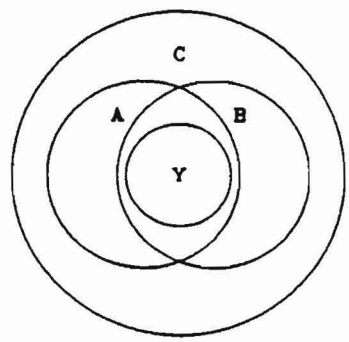


**Venn diagrams describing the method used in the measurement of the LAT efficiency. The meaning of the various sets is described in the text.**

**Fig. 3.22**

muon. These demands leave us with a set of SAT events that we shall call C (in reality, two additional requirements have been made, namely $z_\mu > 0.02m$ and $r_\mu > 0.02m$, the rationale of which will become clear in a moment). Bearing in mind the definition of the large-angle trigger, we summarise the various possibilities in Fig. 3.22. We shall denote the set of trial events in which the LAT-veto condition is satisfied by B (B is a subset of C). The subset of those events characterised by the presence of $\mu_a.\mu_b$ is denoted by A. Finally, the events where the LAT hardware bit is on form a set that we shall call Y. Now, according to Fig. 3.22 we have

$$Y \subset A$$

$$Y \subset B$$

This assumption is justified by the contingency tables of Table 3.1. That $Y \subset A$ is quite clear. And $Y \subset B$ is also a very good approximation, since the number of events which are in Y and not in B is negligible. The overall

**Table 3.1**

| | | *SMS veto* 0 | *SMS veto* 1 |
|---|---|---|---|
| *LAT* | 0 | 15 | 93 |
| *bit* | 1 | 2365 | 12 |

| | | $\mu_a \cdot \mu_b$ 0 | $\mu_a \cdot \mu_b$ 1 |
|---|---|---|---|
| *LAT* | 0 | 13 | 95 |
| *bit* | 1 | 0 | 2377 |

(*a*)

| | | *SMS veto* 0 | *SMS veto* 1 |
|---|---|---|---|
| *LAT* | 0 | 15 | 53 |
| *bit* | 1 | 1259 | 3 |

| | | $\mu_a \cdot \mu_b$ 0 | $\mu_a \cdot \mu_b$ 1 |
|---|---|---|---|
| *LAT* | 0 | 5 | 63 |
| *bit* | 1 | 0 | 1262 |

(*b*)

**Correlation tables between the hardware LAT trigger bit and the SMS veto system and $\mu_a \cdot \mu_b$ for (a) hydrogen and (b) deuterium. For the LAT trigger bit, 0 means that the latter is not set and 1 that it is set. For the SMS veto, 0 means that no SMS plane had a hit, and 1 that at least 1 SMS plane had a hit.**

efficiency of the LAT is

$$\varepsilon = \frac{|Y|}{|C|}$$

This overall efficiency can be written as the product of three efficiencies, each one representing a particular aspect of the the triggering system. We define

$$\varepsilon_1 = \frac{|Y|}{|A \cap B|}$$

$$\varepsilon_2 = \frac{|A|}{|C|}$$

$$\varepsilon_3 = \frac{|A \cap B|}{|A|}$$

and clearly

$$\varepsilon = \varepsilon_1 \varepsilon_2 \varepsilon_3$$

Keeping in mind the fact that $Y \subset A$ and $Y \subset B$, the above efficiencies have the following meaning; $\varepsilon_1$ is the *electronic* efficiency, i.e. the probability that, given that all the appropriate logical requirements are satisfied, the trigger signal

will be generated; $\varepsilon_2$ is the probability that $\mu_a.\mu_b$ will be satisfied, given that a muon track has traversed the SPM stations; this quantity is an indication of the underlying scintillator efficiency; finally, $\varepsilon_3$ is the self-veto insensitivity. Whereas we expect $\varepsilon_1$ and $\varepsilon_2$ to be equal to 1, we do not expect $\varepsilon_3$ to be unity. This stems from the observation that the muon will generate showers and companion $\delta$-rays in the absorbers (primarily in the iron absorber) which have a non-zero probability of impacting the SMS veto system despite the fact that the muon trajectory does not traverse the veto region. It stands to reason that the closer the muon path is to the boundary of the veto, the smaller $\varepsilon_3$. On the other hand, the self-veto insensitivity is expected to go to one the further the muon trajectory is from the edge of the SMS system. In contrast with $\varepsilon_3$, which is directly related to background processes preventing the LAT from registering events where the outgoing muon travels too close to the veto, $\varepsilon_1$ and $\varepsilon_2$ are indicators of the performance of the hardware proper. Their deviating significantly from unity would indicate a pathological behaviour of the triggering system.

Consider first the electronic efficiency. If, in the definition of the set $C$, we remove the requirement that $z_\mu$ be greater than 0.02m, and plot $\varepsilon_1$ against $z_\mu$ (Fig. 3.23a), we observe an abnormal drop of the electronic efficiency as we cross the boundary separating the upper SPM walls from the lower SPM walls; this drop is followed by an increase in $\varepsilon_1$ as $z_\mu$ becomes more negative. The electronic efficiency of the upper wall is very close to 1. Investigations led us to think that this $z_\mu$-dependence of the electronic efficiency for the lower SPM scintillators originates from a relative-timing drift between the SPM counters and the radio-frequency of the accelerator. The phase of the latter was locked by a phase-lock module which used as a time reference a signal generated by four small counters located at the end of the muon system. During the run one

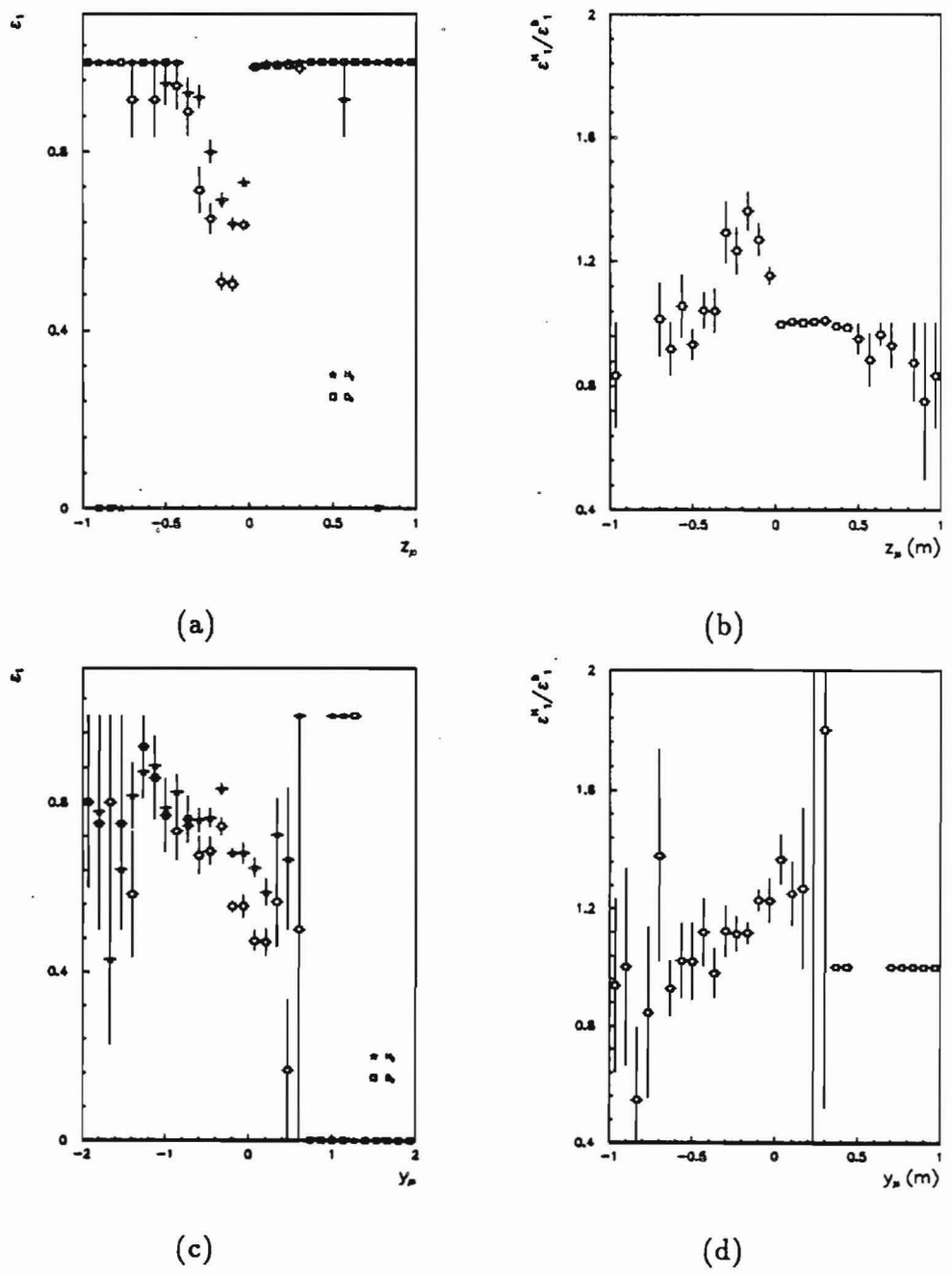


Dependence of the electronic efficiency on $y_\mu$ and $z_\mu$.

**Fig. 3.23**

of the counters died, and after the phase-lock counters were brought back into operation, it was noticed that the locked radio-frequency was 3 ns late. This time-drift was compensated, but we believe that the timing of the lower SPM

counters was already close to the rapidly falling edge of their delay curve and the 3 ns compensation was not sufficient to bring them back to full efficiency.

The inclusion of events which result from the LAT having been enabled by the bottom counters would not, in principle, be a problem, were such an efficiency to depend only on $z_\mu$ and were it to be stable throughout the run. But as shown in Fig. 3.23c,d, it is very clear that it depends on $y_\mu$, indicating a counter-to-counter variation of the electronic efficiency; and to complicate matters further, it has varied substantially between the deuterium run and the hydrogen run. The systematic error which would result from an attempt at correcting for such an effect would be undesirably large; *ergo*, our strategy will be to discard LAT events where the muon has traversed the bottom SPM counters. This is the justification for imposing the aforementioned $z_\mu$ cut, namely $z_\mu > 0.02\,\mathrm{m}$. In the rest of this work, this cut will always be present, in addition to other cuts that will be imposed on the final sample.

This main cut having been imposed on our samples, it still remains to be shown that the trigger, when only the upper SPM are taken into account, displays a reasonable performance. To this end, we study the dependence of the electronic efficiency on $y_\mu$ and $z_\mu$.

To determine $\varepsilon_1$ and $\varepsilon_2$, we proceed as follows. We divide the $(y_\mu, z_\mu)$ plane into $m$ $z_\mu$ slices. Each $z_\mu$ slice is divided into $l$ $y_\mu$ cells. In each (k,j) cell $(1 \leq k \leq m,\ 1 \leq j \leq m,)$, let $s_{kj}$ be the number of successes and $t_{kj}$ be the number of trials. In this cell, the efficiency is estimated by

$$p_{kj} = \frac{s_{kj}}{t_{kj}}$$

Under the hypothesis that, for given $k$, all $p_{kj}$ are the same, the efficiency in

**Table 3.2**

| $< z_\mu >$ (m) | $\varepsilon_1$ | $\chi^2$ | $\chi^2_{0.95}$ | $n_{dof}$ | $\sigma$ |
|---|---|---|---|---|---|
| 0.026 | 0.994 | 3.379 | 12.592 | 6 | 0.006 |
| 0.044 | 0.997 | 8.064 | 16.919 | 9 | 0.002 |
| 0.083 | 1.000 | - | - | - | - |
| 0.162 | 0.997 | 31.559 | 23.685 | 14 | 0.002 |
| 0.310 | 1.000 | - | - | - | - |
| 0.551 | 1.000 | - | - | - | - |
| 1.138 | 1.000 | - | - | - | - |

(a)

| $< z_\mu >$ (m) | $\varepsilon_1$ | $\chi^2$ | $\chi^2_{0.95}$ | $n_{dof}$ | $\sigma$ |
|---|---|---|---|---|---|
| 0.027 | 0.980 | 16.103 | 12.592 | 6 | 0.014 |
| 0.046 | 0.992 | 4.662 | 12.592 | 6 | 0.006 |
| 0.083 | 0.987 | 4.495 | 14.067 | 7 | 0.006 |
| 0.162 | 0.996 | 8.070 | 23.685 | 14 | 0.003 |
| 0.304 | 0.989 | 5.913 | 21.026 | 12 | 0.011 |
| 0.563 | 1.000 | - | - | - | - |
| 1.074 | 1.000 | - | - | - | - |

(b)

**Electronic efficiency for (a) hydrogen and (b) deuterium.**

slice $k$ can be estimated by

$$p_k = \frac{\sum_{j=1}^{l} s_{kj}}{\sum_{j=1}^{l} t_{kj}} \tag{3.5}$$

The quantity used to test the hypothesis that the efficiencies $p_{kj}$ in slice $k$ are the same is

$$\chi^2 = \sum_{j=1}^{l} \frac{(s_{kj} - p_k t_{kj})^2}{t_{kj} p_k (1 - p_k)}$$

which follows a $\chi^2$ distribution with $l - 1$ degrees of freedom. This reduction by 1 of the number of degrees of freedom stems from the constraint given by Eq. 3.5.

In table Table 3.2, we summarise the measurements we performed on the electronic efficiency $\varepsilon_1$. The first column is the average $z_\mu$ in a given $z_\mu$ slice. the second column is the efficiency in that $z_\mu$ slice (i.e. $p_k$). The third column

is the value of $\chi^2$ as defined previously, with its number of degrees of freedom given in column four. Finally, $\sigma$, in the fifth column, is the statistical error on $\varepsilon_1$, estimated by

$$\sigma = \sqrt{\frac{\varepsilon_1(1-\varepsilon_1)}{t}}$$

where $t$ is the number of trials in the slice under consideration. Entries where $\varepsilon_1$ is exactly equal to one are not associated with any statistical quantity.

For hydrogen, we observe little dependence on $y_\mu$, except perhaps at $y_\mu = 0.162\,\mathrm{m}$, where the $\chi^2$ exceeds the $\chi^2$ at 95%. But there $\varepsilon_1$ is 0.997, which, in this analysis, we regard as a reasonable value for any efficiency. Consequently, we may conclude that the efficiency is uniform in $y_\mu$. A merging of the $z_\mu$ slices yields an estimate of $\varepsilon_1$ of $0.998 \pm 0.001$. The corresponding $\chi^2$ is around 3.53, with 6 degrees of freedom, which is less than the 95% $\chi^2$ (12.59). This shows that there is no detectable $z_\mu$ dependence in the hydrogen data.

For deuterium, the situation is somewhat worse. The electronic efficiency is low at $z_\mu = 0.027$ (0.98), the corresponding $\chi^2$ being larger than the critical $\chi^2$. However, if we nevertheless merge the $z_\mu$ slices and compute the overall $\varepsilon_1$, we find a value of $0.991 \pm 0.003$, with a $\chi^2$ of 3.75 with 6 degrees of freedom.

In view of the small deviation of these numbers from one, we shall not make any corrections to correct for hardware or electronic inefficiencies.

The study of $\varepsilon_2$, the $\mu_a.\mu_b$ efficiency, proceeds in a similar manner. Results are summarised in Table 3.3.

The hydrogen data show little dependence on $y_\mu$, except at $y_\mu = 0.083$ where $\varepsilon_2$ is 0.992, which we again regard as an almost perfect efficiency. An overall estimate of $\varepsilon_3$ is $0.995 \pm 0.001$ with a $\chi^2$ of 5.75, with 6 degrees of

**Table 3.3**

| $< z_\mu >$ (m) | $\varepsilon_2$ | $\chi^2$ | $\chi^2_{0.95}$ | $n_{dof}$ | $\sigma$ |
|---|---|---|---|---|---|
| 0.026 | 0.994 | 10.861 | 12.592 | 6 | 0.006 |
| 0.044 | 0.993 | 4.576 | 16.919 | 9 | 0.003 |
| 0.083 | 0.992 | 25.502 | 14.067 | 7 | 0.003 |
| 0.162 | 0.999 | 6.902 | 23.685 | 14 | 0.001 |
| 0.310 | 0.987 | 7.321 | 21.026 | 12 | 0.009 |
| 0.564 | 1.000 | - | - | - | - |
| 1.156 | 1.000 | - | - | - | - |

(a)

| $< z_\mu >$ (m) | $\varepsilon_2$ | $\chi^2$ | $\chi^2_{0.95}$ | $n_{dof}$ | $\sigma$ |
|---|---|---|---|---|---|
| 0.027 | 0.971 | 10.337 | 12.592 | 6 | 0.017 |
| 0.046 | 0.996 | 1.918 | 12.592 | 6 | 0.004 |
| 0.083 | 1.000 | - | - | - | - |
| 0.162 | 0.998 | 7.046 | 23.685 | 14 | 0.002 |
| 0.305 | 1.000 | - | - | - | - |
| 0.570 | 1.000 | - | - | - | - |
| 1.074 | 1.000 | - | - | - | - |

(b)

**$\mu_a$.$\mu_b$ efficiency for (a) hydrogen and (b) deuterium.**

freedom.

The deuterium sample shows a low value of $\varepsilon_2$ (0.971) in the first $z_\mu$ slice. The merging of the $z_\mu$ slices yields an average value of $\varepsilon_2$ of 0.996 with a $\chi^2$ of 19.9 with 6 degrees of freedom, against a critical $\chi^2$ of 12.59.

The self-veto insensitivity, $\varepsilon_3$, is expected to depend primarily on the distance between the outgoing-muon trajectory and the veto boundary. The geometry of the latter is most complex, since the veto is a logical *or* of 4 SMS planes, and in principle includes a geometrical contribution from the SMS phototubes. In spite of this complication, we shall assume that the behaviour of $\varepsilon_3$ can be fully described by two variables, namely $r_\mu$ and $\varphi$. $r_\mu$ is the minimum distance of approach of the muon path with respect to the overlap of the planes of SMS1 and the overlap of the planes of SMS4. $\varphi$ is the azimuthal

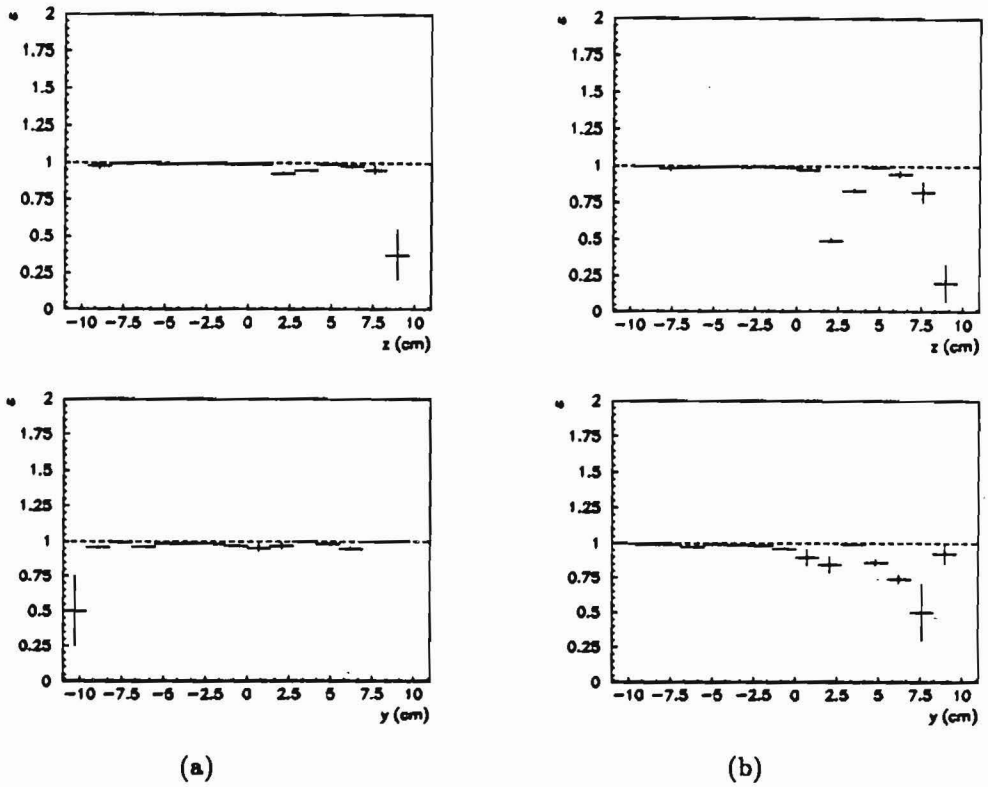


Efficiency of SMS latches at station 1 for (a) hydrogen and (b) deuterium.

**Fig. 3.24**

angle of the outgoing muon with respect to the beam axis. When $r_\mu$ is large, we expect little dependence of $\varepsilon_3$ on $\varphi$.

The method that we wished to use to measure $\varepsilon_3$ is to check the presence of hits in the SMS planes at station one and four and declare an event to be self-veto if the muon does not traverse the veto and at the same time any SMS plane at station one or four registers a hit.

However, it was found that the SMS latches had an inefficient behaviour at station 1. This is clearly a problem, since we rely on the information they provide to determine whether there are hits in the SMS planes when the muon trajectory goes outside the veto. The efficiency of the latches is shown in Fig. 3.24 and Fig. 3.25, as a function of the coordinates of the muon impact

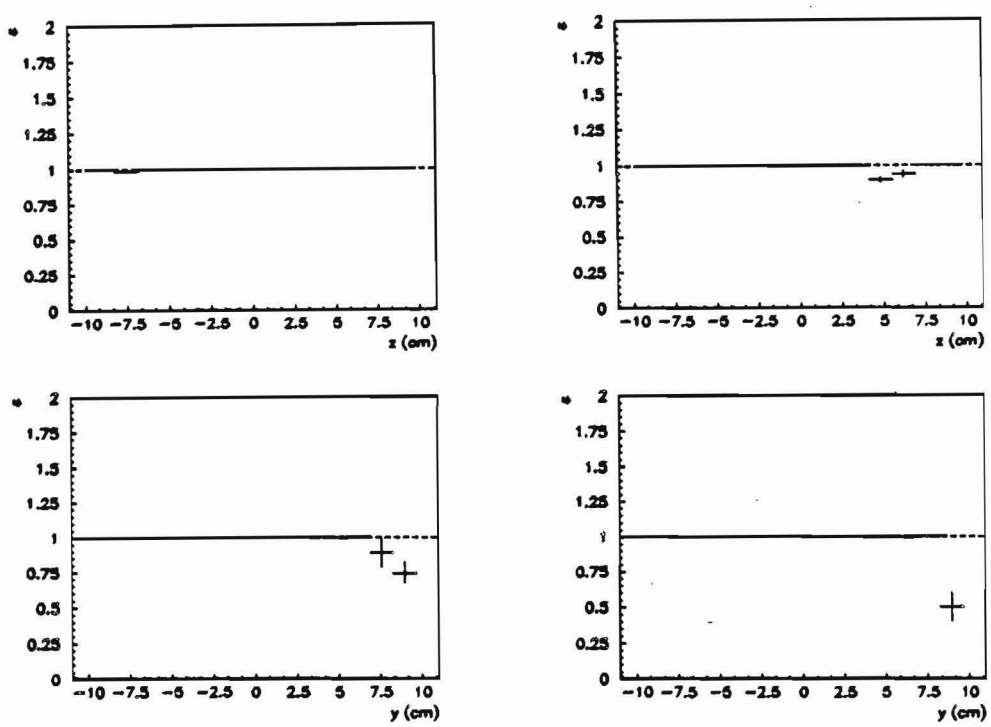


(a) (b)

**Efficiency of SMS latches at station 4 for (a) hydrogen and (b) deuterium.**

**Fig. 3.25**

point at SPM1. The latter measurement was obtained by constraining the muon to traverse all SMS stations and by checking the appearance of at least a hit at each SMS station.

To illustrate the impact of the SMS latch inefficiencies on the measurement of $\varepsilon_3$, we have determined $\varepsilon_3$ by restricting the muon trajectory to the first quadrant. Intuitively, because the latches are very inefficient in this region, we expect $\varepsilon_3$ to be higher than it would be in the third quadrant. A comparison between Fig. 3.26 and Fig. 3.27 shows that this is indeed the case. We are therefore coerced to using the third quadrant to determine the $\varepsilon_3$. Such a measurement is shown in Fig. 3.26, as a function of $r_\mu$. For illustrative purpose, we have parametrised $\varepsilon_3$ in the form

$$\varepsilon_3 = P_1 - P_2\, e^{-P_3 r_\mu} \tag{3.6}$$

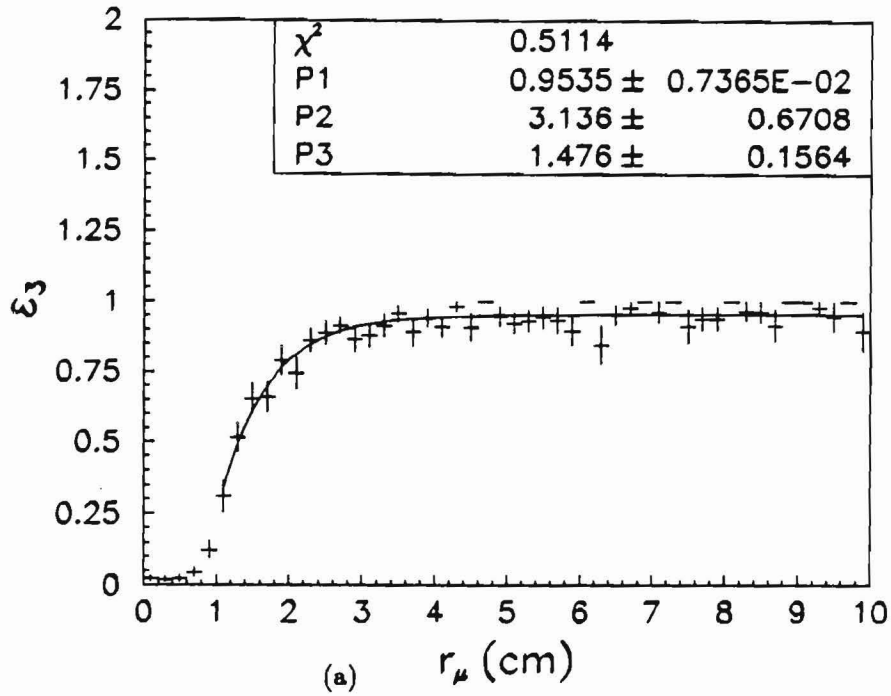


(a)

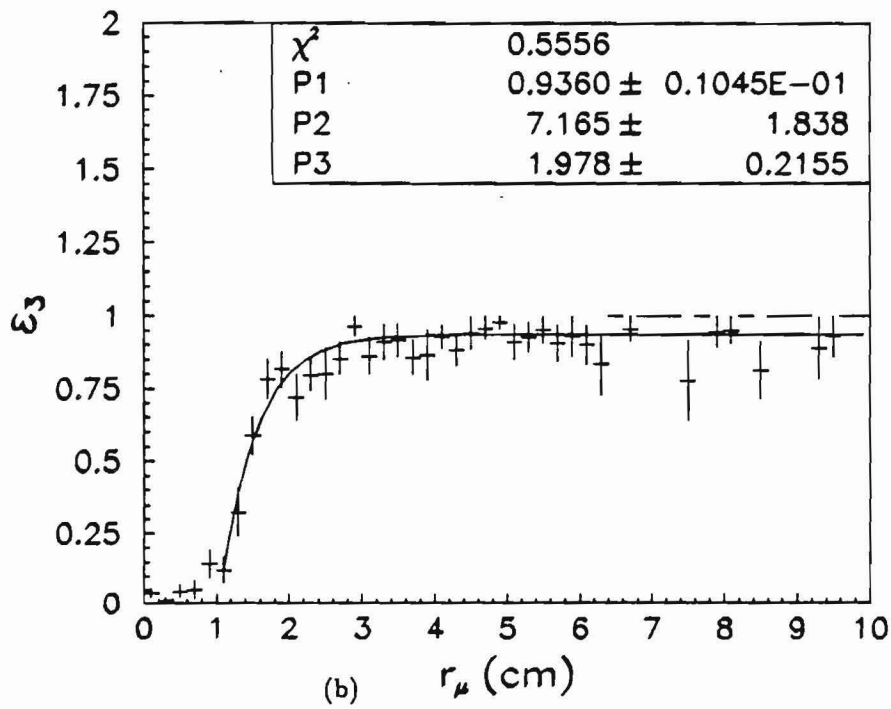


(b)

**Self-veto insensitivity as a function of $r_\mu$, for (a) hydrogen and (b) deuterium, when use is made of the SMS latches.**

**Fig. 3.26**

where $r_\mu$ is in *centimeters*. The resulting fit, along with the values of the fit parameters are shown in Fig. 3.26.

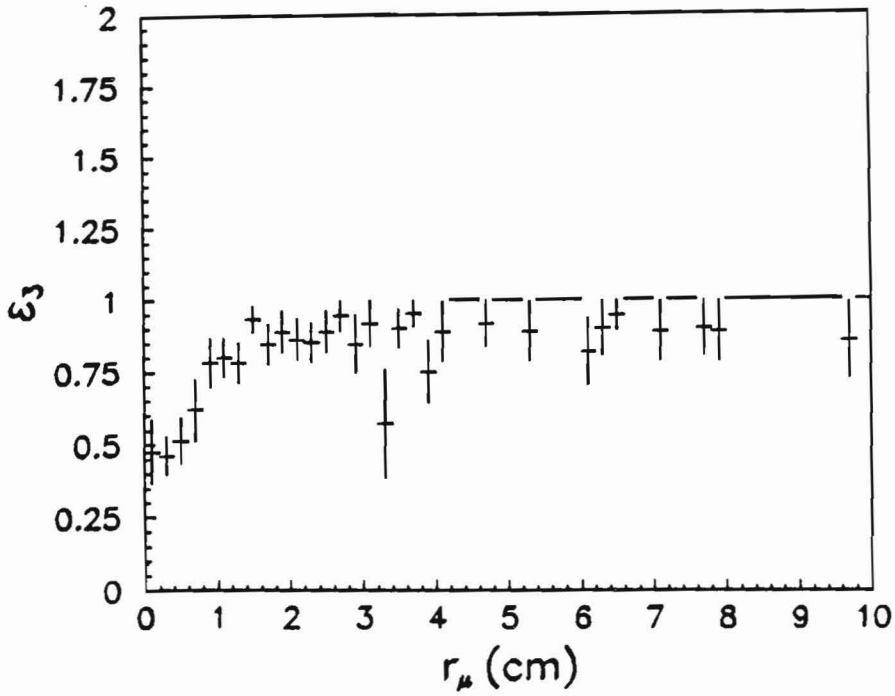


**Self-veto insensitivity as a function of $r_\mu$ as measured from quadrant one (deuterium).**

**Fig. 3.27**

**Table 3.4**

| | Cut 1 | Cut 2 | Cut 3 |
|---|---|---|---|
| $H_2$ | $0.961 \pm 0.003$ | $0.933 \pm 0.01$ | $0.958 \pm 0.014$ |
| $D_2$ | $0.952 \pm 0.005$ | $0.914 \pm 0.014$ | $0.905 \pm 0.025$ |

**The behaviour of $\varepsilon_3$ as a function of various cuts when SMS latches are used.**

**Table 3.5**

| | Plane 1 | Plane 2 |
|---|---|---|
| $H_2$ | $0.9926 \pm 0.0005$ | $0.9802 \pm 0.0009$ |
| $D_2$ | $0.9929 \pm 0.0008$ | $0.9803 \pm 0.001$ |

**Efficiency of SMS1 latches when the muon trajectory is constrained to traverse the third quadrant at SPM1.**

**Table 3.6**

| | Plane 1 | Plane 2 |
|---|---|---|
| $H_2$ | $0.966 \pm 0.0095$ | $0.980 \pm 0.0075$ |
| $D_2$ | $0.852 \pm 0.023$ | $0.850 \pm 0.023$ |

**Efficiency of SMS1 latches when the muon trajectory is constrained to traverse the first quadrant at SPM1.**

**Table 3.7**

| $x_{bj}$ | $H_2$ | $D_2$ |
|---|---|---|
| 0.005–0.028 | $0.923 \pm 0.037$ | $0.864 \pm 0.045$ |
| 0.028–0.050 | $0.975 \pm 0.025$ | $0.903 \pm 0.053$ |
| 0.050–0.080 | $0.925 \pm 0.042$ | $0.909 \pm 0.061$ |
| 0.080–0.160 | $1.000 \pm 0.000$ | $1.000 \pm 0.000$ |
| 0.160–1.000 | $1.000 \pm 0.000$ | $1.000 \pm 0.000$ |

**Trigger efficiency as a function of the $x_{bj}$ range, when use is made of the SMS latches. The errors are statistical errors only.**

A few comments are in order, regarding this result. Although we expected $\varepsilon_3$ to be nearly equal to one for large values of $r_\mu$, we see clearly from Fig. 3.26 that it does not. For hydrogen, the asymptotic value is 0.954 and for deuterium it is 0.936. If one assumes that for $r_\mu > 3\,\mathrm{cm}$ $\varepsilon_3$ is constant, than a merging of all the data points yields $0.961 \pm 0.003$ for hydrogen and $0.952 \pm 0.005$ for deuterium. But a complication arises when we apply more restrictive cuts to the SAT data sample. In Table 3.4, we present $\varepsilon_3$ for three different cuts denoted by Cut 1, Cut 2 and Cut 3. These cuts are defined as follows :

*Cut 1*

$$r_\mu > 3\,\mathrm{cm}$$

*Cut 2*

$$r_\mu > 3\,\mathrm{cm}$$

$$x_{bj} > 0.005$$

*Cut 3*

$$r_\mu > 3\,\mathrm{cm}$$

$$x_{bj} > 0.005$$

$$Q^2 > 4\,\mathrm{GeV}^2$$

$$\nu > 50\,\mathrm{GeV}$$

$$y < 0.65$$

$$-11.6\,\mathrm{m} < x_v < -10.6\,\mathrm{m}$$

Cut 3 defines our kinematical range.

A glance at Table 3.4 shows that we are faced with two problems. The first problem, mentioned earlier, is the fact that $\varepsilon_3$ is not equal to one when $r_\mu$ is large, coupled with the fact that it shows an $x_{bj}$ dependence Table 3.7. The second problem is the discrepancy between hydrogen and deuterium, for Cut 2 and Cut 3.

Concerning the second problem, a possible explanation would be that the latch efficiencies for quadrant 3 are different for hydrogen and deuterium. This hypothesis, however, can be dismissed by considering the latch efficiencies for quadrant 3 as shown in Table 3.5. There remains to consider the state of the first quadrant. Clearly, from Table 3.6, the overall efficiency of the latches in the first quadrant is very low for deuterium (0.85). Since inefficiencies stemming from the first quadrant can still contaminate the measurement we perform using the third quadrant, we are forced to not use the SMS latches in order to determine $\varepsilon_3$.

The only possibility left is to appeal to the LAT hardware trigger bit to decide whether a given event is a self-veto event. To argue that this is a valid approach, we recall, from earlier discussions, that the hardware and electronic efficiencies of the large-angle trigger in the upper half of the muon system are better than 0.99. Therefore, if the LAT hardware bit fails to be set, we can conclude that this is due to a self-veto in the SMS planes. Bearing this in mind,

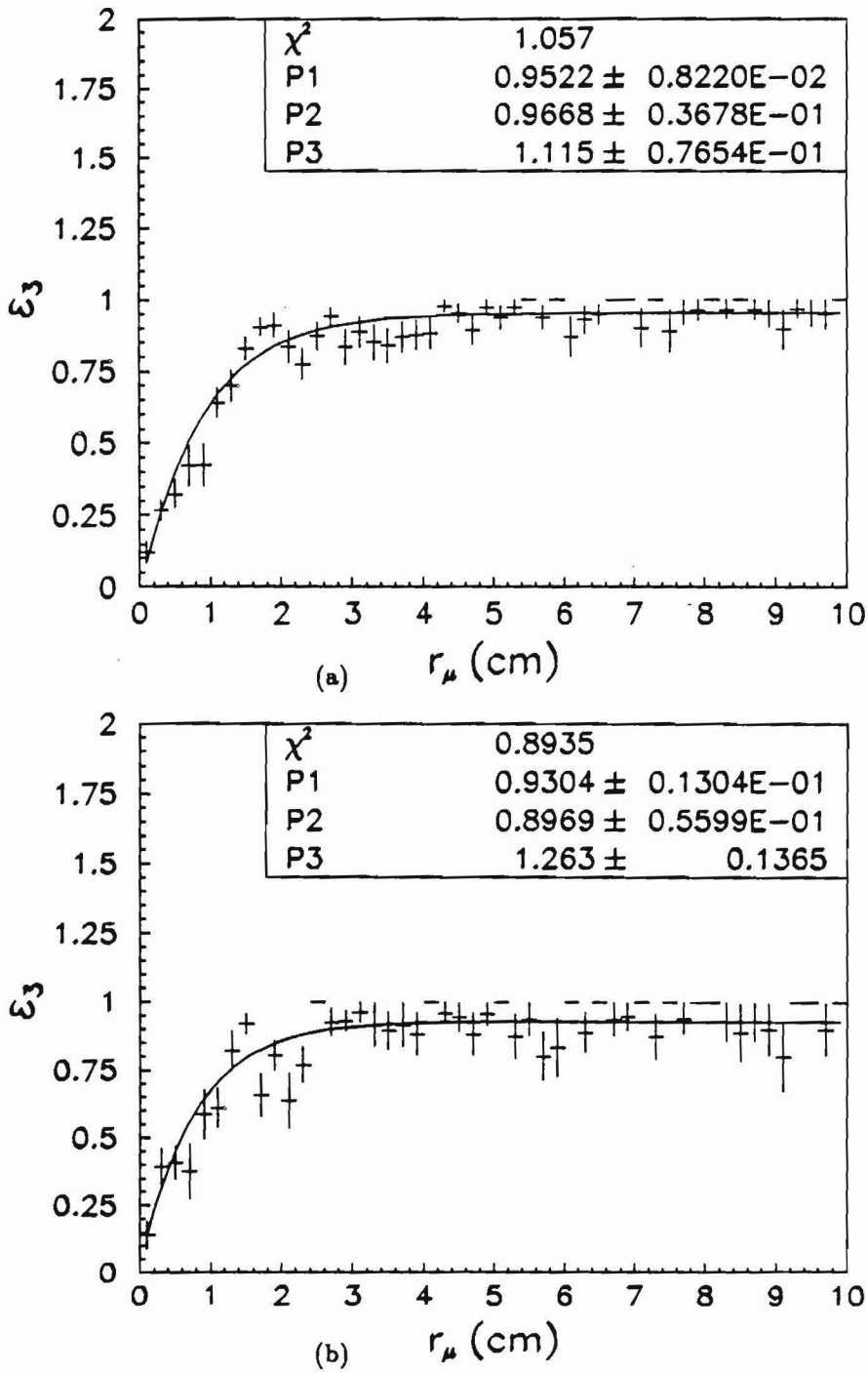


**Self-veto insensitivity as a function of $r_\mu$, for (a) hydrogen and (b) deuterium.**

**Fig. 3.28**

we present our final measurement of $\varepsilon_3$. We show in Fig. 3.28 $\varepsilon_3$ as a function of $r_\mu$. The parametrisation we use is that of Eq. 3.6. For $r_\mu < 3\,\mathrm{cm}$, $\varepsilon$ varies

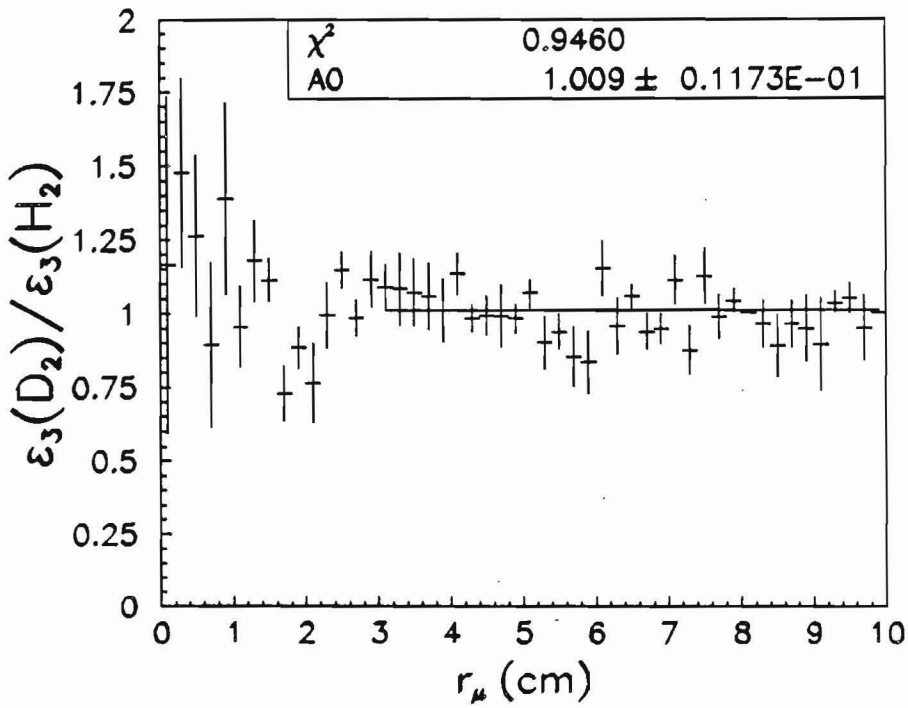


**Ratio of $\varepsilon_3$ for deuterium to $\varepsilon_3$ for hydrogen.**
**Fig. 3.29**

rapidly and does not reach 0 as $r_\mu$ approaches 0. The latter is a consequence of the finite resolution on $r_\mu$ (around 6 mm). It is then reasonably flat for $r_\mu > 3$ cm, which will be a justification for imposing on our final sample the cut $r_\mu > 3$ cm. We have however to admit that we do not understand the reason why the asymptotic value of $\varepsilon_3$ for large $r_\mu$ is not 1, contrary to our expectation. To cross-check the value of the parameter $P_1$, we have calculated the value of $\varepsilon_3$ assuming that it is constant for $r_\mu > 3$ cm. We have found $0.9565 \pm 0.004$ for hydrogen and $0.9489 \pm 0.006$ for deuterium. These values are higher than the values of $P_1$ found by fitting $\varepsilon_3$, which is understandable since the fitting procedure ignores bins in $r_\mu$ where the efficiency is equal to 1.

Using Cut 3, previously defined, we find that the average of $\varepsilon_3$ is $0.945 \pm 0.012$ for hydrogen and $0.952 \pm 0.013$ for deuterium.

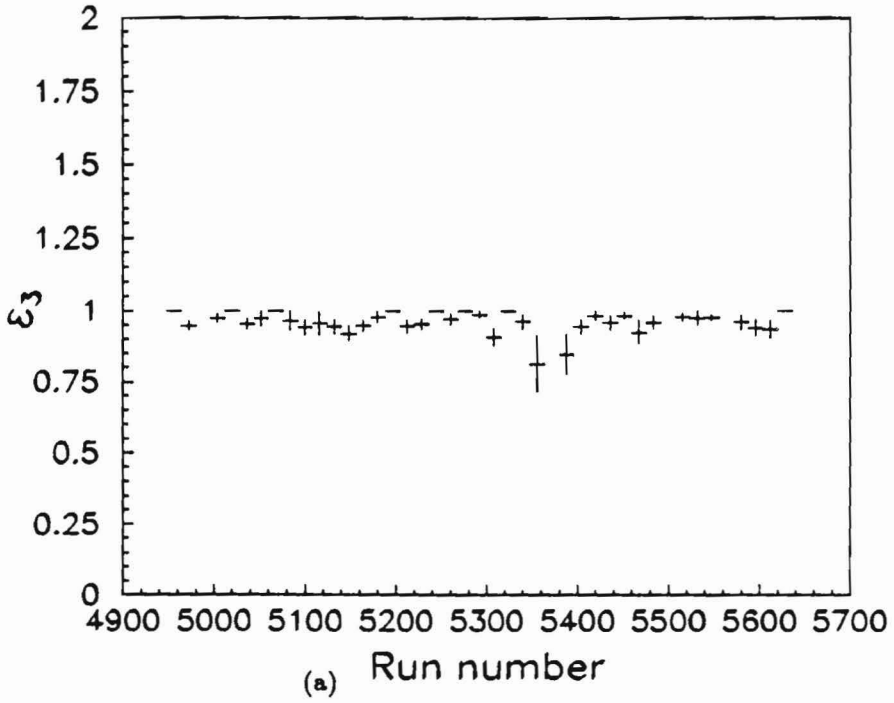


(a)

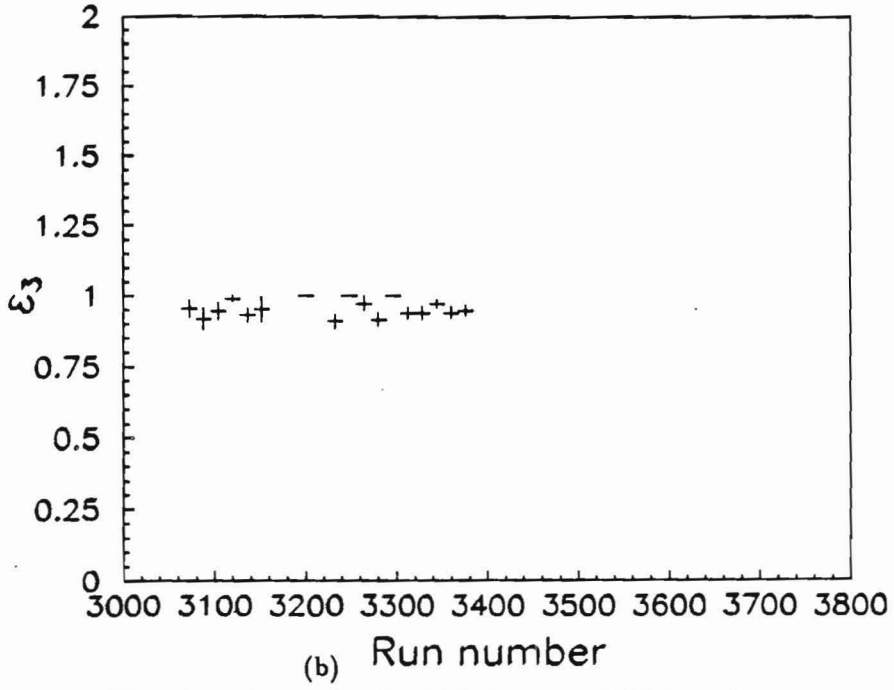


(b)

**Time dependence of $\varepsilon_3$ for (a) hydrogen and (b) deuterium.**

**Fig. 3.30**

As a last point related to the trigger efficiency, we wish to mention the time stability of $\varepsilon_3$. As will be discussed later, in our final sample, runs which show

an abnormal behaviour will be removed. With those runs removed, we have plotted the average of $\varepsilon_3$ as a function of run number in Fig. 3.30 for hydrogen and deuterium. It can be seen that a few hydrogen runs show a low average $\varepsilon_3$. Their removal has no significant impact of $\varepsilon_3$. Consequently, we shall keep them in our sample.

**Table 3.8**

| $x_{bj}$ | $H_2$ | $D_2$ |
|---|---|---|
| 0.005–0.028 | $0.930 \pm 0.022$ | $0.946 \pm 0.023$ |
| 0.028–0.050 | $0.931 \pm 0.030$ | $0.928 \pm 0.031$ |
| 0.050–0.080 | $0.985 \pm 0.015$ | $0.958 \pm 0.029$ |
| 0.080–0.160 | $0.938 \pm 0.030$ | $0.975 \pm 0.025$ |
| 0.160–1.000 | $0.964 \pm 0.035$ | $1.000 \pm 0.000$ |

**Final trigger efficiency as a function of the $x_{bj}$ range. The errors are statistical errors only.**

Now, given this we must decide on the strategy for correcting our data for the losses resulting from self-vetoing. If we are only concerned about the ratio of cross-sections, then we do not need to correct for the trigger efficiency. To support this statement, we consider Fig. 3.29 where we have plotted the ratio of deuterium to hydrogen $\varepsilon_3$. The parameter $A_0$ is a level fit to this ratio for $r_\mu > 3\,\mathrm{cm}$. It shows that both running periods have the same $\varepsilon_3$. If, however, we wish to measure the cross-sections, we may correct the data in two different ways. Since $\varepsilon_3$ is constant for $r_\mu > 3\,\mathrm{cm}$, we may apply an overall correction factor to all bins or we apply a bin to bin correction in $x_{bj}$ based on Table 3.8 and obtained with Cut 3 imposed on the SAT sample. But given that $\varepsilon_3$ does not show an $x_{bj}$ dependence (unlike the measurement obtained using the SMS latches), we may apply an overall correction factor for each target.

The systematic uncertainty on these corrections stems from our lack of understanding as to why $\varepsilon_3$ is not unity when $r_\mu$ is large. One way of estimating

the systematic uncertainty is to take as a correction factor for hydrogen

$$\frac{1}{2}(1+\frac{1}{0.9565})=1.023$$

which will give rise to a relative uncertainty of

$$\frac{\frac{1}{2}(\frac{1}{0.9565}-1)}{\frac{1}{2}(\frac{1}{0.9565}+1)}=0.02$$

if we consider that the measurement we performed is a lower bound of the trigger efficiency.

Similar considerations apply to deuterium, leading to a final correction factor of

$$\frac{1}{2}(1+\frac{1}{0.9489})=1.027$$

and a relative systematic uncertainty of

$$\frac{\frac{1}{2}(\frac{1}{0.9489}-1)}{\frac{1}{2}(\frac{1}{0.9489}+1)}=0.026$$

**Table 3.9**

| | Correction factor | Statistical error (in %) | Systematic error (in %) |
|---|---|---|---|
| $H_2$ | 1.023 | 0.4 | 2.0 |
| $D_2$ | 1.027 | 0.6 | 2.6 |

**Corrections to cross-sections arising from the inefficiency of large-angle trigger.**

In Table 3.9, we summarise our final corrections to cross-sections stemming from the inefficiency of the large-angle trigger.

## 3.5 Software Efficiency

### *3.5.1 Method*

As we mentioned earlier, we need to take into account the inefficiencies of the software that reconstruct the muon in the forward spectrometers.

The efficiency for reconstructing the muon is limited by the sensitivity of the alogirthms employed to the number of available hits in the chambers, which in turn is directly related to the efficiency of the chamber for registering hits.

The efficiency of the filter program will be estimated directly from data, with help from a monitoring filter.

The efficiency of the pattern recogniser will be estimated primarily using a Monte Carlo simulation, but we shall discuss some problems that arise when an attempt at an independent check based on data is made.

The efficiency of the muon matcher will be estimated from Monte Carlo simulation. However, our simulation does not include any muon large-angle scattering in the steel, and as it so happens that such a process impairs significantly the efficiency of the muon matcher. This contribution will be extracted from data.

The efficiency of the vertex processor will be measured from data. But as it turns out, its performance is very good, provided that the tracks that are handed over to this software are good-quality tracks. In other words, given that the pattern recogniser and the track-fitting program reconstruct tracks correctly, the vertex processor does not fail to reconstruct the primary vertex correctly.

### *3.5.2 Filter efficiency*

The question that needs to be addressed is whether the filter,as described earlier, rejects events which are genuine deep-inelastic events. That it does not

reject all unwanted events is unimportant. But it should always accept events in which an interaction occurred, or at worst, it should reject only a negligible fraction of such events. In order to estimate its efficiency, a monitoring filtering programme was run concurrently with the main filter. Randomly, on 50% of the input events, the monitoring program checks the presence of a scattered muon in the PTM chambers. Events are flagged as to whether they pass or fail this monitoring filter and output on tape even if they have been rejected by the primary filter. The measurement method of the efficiency of the primary filter is conceptually identical to that used to measure the efficiency of the trigger. We took a set of LAT reconstructed events which passed the monitoring filter and applied our final cuts to generate a set of "genuine" deeply inelastic scattering events. We found that the fraction of events which actually failed to be accepted by the primary filter is $0.0059 \pm 0.0026$. This result is consistent with one that was obtained from a visual scan of LAT events and reported in (Schmitt,Aïd, 1991b). Based on this measurement, we can conclude that the losses due to the filter program are negligible. Henceforth, we shall ignore those and simply take

$$\varepsilon_f \sim 1$$

### *3.5.3 Pattern-recognition efficiency*

The limitations of the pattern-recognition program in reconstructing the scattered muon stems partly from its sensitivity to the inefficiency of the tracking chambers. The behaviour and shortcomings of the pattern-recogniser have been discussed at some length in (Ryan, 1990). The efficiency of pattern recognition has been estimated using the Monte Carlo simulation program in which the efficiencies of the tracking chambers have been incorporated.

In principle, the reconstruction efficiency depends on several variables such as the coordinates of its trajectory at each chamber station, the number of charged tracks (a high number of charged tracks will tend to confuse the pattern recognition program). Even if these were the only fundamental variables on which the reconstruction efficiency depended, it is not possible in practice

to determine its joint dependence on all these variables. In the end, our strategy will be to express the reconstruction efficiency $\varepsilon_r$ as a function of each kinematical variable of interest, namely $Q^2$, $\nu$ and $x_{bj}$. Averaging over the other variables will be assumed, which is legitimate, since, as we pointed out earlier, there is a fair agreement between the reconstructed Monte Carlo quantities and their partners in data. In order to keep the systematic uncertainty small, we shall impose cuts that will guarantee a reconstruction efficiency of at least 90%.

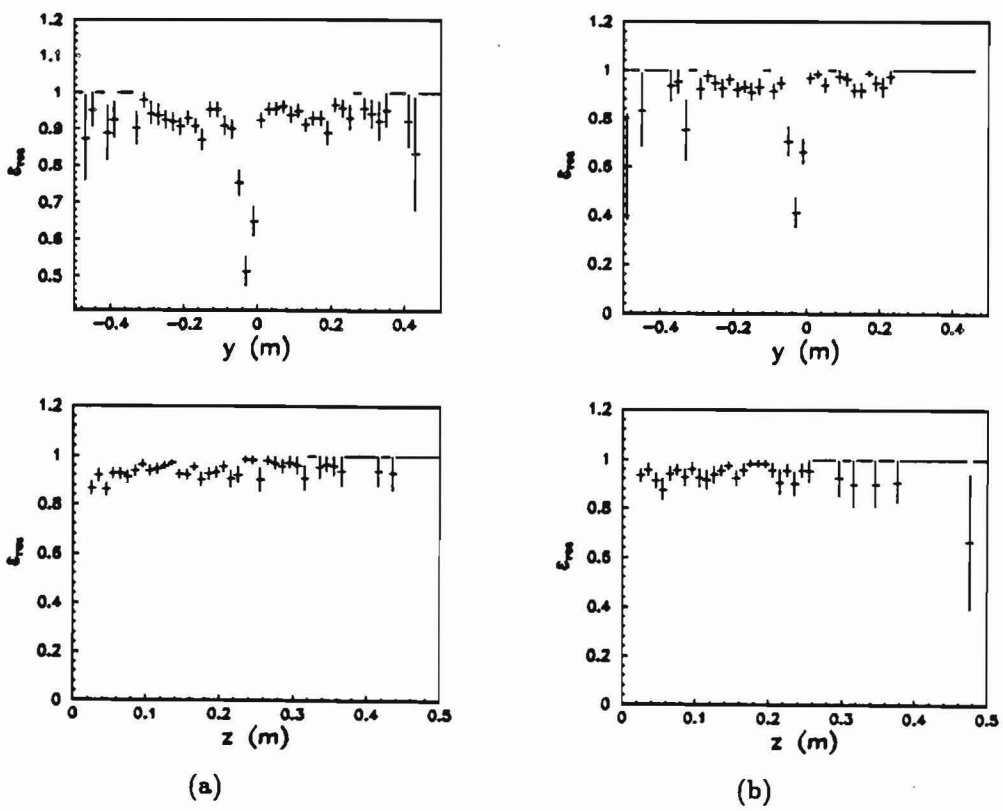


Reconstruction efficiency as a function of the coordinates of the impact point of the muon at SMP1 for (a) hydrogen and (b) deuterium.

**Fig. 3.31**

It is intuitively clear that the reconstruction efficiency of the outgoing muon will depend primarily on the intercept of its trajectory at each chamber station. Regions of low chamber efficiency will be responsible for missing hits,

resulting in the potential loss of the scattered muon. Following this idea, we have plotted $\varepsilon_\tau$ as a function of $y_\mu$ and $z_\mu$, the generated coordinates of the scattered muon at SPM1. As a function of $y_\mu$, it drops down to nearly 50% in the region $-0.06\,m < y_\mu < 0\,m$. The source of this low value is the vertical inactive stripe (divider) of the drift chambers. We shall impose an additional cut

$$y_\mu < -0.08\,\mathrm{m} \text{ or } y_\mu > 0.02\,\mathrm{m}$$

The reason for removing a slightly larger region stems from the resolution in $y_\mu$. Although we have plotted the efficiency as a function of the generated coordinate $y_\mu$, we will have at our disposal, in data, only the reconstructed coordinate.

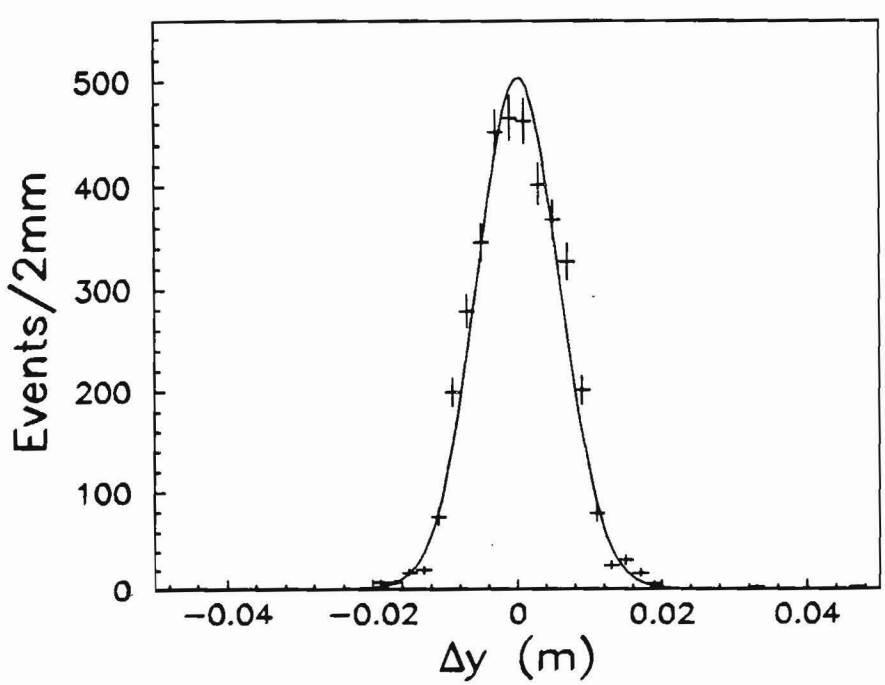


Resolution $\Delta y$ on the $y_\mu$ coordinate of the muon impact point at the first SPM station. The width of the distribution is approximately 6 mm.

**Fig. 3.32**

The resolution in $y_\mu$, as estimated from Monte Carlo is around 6 mm, as can be seen in Fig. 3.32. A safety margin of about $3\sigma$ gives the aforementioned cut.

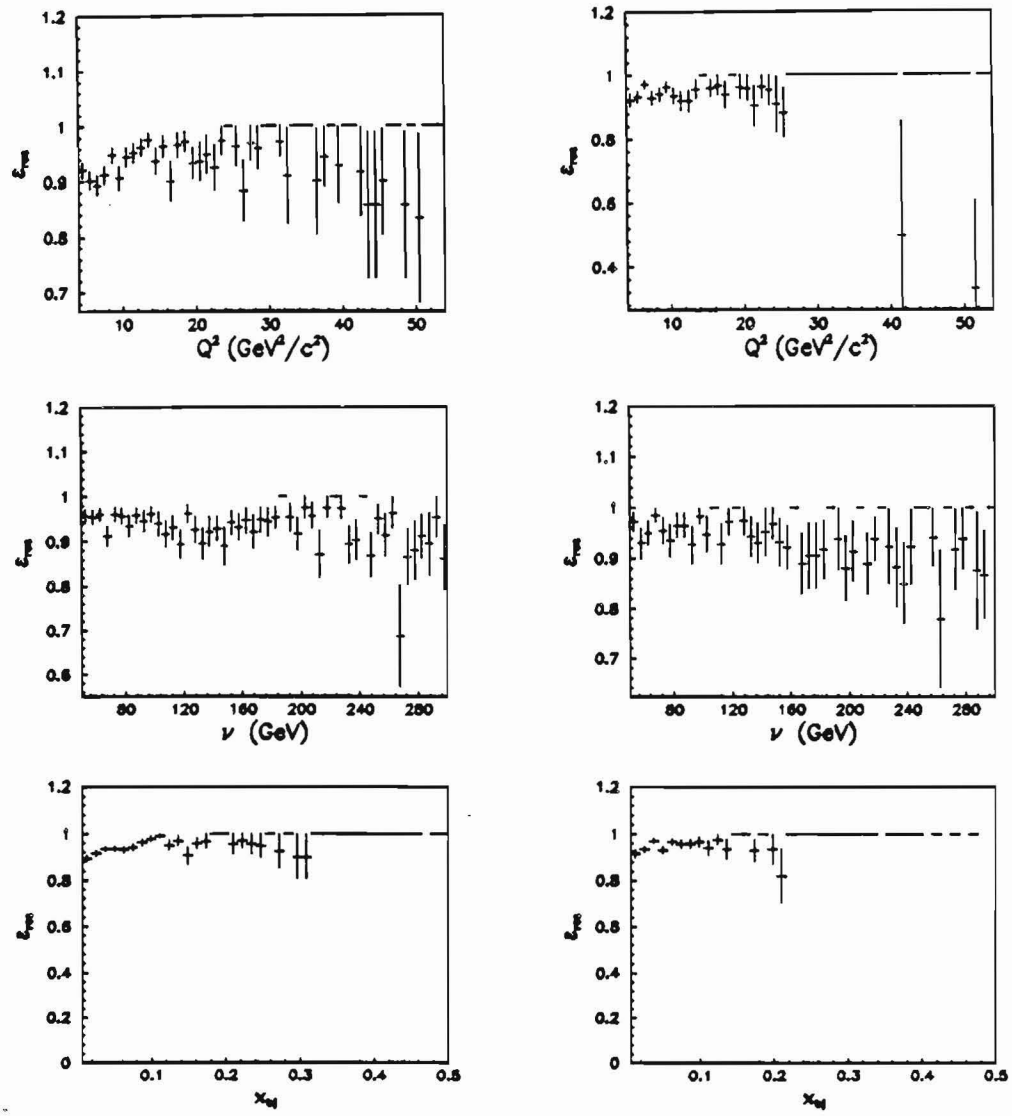


**Reconstruction efficiency as a function of kinematical variables for (a) hydrogen and (b) deuterium.**
**Fig. 3.33**

The dependence on $z_\mu$ is mild and does not show any striking feature. We

are plotting the reconstruction efficiency only for $z_\mu > 0.02\,\mathrm{m}$, since, as we said earlier, the lower half of the spectrometer had to be excluded because of trigger iniefficiency.

Now with the aforementioned cut in effect, we have plotted the dependence of the reconstruction efficiency on the kinematical variables $Q^2$, $\nu$ and $x_{bj}$ (Fig. 3.33). The average value of the reconstruction efficiency outside the central vertical stripe is 0.933±0.004 for hydrogen and 0.947±0.006 for deuterium.

### *3.5.4 Muon-matching efficiency*

The efficiency of the muon-matching code has been estimated from data. The method and results can be found in (Schmitt,Aïd 1991b). A sample of events were selected by demanding first that there be one and only one beam, that it be in-time and fitted. Next, in order to guarantee that the events are genuine deeply inelastic scattering events, it is required that there be at least two tracks in the forward spectrometer. Furthermore, since the muon-matching program needs a track reaching the drift chambers, it is demanded that there be a positive track with a momentum above 1 GeV reaching the drift chambers. These requirements define an initial sample of events in which the muon should have been identified. A subset of events which failed to have a muon identified has been scanned visually in order to verify that they were genuine match failures. The majority of the events could not be matched because of errors of the pattern recognition code in the forward spectrometer. The conclusion from this visual scan is that the the muon-matching inefficiency is

$$1 - \varepsilon_m = 1.9 \pm 0.7\%.$$

In all events that failed the match, the muon had undergone a large-angle

scattering in the steel and had not passed the intersection match, presumably because the cuts used by the algorithm were not adequate. It should be noted that the simulation program does not include any large-angle scattering in either the calorimeter lead or the steel absorber.

### *3.5.5 Vertex-reconstruction efficiency*

The vertex-reconstruction efficiency has been estimated from visual scan of LAT data. It was found that the inefficiency is negligible ($< 1\%$). For more details, see (Schmitt, Aïd, 1991b).

### *3.5.6 Other issues in reconstruction efficiency*

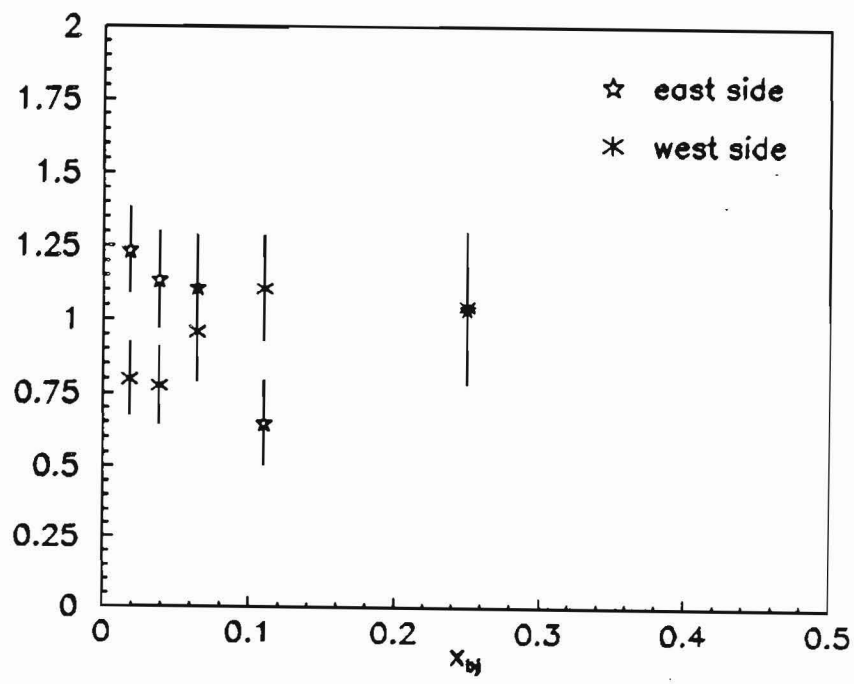


Neutron to proton cross-section ratio for each side of the spectrometer.
**Fig. 3.34**

In order to check the results obtained from Monte Carlo concerning the

muon reconstruction efficiency, measurements have been performed from LAT data (Schmitt,1991a). This is made possible by the fact that the muon lines are reconstructed independently with the PTM planes on the one hand and with the chambers located upstream of the iron absorber. As we mentioned earlier, most of the failures to reconstruct the muon have their origin in pattern recognition problems upstream of the aborber.

These studies reveal two problems. Firstly, there appear to be a difference in reconstruction efficiency between the east and the west sides of the drift chambers, which may be due to plane-inefficiency correlations. This correlation is not included in the Monte Carlo. Secondly, even far away from the region where correlated inefficiency are important, there is a discrepancy between the Monte Carlo simulation and the aforementioned measurement of the order of 5%. We shall take this discrepancy as an overall systematic uncertainty that needs to be applied to all the bins where we measure the cross-sections.

In order to assess the effect of such a difference, we have measured the the neutron-to proton cross-section by considering each wing separately (Fig. 3.34). If such an effect exists it cannot be inferred from these plots, the variations between each and west being consistent with statistical fluctuations, but it cannot be ruled out either.

### *3.5.7 Corrections and systematic uncertainties*

From the previous discussions, we are now in position to determine the corrections arising from reconstruction inefficiencies that we need to apply in order to get the deep inelastic cross-sections.

All effects which are modelled by the Monte Carlo will lead to a bin by

**Table 3.10**

| $x_{bj}$ | $H_2$ | $D_2$ |
|---|---|---|
| 0.005–0.028 | $0.8919 \pm 0.010$ | $0.9236 \pm 0.009$ |
| 0.028–0.050 | $0.9354 \pm 0.009$ | $0.9467 \pm 0.008$ |
| 0.050–0.080 | $0.9326 \pm 0.010$ | $0.9557 \pm 0.008$ |
| 0.080–0.160 | $0.9638 \pm 0.007$ | $0.9612 \pm 0.007$ |
| 0.160–1.000 | $0.9718 \pm 0.009$ | $0.9688 \pm 0.009$ |

Reconstruction efficiency as a function of the $x_{bj}$ range. The errors are statistical errors only.

bin correction in $x_{bj}$ based on the reconstruction efficiency given in Table 3.10. Since, as we said earlier, there is some discrepancy between the Monte Carlo estimate and the data estimate of the reconstruction efficiency of the order of 5%, we shall take this as an overall systematic uncertainty on the corrections we need to apply.

In addition to these correction factors, we need to apply a correction which arises from the component of the muon-matching inefficiency which has not been taken into account in the simulation program. To this correction, we shall attribute a statistical error only but no systematic error.

## 3.6 Issues in spectrometer calibration

Momentum measurement in E665 is accomplished by two spectromters : the beam spectrometer and the forward spectrometer. A sample of non-interacing beams, such as those provided by the RBEAM trigger, permits the cross-calibration of the both spectrometers. Momentum measurements for such events should provide identical results. Studies done elsewhere (Schmitt,1991f) reveal that the momentum measured by the beam spectrometer is around 7 GeV higher than that reported in the forward spectrometer. There is some evidence that the beam spectrometer is at fault, and under the assumption that the beam energy is really lower than actually measured by the beam spectrometer, we wish to assess the impact of such an effect on the cross-sections and on the ratio of these cross-sections.

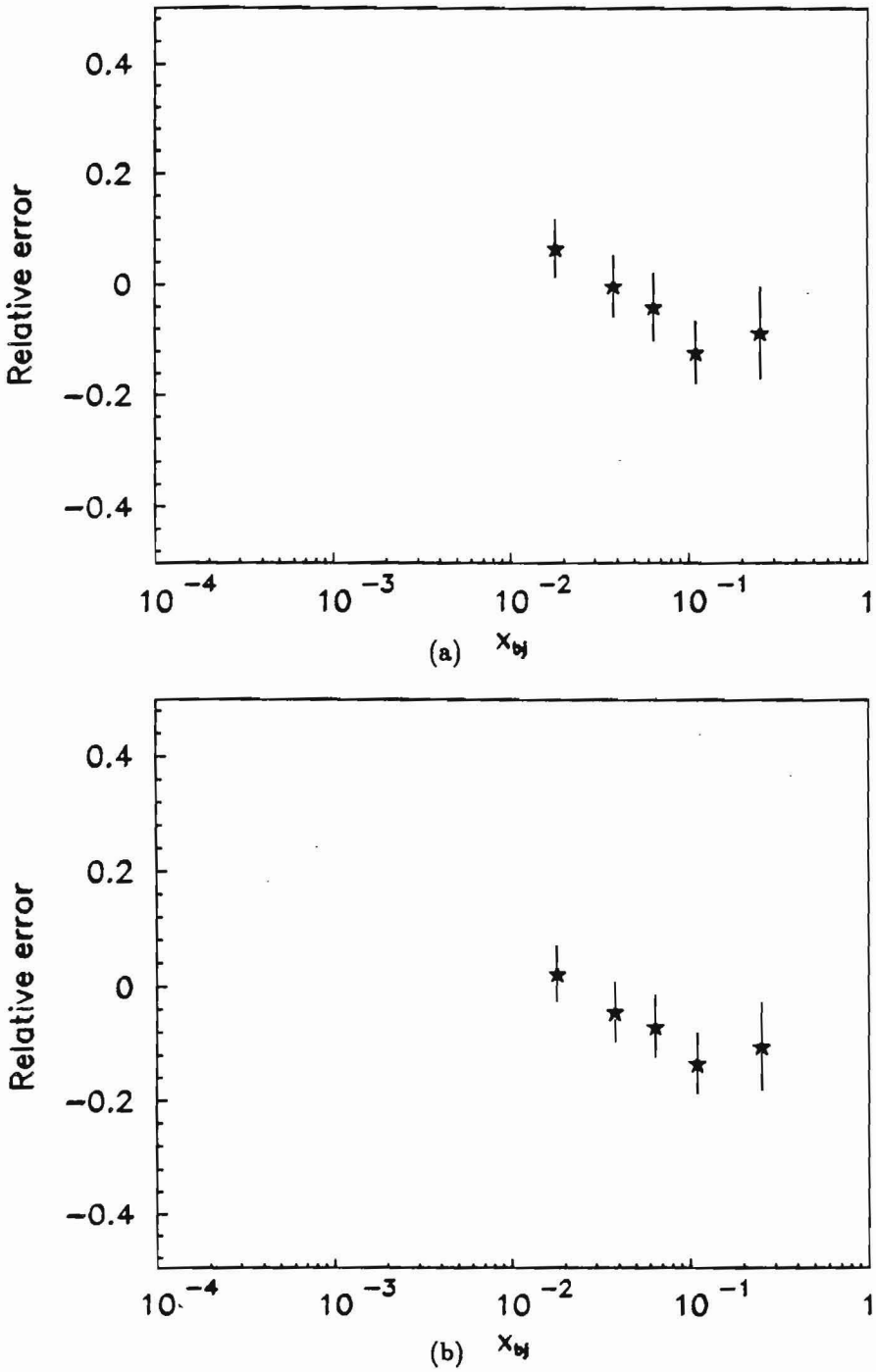


**Relative error on the cross-section, originating from a mis-measurement of the beam energy for (a) hydrogen and (b) deuterium.**

**Fig. 3.35**

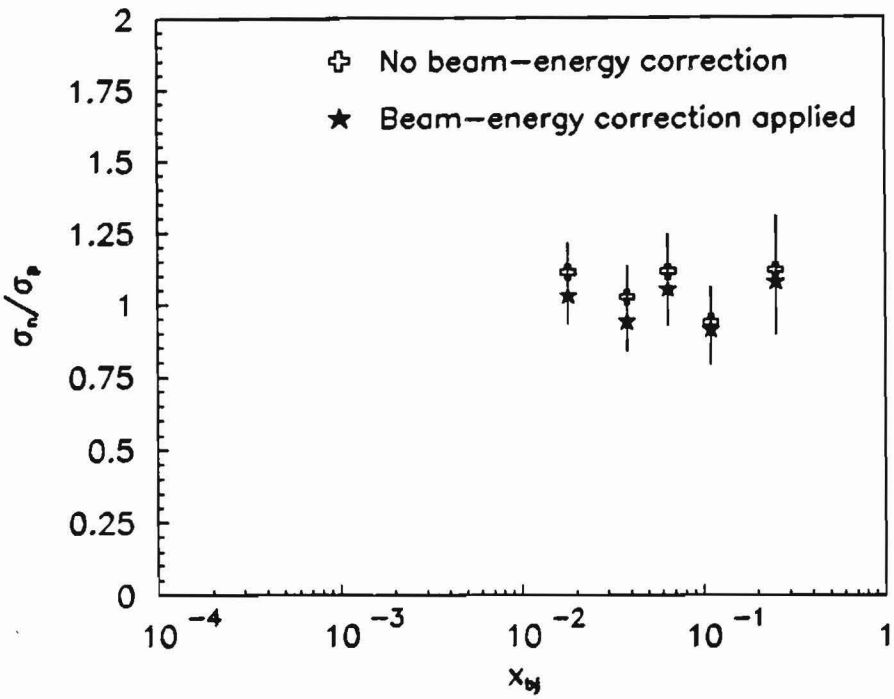


**Cross-section ratios, with and without beam energy re-adjusted.**
**Fig. 3.36**

In Fig. 3.35, we have plotted the relative error

$$\frac{\sigma_1 - \sigma_0}{\sigma_1}$$

where $\sigma_1$ is the cross-section when the beam energy is decreased by 7 GeV and $\sigma_0$ the same cross-section when no such effect is taken into account. Overall, correcting for such an effect leads us to loose about 200 events and results in decreasing the cross-section by as much as 10% in the worst case and 5% in the best case. The ratio is not so sensitive to an energy mis-measurement, as can be seen in Fig. 3.36. The variations are well within the statistical uncertainty.

### 3.7 Issues in kinematical resolution

The finite resolution of the spectrometer will induce a smearing of the kinematical variables. Our purpose in this section is to argue that, provided

that the resolution is not too large, in a sense that we shall make more precise later, the correction due to the smearing of $x_{bj}$ and $Q^2$ is negligible. This will imply in particular that the fact that the amount of multiple scattering has been implemented incorrectly in the Monte Carlo simulation is of no serious consequence. As a consequence of which, we shall dispense with actually correcting for this effect.

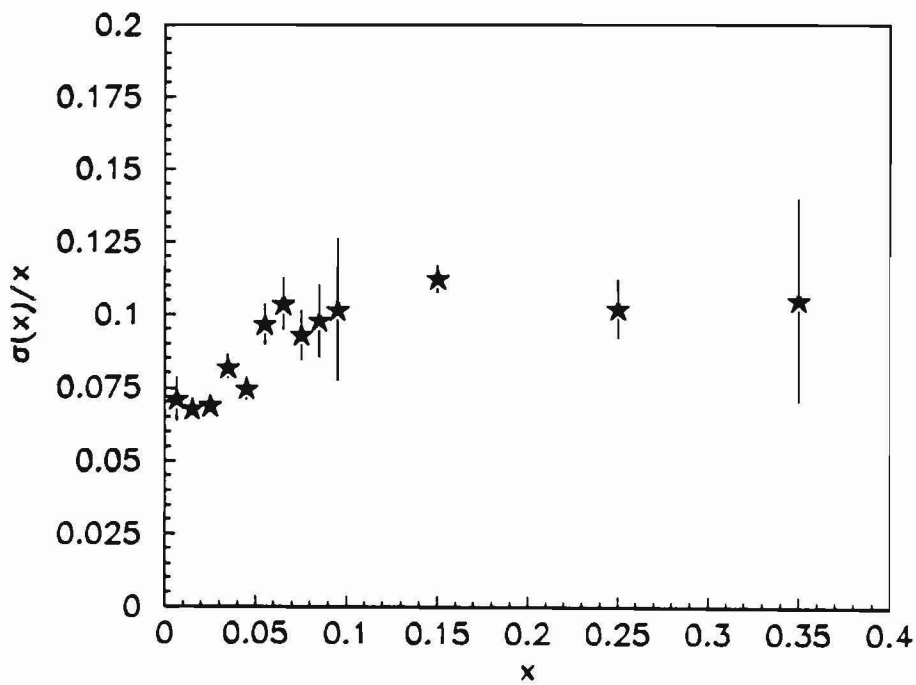


$x_{bj}$ resolution as estimated from Monte Carlo.
**Fig. 3.37**

Consider a probability density function $f(x)$. This is the true distribution of the variable $x$. The distribution we observe is $g(x)$. Let us assume that the resolution kernel $k(x,y)$ giving rise to $g(x)$ is gaussian, of the form

$$k(x,y) = \frac{1}{\sqrt{2\pi}\sigma(x)} e^{-\frac{(x-y)^2}{2\sigma^2(x)}}$$

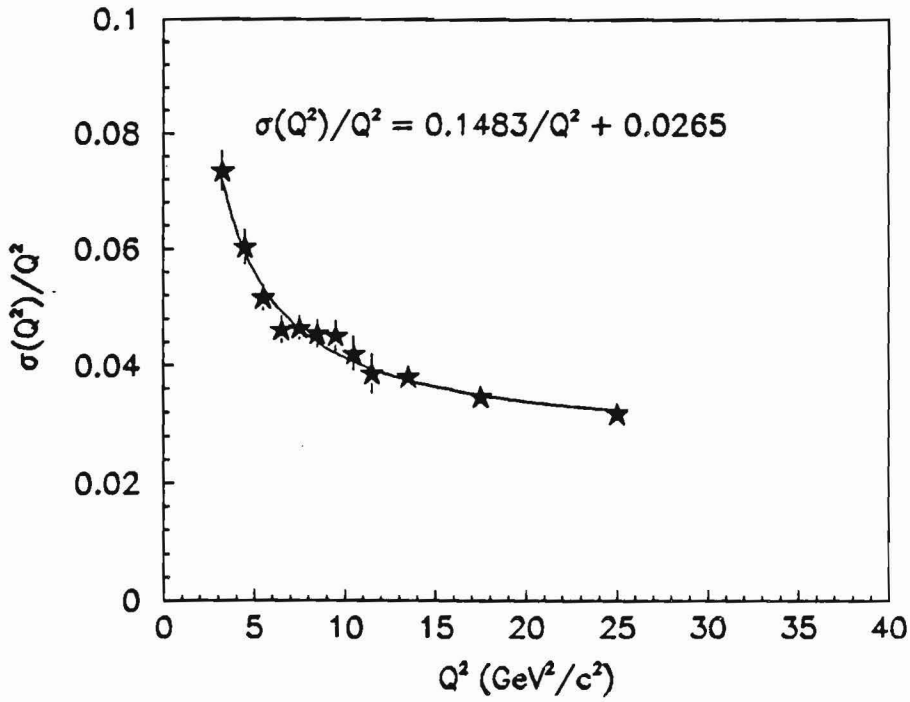


$Q^2$ resolution as estimated from Monte Carlo.
**Fig. 3.38**

The relation between $f$ and $g$ is given by

$$g(y) = \int_{-\infty}^{+\infty} \frac{1}{\sqrt{2\pi}\sigma(x)} e^{-\frac{(x-y)^2}{2\sigma^2(x)}} f(x)\, dx \tag{3.7}$$

In practice, even knowing $g$, it is difficult to invert Eq. 3.7 to get $f$. Eq. 3.7 is a special case of a more general class of integral equations. It is not our goal here to present the methods used to solve integral equations. For this, we refer the reader to Green (1969), Hoschtadt (1973), Mikhlin (1957), Muskelishvili (1953) and Pogozelski (1966). Here we shall derive an asymptotic expansion of $g$ as a function of $\sigma$, as $\sigma \to 0$. For this purpose, we write Eq. 3.7 as

$$g(y) = \int_{-\infty}^{+\infty} \frac{1}{\sqrt{2\pi}\sigma(x+y)} e^{-\frac{x^2}{2\sigma^2(x+y)}} f(x+y)\, dx$$

Futhermore, we shall set

$$\sigma = \frac{\theta}{\sqrt{t}}$$

In principle, the integration limits in Eq. 3.7 should be taken to be the boundaries of the domain of $f$. We shall assume that the resolution is small enough to justify the limits used in Eq. 3.7. However, this hypothesis breaks down at the edges of the domain of $f$. The result we shall derive will be valid only sufficiently far away from the boundaries of the interval of $f$.

We shall expand Eq. 3.7 in powers of $1/\sqrt{t}$ when $t \to \infty$. Following De Bruijn (De Bruijn, 1958), we apply the Laplace method to get an asymptotic expansion of $g(y)$. We have

$$g(y) \sim \sqrt{\frac{t}{2\pi}} \sum_{\nu=0}^{\infty} d_\nu t^{-\frac{1}{2}-\nu} \qquad (t \to \infty) \tag{3.8}$$

where

$$d_\nu = (-a_2)^{-\nu-\frac{1}{2}} \sum_{m=0}^{2\nu} c_{m,2\nu-m} (-a_2)^{-m} \Gamma\left(m+\nu+\frac{1}{2}\right)$$

The coefficients $c_{mn}$ are given by the double expansion

$$\frac{f(x+y)}{\sigma(x+y)} e^{tx^3} (a_3 + a_4 x + \ldots) = \sum_{m=0}^{\infty} \sum_{n=0}^{\infty} c_{mn} \left(tx^3\right)^m x^n$$

and

$$-\frac{1}{2\theta^2(x+y)} = a_2 + a_3 x + a_4 x^2 + \ldots$$

Performing all the expansions and keeping terms up to $\nu = 1$ in Eq. 3.8 we get the final result

$$g(y) \sim \left\{1 + \sigma'^2(y) + \sigma(y)\sigma''(y)\right\} f(y) + 2\sigma(y)\sigma'(y) f'(y) + \frac{\sigma^2}{2} f''(y) \tag{3.9}$$

When we apply the result of Eq. 3.9 in the case where

$$f(y) = \frac{a}{y^\alpha}$$

$$\sigma(y) = \lambda y$$

we get

$$\frac{g(y)}{f(y)} \sim 1 + \frac{\lambda^2}{2}(\alpha - 1)(\alpha - 2)$$

It is to be noted that the correction due to smearing is second order in $\lambda$, with the exception of $\alpha = 1$ or $\alpha = 2$; in the latter cases, the smearing correction is of order 4 in relative resolution.

We have checked our asympotic expansion with a simple Monte Carlo simulation, and we found that the expression we derived agrees very well with the simulation, except at the boundaries of the distributions as we expect. For the $Q^2$ distribution, the effect is below 1%, except at the boundaries of the domain. A similar procedure can be applied to the $x_{bj}$ distribution to show that the effect of resolution is negligible. For all purposes, it was found that the ratio of two smeared distributions is nearly equal to the ratio of the true distributions.

### 3.8 Background estimate

In addition to deeply inelastic events, the trigger will register unwanted background events. These are primarily muon-electron elastic scattering events ($\mu$-e), muon-bremsstrahlung events ($\mu$-$\gamma$), events which are accompanied by an out-of-time muon beam or originate from the interaction of a beam hadron (e.g. $\pi^+$) and finally events which result from the interaction of the muon outside of the target.

$\mu$-e scattering events, being elastic, obey

$$\frac{Q^2}{2m_e\nu} = 1$$

where $m_e$ is the electron mass. Since we calculate $x_{bj}$ using the proton mass, these events have

$$x_{bj} = \frac{m_e}{M_p} \sim 5.4 \times 10^{-4}$$

Since the minimum $x_{bj}$ we allow in our analysis is $5 \times 10^{-3}$, the contamination from such a physical process is negligible.

Muon-bremsstrahlung events are typically characterised by a very small muon scattering angle and a very high energy transfer, and will therefore appear at low $x_{bj}$. Since the target is inside the CVM, the scattered muon will not experience the full focusing of the spectrometer, as a result of which its orbit will bring it predominantly to the west side of the muon system. In our analysis, we have reduced the contribution from $\mu$-$\gamma$ events by first imposing a minimum $x_{bj}$ of $3 \times 10^{-3}$ and then a maximum $y$ of 0.65. The remaining radiative contribution will be corrected numerically and will be the subject of a subsequent section.

"Fake" events which are accompanied by an out-of-time beam are discarded by masking the beam muon trajectory with the beam hodoscopes. We always require that there be exactly one beam in the beam spectrometer and that it be in-time.

There remain events for which the interaction point is outside the volume of the liquid target. Those events which are far away (with regard to the vertex resolution) from the liquid target are easily removed by imposing a cut on the vertex position. This apply to events which occurred in PBT4, in PCV, in C0 and in C1. But such a vertex cut, because of resolution, will not remove

all the events for which the interaction point is in the target-vessel wall. To estimate the contamination from the target-vessel wall, we have taken data with an empty target

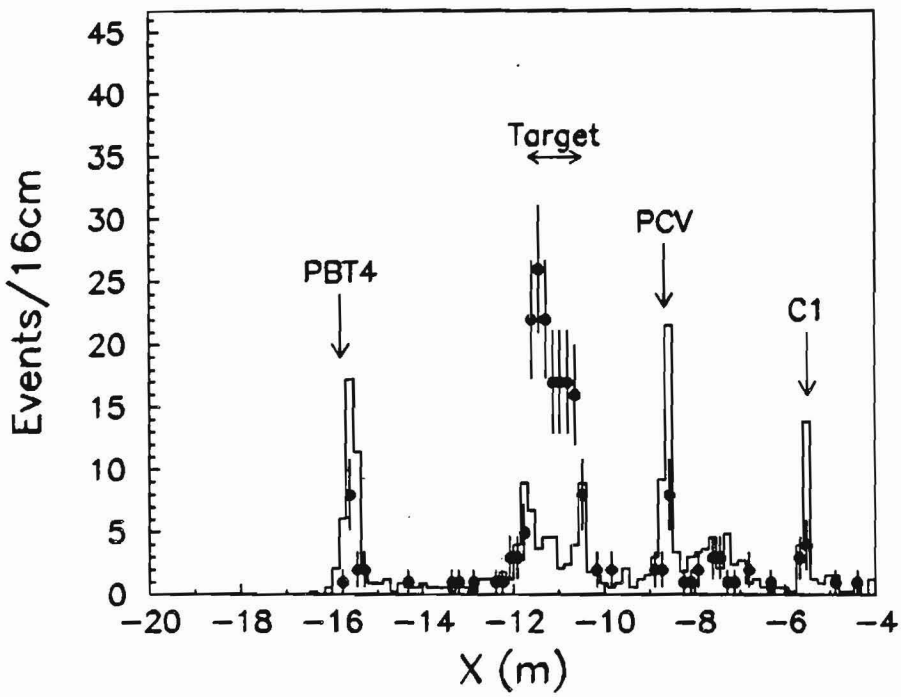


Distribution of primary vertices along the x-axis for empty target (solid line) and full target (solid circles). The vertical arrows show the detectors with materials which act as scatterers. The edges of the target can be clearly seen .

**Fig. 3.39**

Fig. 3.39 displays the distribution of vertices along the x-axis both for the empty target and the full hydrogen target. Only a fraction of the total hydrogen sample was used to generate this distribution. In order to have reasonably well reconstructed primary vertices, we have required that there be one in-time beam, no out-of-time beam, that the beam traverse the target, that $Q^2$ be greater than $4\,\mathrm{GeV}^2/c^2$ and $\nu$ be greater than 50 GeV. No other cuts have been applied. It can be seen in Fig. 3.39 that the distribution of events in the

target is substantially different between the full vessel and the empty vessel, the latter providing interactions in its end faces. Interactions in other materials of the spectrometer, such as PBT4, PCV, C0 and C1 are clearly present in both data sets. From this, it is natural to impose a cut on the x-position of the primary vertex to remove the latter category of events.

Let us estimate the fraction $\varepsilon_w$ of events which occur in the target wall. Let $N_f$ be the number of events which have been registered with a full target, with a number of beams $b_f$ and $N_e$ the number of events which have been registered with an empty target, with a number of beams $b_e$. Then we can write

$$N_f = N_l + N_w$$

where $N_l$ is the number of events which occurred in the liquid target and $N_w$ the number of events which occurred in the target-vessel wall. But

$$N_w = \frac{b_f}{b_e} N_e$$

and therefore

$$N_l = N_f(1 - \varepsilon_w)$$

with

$$\varepsilon_w = \frac{\frac{N_e}{b_e}}{\frac{N_f}{b_f}}$$

From this, it follows that a statistical uncertainty arising from the empty-target subtraction is to be added in quadrature to the statistical uncertainty arising from the full-target measurement. It is readily seen that the variance $\sigma^2$ on $N_l/b_f$ is

$$\sigma^2 = \frac{1}{b_f}\frac{N_l}{b_f} + \frac{1}{b_e}\frac{N_e}{b_e}$$

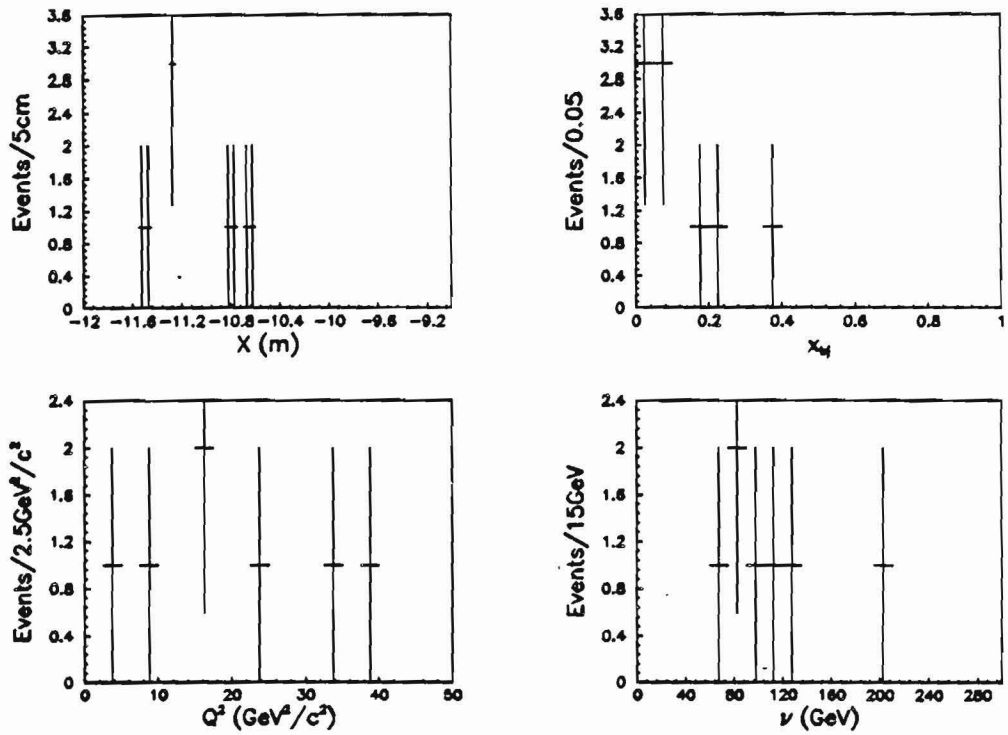


**Distribution of primary vertices along the x-axis for empty target for those events surviving all cuts, along with their kinematical distributions.**

**Fig. 3.40**

When we apply all the relevant cuts, we find that 9 events come from outside the fiducial volume of the liquid of target, for a total uncorrected number of beams of $1.140 \times 10^{10}$. The distribution of these background events is shown in Fig. 3.40. Ideally, we would like this correction to be performed on each bin of the the relevant kinematical distribution. But because of low statistics, we shall simply perform a level correction, identical in all bins. Such a correction is 2.8% for hydrogen and 1.2% for deuterium.

## 3.9 Deuterium-target purity

As we pointed out in Chapter 2, the deuterium target that was used during the 1987 run contains a small fraction of contaminants, the most important

one being HD, which as we said, represents 5.1% in volume of the target.

Let us determine the cross-section $\sigma_p$ and $\sigma_n$ for proton and neutron respectively. Let $p_i$ be the number of protons in the molecule of contaminant $i$, and similarly, $n_i$ be the number of neutrons in that molecule. We denote $\rho_i$ the density of contaminant $i$, $M_i$ its molar mass.

If $N_p$ is the number of proton interactions and $N_n$ the number of neutron interactions, then we can write

$$N_p = \sigma_p l \mathcal{N} \sum_i p_i \frac{\rho_i}{M_i}$$

$$N_n = \sigma_n l \mathcal{N} \sum_i n_i \frac{\rho_i}{M_i}$$

where N is the Avogadro number and $l$ the length of the target.

We take the density of HD to be the average of the hydrogen and deuterium density, and likewise the density of tritium to be 3/2 the density of deuterium.

If we denote by

$$\alpha = \sum_i p_i \frac{\rho_i}{M_i}$$

$$\beta = \sum_i n_i \frac{\rho_i}{M_i}$$

we find that

$$\alpha = 0.08046\,\mathrm{cm}^{-3}$$

$$\beta = 0.07843\,\mathrm{cm}^{-3}$$

If the number of events in the deuterium target is $N$, and the number of

beams is $B_D$ then

$$\sigma_n = \frac{1}{\beta}\frac{N}{lNB_D} - \frac{\alpha}{\beta}\sigma_p$$

With respect to a pure deuterium cross-section, the size of the correction we need to apply to the contaminated cross-section is of the order of 2.3%.

## 3.10 Data stability

The issue we want to address here is the time dependence of the running conditions of the experiment. This is a priori a problem since the time elapsed between the deuterium run and the hydrogen run is about a month, and we have seen already that the trigger performances are different for these two period. The approach we shall take is to study the run-by-run behaviour of several quantities and remove the periods during which they deviated significantly from their averages. By significantly, we mean that the quantity is at least four standard deviations away from the overall average. The measure of such a deviation for a quantity $y$ is the normalised residual $\Delta_y$ defined by

$$\Delta_y = \frac{\langle y_{run}\rangle - \langle y\rangle}{\sigma_y}$$

where $\langle y_{run}\rangle$ is the average of $y$ in a given run, $\langle y\rangle$ is the average for entire running period and $\sigma_y$ is the standard deviation of $y$ in the particular run under consideration.

The first quantity we monitor is the event yield, i.e. the number of reconstructed LAT events which fall within our chosen kinematical range per unit beam. In Fig. 3.41, we show the raw yield, when no corrections of any kind have been applied to it and the yield corrected for beam losses. Little time dependence is observed, except for a few runs that we shall remove from our data sample. Similar behaviour is observed for the yield corrected for beam losses (Fig. 3.42).

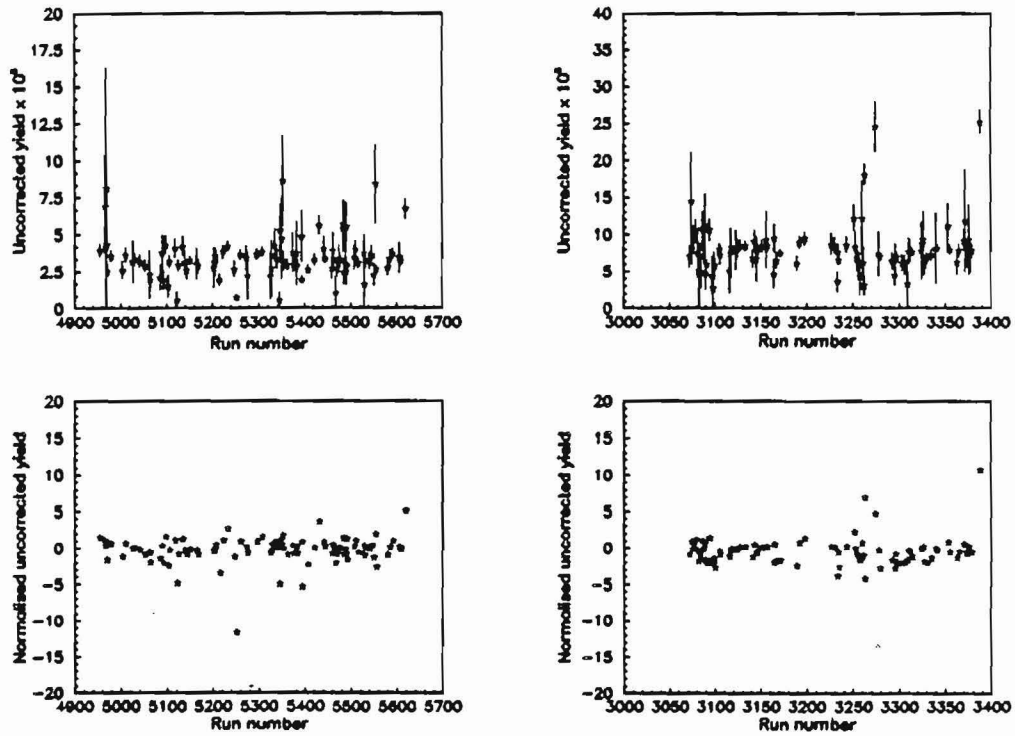


(a) (b)

**Time-dependence of uncorrected event yield for (a) hydrogen and (b) deuterium.**

**Fig. 3.41**

To convince ourselves that our data is reasonably stable, we have plotted the average $Q^2$, $\nu$ and $x_{bj}$ as a function of the run number. Again little time dependence is observed but for a few outlier runs.

In conclusion, the time variations of the running conditions do not impact significantly the uniformity of our data samples.

## 3.11 Fermi-motion correction

The extraction of neutron cross-sections is done by measuring deuterium cross-sections and subtracting the proton cross-sections. This amounts to saying that

$$\sigma_d = \sigma_n + \sigma_p \tag{3.10}$$

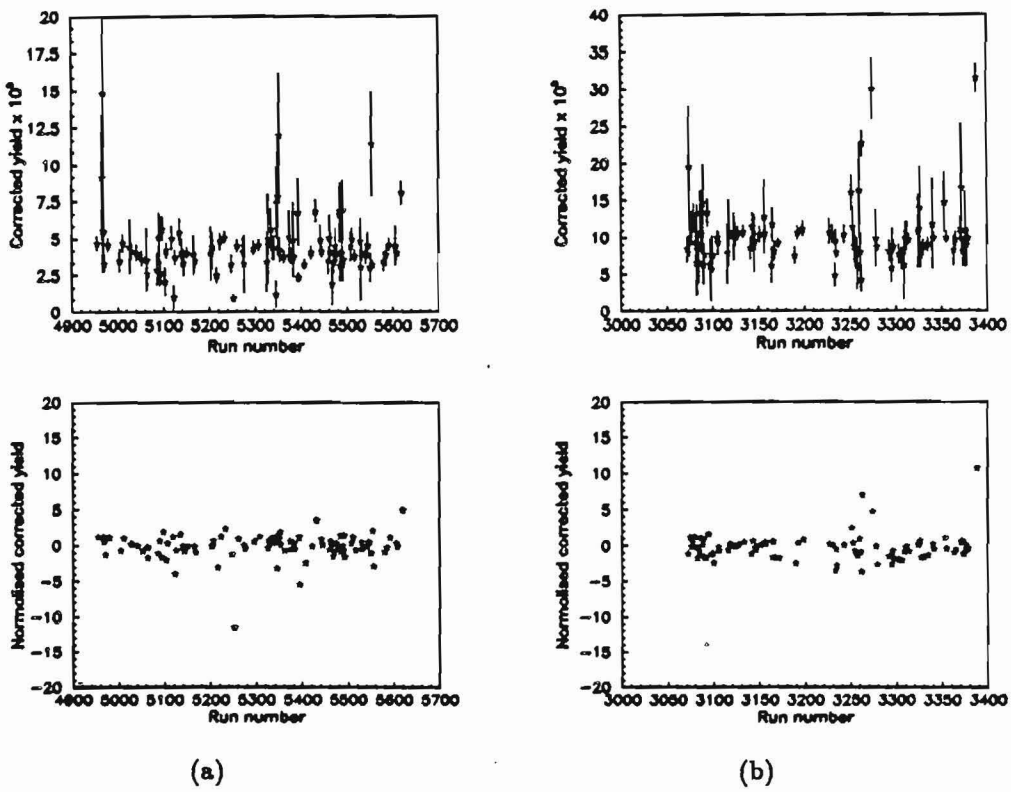


Time-dependence of corrected event yield for (a) hydrogen and (b) deuterium.

**Fig. 3.42**

where $\sigma_p$ is the proton cross-section, $\sigma_n$ the neutron cross-section and $\sigma_d$ the deuteron cross-section. Because the deuteron is a bound state of a neutron and a proton, Eq. 3.10 is not exact and must be corrected for Fermi motion. The relative motion of the nucleons in deuteron induces a Döppler-broadening effect which modifies the cross-section for three reasons (West, 1972; Atwood and West, 1973) :

(i) The beam energy in the rest frame of the deuteron (laboratory) is different from the beam energy seen from the rest frame of the target nucleon.

(ii) The beam flux measured in the rest frame of the target nucleon is not the same as the one measured in the lab.

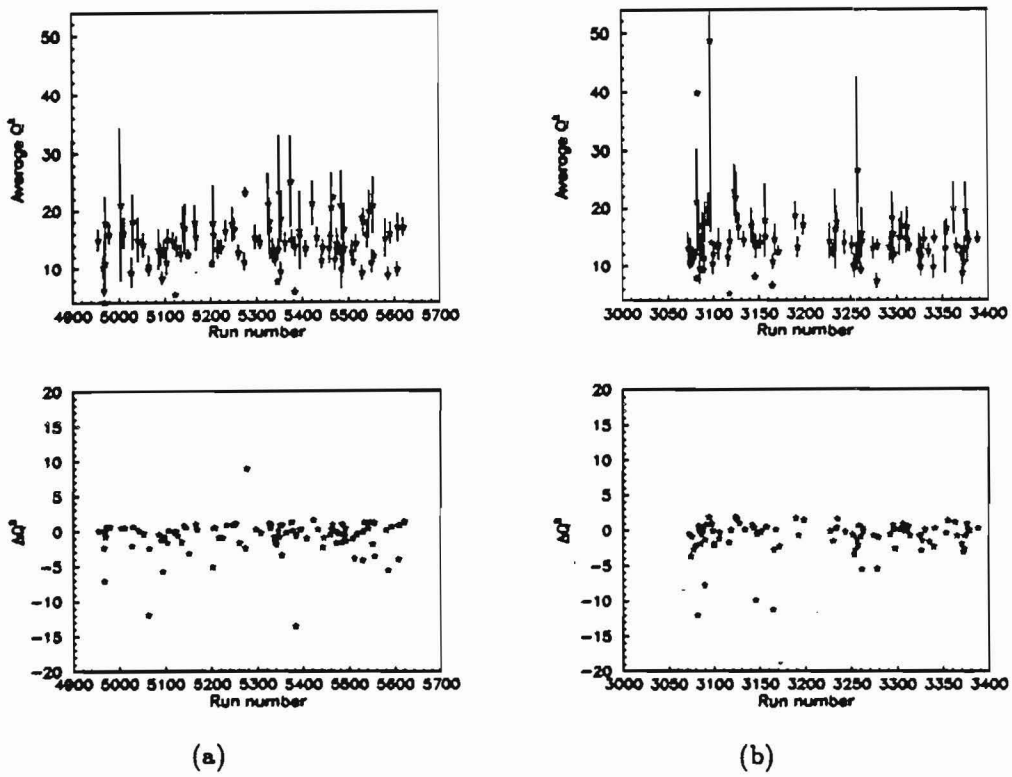


Time-dependence of $Q^2$ and the corresponding normalised residual for (a) hydrogen and (b) deuterium.

**Fig. 3.43**

(iii) The fact that the nucleons form a bound state imposes restriction on their momentum distribution.

(iii) has been pointed out by West (West, 1971). In the case of deep inelastic scattering, the momentum $p$ must satisfy

$$p \geq \frac{M((2-x_{bj})^2-1)}{2(2-x_{bj})} \tag{3.11}$$

In order to determine quantitatively how Döppler broadening changes the free-neutron cross-section, it is necessary to know the momentum distribution of the nucleons in the deuteron.

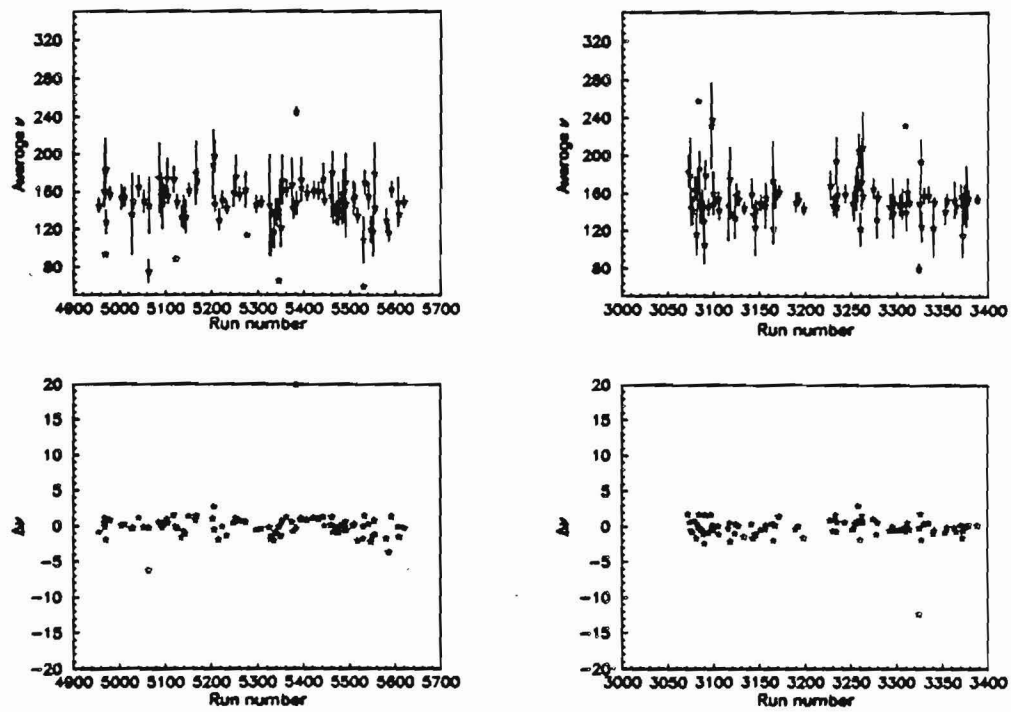


Time-dependence of $\nu$ and the corresponding normalised residual for (a) hydrogen and (b) deuterium.

**Fig. 3.44**

The traditional approach (West, 1972; Atwood and West, 1973) has been to use the non-relativistic wave function of the deuteron in the calculation of the Döppler-smeared deeply inelastic cross-section. The most general expression of the deuteron wave function $\psi_{SD}(r)$ in configuration space is given by

$$\psi_{SD}(r) = \frac{1}{r}(\cos\omega\, f_S(r)\mathcal{Y}^1_{110} + \sin\omega\, f_D(r)\mathcal{Y}^1_{112} \tag{3.12}$$

where the radial functions $f_S$ and $f_D$ are respectively the S- and D-state radial contributions, $\omega$ determines the relative proportion of the S- and D- states and $\mathcal{Y}^1_{110}$ and $\mathcal{Y}^1_{112}$ are spherical harmonics. The wave function is normalised to 1. The momentum distribution is merely the Fourier transform of $\psi_{SD}(r)$, which we shall denote by $\psi_{SD}(p)$, the determination of which is done by assuming an

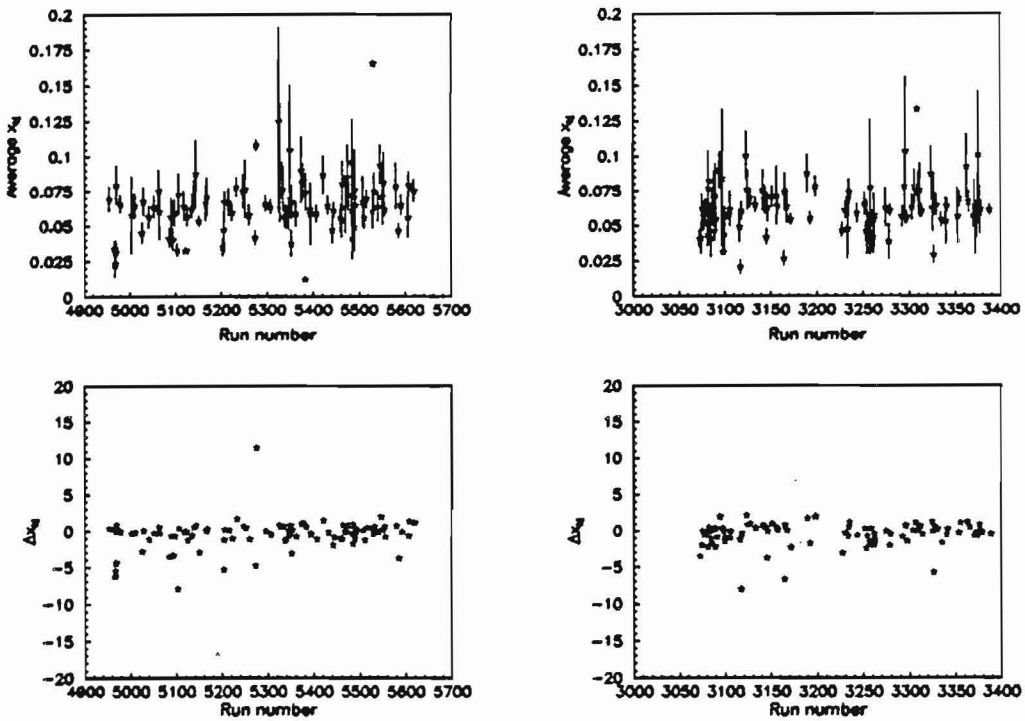


(a) (b)

Time-dependence of $x_{bj}$ and the corresponding normalised residual for (a) hydrogen and (b) deuterium.

**Fig. 3.45**

interaction potential between the nucleons.

Instead of working with cross-sections, we shall work directly with structure functions. According to (West, 1972) the relation between the smeared and the unsmeared cross-sections is given, in the limit of large $Q^2$, by

$$\begin{aligned} F_1^D &= 2\pi M x \int_0^\infty \frac{p}{p_i^0} |\psi_{DS}(p)|^2 \, dp \int_{x-}^{+} \frac{F_1(x')}{x'^2} \, dx' \\ F_2^D &= 2\pi M x^2 \int_0^\infty \frac{p}{p_i^0} |\psi_{DS}(p)|^2 \, dp \int_{x-}^{+} \frac{F_2(x')}{x'} \, dx' \end{aligned} \tag{3.13}$$

These expressions suffer, as has been pointed out in (Frankfurt,1978), from an ambiguous prescription for the normalisation of the wave-function. If Eq. 3.13

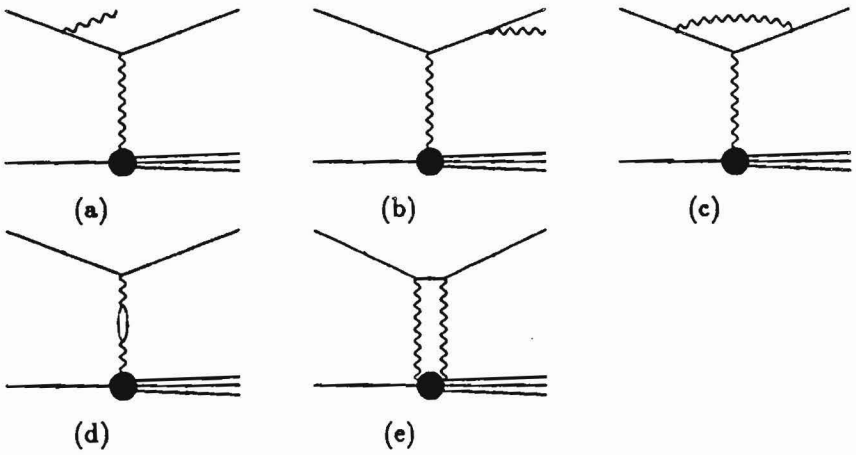


Lowest-order diagrams contributing to the deep-inelastic cross-section. (a),(b) Internal bremsstrahlung; (c) Vertex correction; (d) Vacuum polarisation; (e) Two-photon exchange.

**Fig. 3.46**

is used to unfold Fermi smearing, the correction is underestimated. Following (Frankfurt,1978), we shall write instead, in the scaling limit

$$W_1^D(\nu, Q^2) = \int \left( \frac{W_1^N(\alpha\nu, Q^2)}{\alpha} + \frac{p_T^2}{2M_N^2} \frac{W_2^N(\alpha\nu, Q^2)}{\alpha} \right) |\psi_{DS}(p)|^2 \, d^3p$$
$$\frac{W_2^D(\nu, Q^2)}{M_D^2} = \int \frac{\alpha}{M_N^2} W_2^N((\alpha\nu, Q^2)|\psi_{DS}(p)|^2 \, d^3p \tag{3.14}$$

where we refer to (Frankfurt,1978) for the notations.

The convolution equations of Eq. 3.14 have been used in (Aubert,1987), together with the Paris potential (Lacombe et al.,1981) as a basis for estimating the magnitude of Fermi motion on the neutron structure functions when extracted from the deuteron. The correction was found to be below 1% for $x_{bj}$ below 0.4. It becomes significant when $x_{bj}$ is above 0.65. Since our data sample does not allow us to go beyond 0.4 in $x_{bj}$, we shall ignore Fermi smearing altogether.

## 3.12 Radiative corrections

The one-photon exchange cross-section is directly related to the structure functions of the nucleon, but experimentally, the cross-section that we measure includes electromagnetic contributions traditionally known as *radiative corrections*. These corrections arise from higher-order diagrams, some of which are shown in Fig. 3.46.

In the past, the radiative corrections applied by most lepton scattering experiments have been those calculated by Mo and Tsai (Mo and Tsai, 1969), on the basis of diagrams (a-d) of Fig. 3.46. The authors made the approximation that most of the radiative contributions come from real photons the momenta of which are nearly colinear to the direction of either the incident lepton or the the direction of the outgoing lepton (peaking approximation). More recently, Akhundov, Bardin and Shumeĭko, (Akhundov et al., 1986b) have performed a more accurate, completely covariant calculation of the radiative corrections by taking into account diagrams of order higher than those of Fig. 3.46, including electroweak graphs.

For further details on the calculations, we refer the reader to Akhundov (1986a), Akhundov (1986b), Bardin and Shumeĭko (1979), Shumeĭko (1979).

The brief outline we shall give here follows closely (Lohmann,Akhundov 1990).

If we denote by $\sigma_m$ the measured cross-section and by $\sigma_0$ the one-photon exchange cross-section, then we can write

$$\sigma_m = (1 + \delta_{tot})\sigma_0$$

$\delta_{tot}$ is the total radiative correction.

The correction $\delta_{tot}$ can be written as

$$\delta_{tot} = \delta_{QED}(\alpha) + \delta_{QED}(\alpha^2) + \delta_{EW}(\frac{G_F}{\alpha})$$

$\delta_{QED}(\alpha)$ is a first-order QED correction, $\delta_{QED}(\alpha)^2$ is second-order QED correction and $\delta_{EW}(\frac{G_F}{\alpha})$ is a first-order electroweak interference correction, and $G_F$ is the Fermi coupling constant.

$\delta_{QED}(\alpha)$ can be written in turn as

$$\delta_{QED}(\alpha) = \delta_{vac}(\alpha) + \delta_{lepton}(\alpha) + \delta_{hadron}(\alpha)$$

and $\delta_{QED}(\alpha^2)$ can be written in turn as

$$\delta_{QED}(\alpha^2) = \delta_{vac}(\alpha^2) + \delta_{lepton}(\alpha^2) + \delta_{pair}(\alpha^2)$$

$\delta_{vac}$ is the contribution from the vacuum-polarisation graphs, including lepton and quark loops. $\delta_{lepton}$ is the contribution to the lepton vertex, arising from diagrams such as Fig. 3.46(a-c), $\delta_{hadron}(\alpha)$ is the contribution from the hadron vertex and $\delta_{pair}(\alpha^2)$ is the contribution from pair creation diagrams on the muon lines. In what follow, we shall briefly describe these corrections and give numerical estimates.

### *3.12.1 Lepton corrections*

The lepton correction $\delta_{lepton}$ can be written as a sum of an elastic contribution and an inelastic contribution.

$$\delta_{lepton} = \delta_{elastic} + \delta_{inelastic}$$

$\delta_{elastic}(\alpha)$ results from the process

$$\mu + N \rightarrow \mu + N + \gamma$$

where the target remains intact after scattering and a real photon is emitted. When the target is a nucleus, it is customary to distinguish between a coherent contribution to $\delta_{elastic}(\alpha)$, where the scattering occurs off the nucleus as a whole, and a quasi-elastic contribution where the scattering occurs off an individual nucleon in the nucleus. $\delta_{elastic}(\alpha)$ depends on the form factors of the target. The proton form factors were taken from a parametrisation given in (Bilen'kaya et al. 1974)

$$G_E^p = \frac{1}{\mu_p} G_M^p(Q^2) = \frac{1}{(1+b_1Q^2)(1+b_2Q^2)(1+b_3Q^2)}$$

with

$$b_1 = 0.61\,\mathrm{GeV}^{-2}$$

$$b_2 = 2.31\,\mathrm{GeV}^{-2}$$

$$b_3 = 0.04\,\mathrm{GeV}^{-2}$$

The deuteron elastic form factors have been taken from (Stein et al.,1975).

$\delta_{elastic}(\alpha^2)$ includes vacuum polarisation diagrams, one-loop diagrams and double-bremsstrahlung diagrams.

The inelatic radiative correction $\delta_{inelastic}$ stems from the process

$$\mu + N \rightarrow \mu + X + \gamma$$

where the target has been fragmented into a hadronic final state $X$. This contribution depends on the structure functions of the targets. The correction $\delta_{inelastic}(\alpha^2)$ is assumed to be independent of the hadronic final state and that

$$\frac{\delta_{inelastic}(\alpha^2)}{\delta_{inelastic}(\alpha)} = \frac{\delta_{elastic}(\alpha^2)}{\delta_{elastic}(\alpha)}$$

### *3.12.2 Hadron-vertex corrections*

The correction $\delta_{hadron}$ arising from photon emission at the hadron vertex can only be calculated if assumptions are made as to the nature of the interaction of the vitual photon with the target. The model used is that of the quark-parton model. The corrections were found to be typically very small.

### *3.12.3 Electroweak correction*

The contribution $\delta_{EW}(\frac{G_F}{\alpha})$ results from the interference of the one-photon exchange diagram with the Z-exchange diagram. Unlike the purely electromagnetic corrections, it depends on the sign and the polarisation of the muon.

### *3.12.4 Overall radiative corrections*

We have used the Bardin formalism to calculate $\delta_{tot}$ for deep inelastic scattering on hydrogen and deuterium. From a practical standpoint, we have used a program (TERAD86) that was given to us by S. Wimpenny (Lietzke,1989). It is described in (Lohmann,Akhundov,1990). This code is, with minor modifications, the same as the one used by the BCDMS collaboration to perform their radiative corrections. We have set the beam energy at its average value of 490 GeV, with a muon polarisation equal to -0.78. A minimum $Q^2$ of 4 GeV$^2$/c$^2$ has been imposed on the kinematical range, along with a minimum $x_{bj}$ of 0.003 and a maximum $y$ of 0.9. The $F_2$ structure function chosen is a global fit from (Morfin and Tung,1990) and the value of $R$, the ratio of longitudinal to transverse cross-section has been set to 0. In Fig. 3.47,

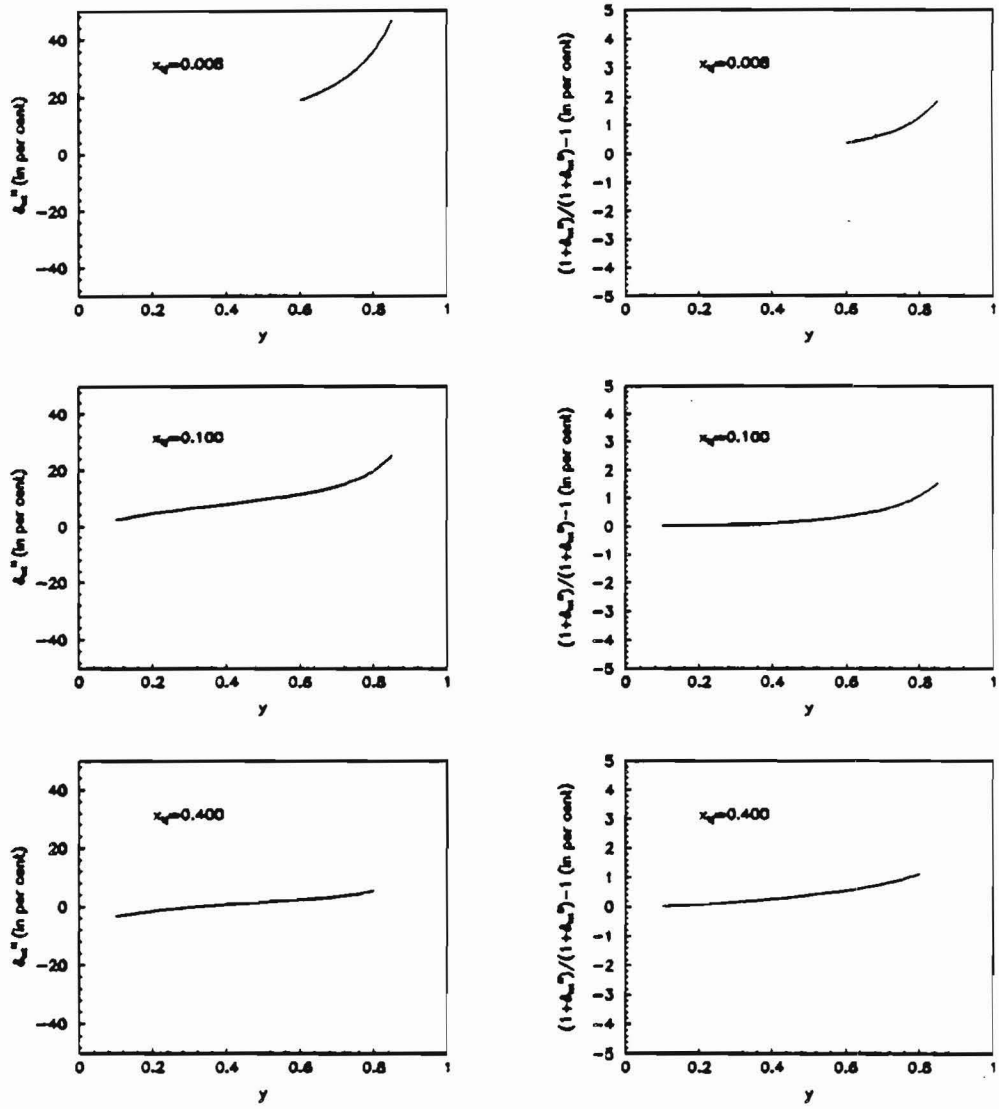


**Radiative corrections for hydrogen and deuterium, using Bardin calculations, as a function of y, for various values of $x_{bj}$.**

**Fig. 3.47**

we have plotted the total correction $\delta^H_{tot}$ for hydrogen and the ratio of the correction factors $(1+\delta^H_{tot})/(1+\delta^D_{tot})$ for hydrogen and deuterium. We can see that $\delta^H_{tot}$ rises with $y$, to reach values of 40% at low $x_{bj}$. However, the ratio of the radiative-correction factors does not deviate from 1 by more than 0.5% for $y$ is less than 0.65. Fig. 3.47 summarises the results. Whereas the value of $\delta_{tot}$

can be as high as 40% for large values of $y$, the ratio of the radiative correction factors between deuterium and hydrogen does not deviate from one by more than 2% at large y, and is nearly equal to one in our kinematical range for $y < 0.65$.

### 3.13 Analysis of the systematic uncertainties

In the study of the corrections that we need to apply in order to measure the cross-sections, we have attempted to give an estimate of the accuracy with which we know these corrections. Although we are confident about our knowledge of the effects discussed so far, it would be desirable to have an independent check of our estimate of these uncertainties.

For this purpose, we have compared the cross-section of production of elastic $\mu e$ events in hydrogen and deuterium. We do not measure the $\mu e$ cross-sections but only the ratio of the deuterium to hydrogen cross-section. The ratio is theoretically equal to one. Any deviation of this ratio from one is an indication of an unknown systematic effect which, therefore, has not been taken into account in the analysis.

We have selected a set of $\mu e$ elastic scattering events using a reduction program described in (Schmitt,1990d). An event is declared to be a candidate $\mu e$ elastic scattering if its $Q^2$ is greater than $10^{-6}\,\mathrm{GeV}^2/c^2$, its $\nu$ is greater 5 GeV, the number of tracks linked to the primary vertex, not including the beam and the scattered muon is equal to one and of a sign opposite to that of the muon, and finally if the fraction of energy carried by the candidate electron track is greater that 0.5.

We have reduced this sample by applying a number of constraints which

are as follows

$$z_\mu > 2\,\mathrm{cm}$$

$$r_\mu > 3\,\mathrm{cm}$$

$$-11.6\,\mathrm{m} < x_{vertex} < -10.6\,\mathrm{m}$$

$$2 \times 10^{-4} < x_{bj} < 10^{-3}$$

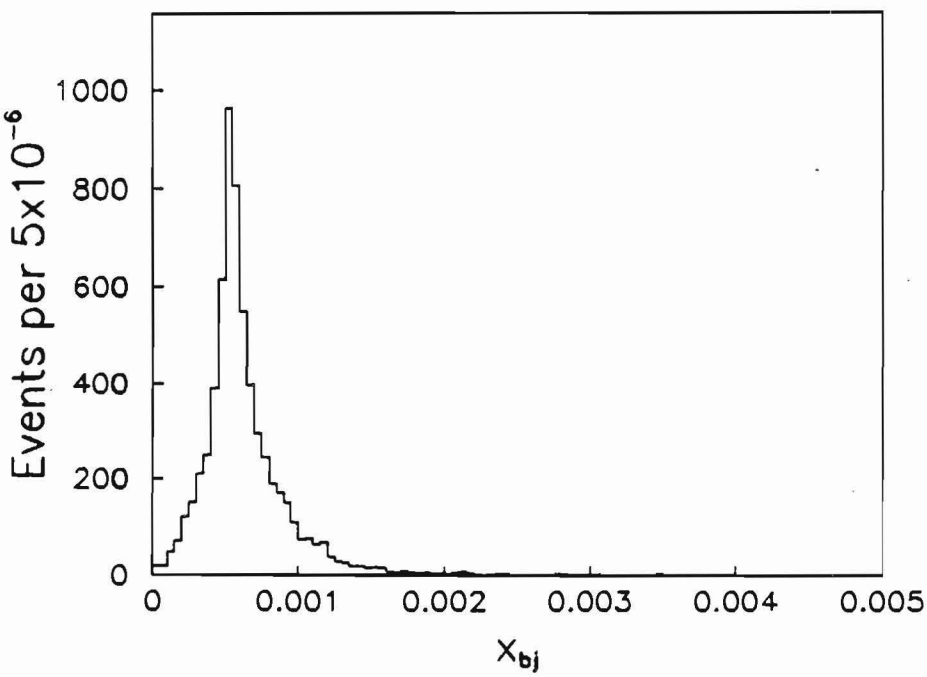


**$x_{bj}$ distribution of LAT $\mu e$ events for $H_2$.**
**Fig. 3.48**

The cut imposed on $x_{bj}$ is motivated by the fact that these events are elastic events and consequently, if the resolution on $x_{bj}$ were perfect, we would have

$$x_{bj} = \frac{M_e}{M_p}$$

where $M_e$ is the mass of the electron and $M_p$ is the mass of the proton. The

resolution on $x_{bj}$, as can be seen from Fig. 3.48, leads us to impose this cut in order to ensure the quality of the selected sample.

**Table 3.11**

| Cut | $\left(\frac{\sigma_D}{\sigma_H}\right)_{\mu e}$ |
|---|---|
| Basic cut | $1.13 \pm 0.04$ |
| $\theta \geq 5\,\mathrm{mrad}$ | $1.06 \pm 0.09$ |
| $y_\mu \leq -8\,\mathrm{cm}$ or $y_\mu \geq 2\,\mathrm{cm}$ | $1.14 \pm 0.04$ |
| $\theta \geq 5\,\mathrm{mrad}$ and ($y_\mu \leq -8\,\mathrm{cm}$ or $y_\mu \geq 2\,\mathrm{cm}$) | $1.06 \pm 0.09$ |
| $\theta \geq 5\,\mathrm{mrad}$ and $n_f^- = 1$ and ($y_\mu \leq -8\,\mathrm{cm}$ or $y_\mu \geq 2\,\mathrm{cm}$) | $1.11 \pm 0.10$ |

Ratio of deuterium to hydrogen $\mu e$ cross-sections as a function of various cuts. The basic cut listed in this table is described in the text. The basic cut is always applied in addition to the cuts listed in this table. The errors are statistical errors only.

In Table 3.11, we summarise the values that we obtain for the cross-section ratio $\left(\frac{\sigma_D}{\sigma_H}\right)_{\mu e}$. Regardless of how strict a cut we impose, the ratio is systematically greater than one, with, unfortunately, a statistical error comparable to the deviation from one. In order to constraint the sample of $\mu e$ events, we also have demanded that the number $n_f^-$ of negative fitted tracks to the primary vertex be exactly equal to one. In other words, since we have already have one negative track linked to the vertex, we require that it be fitted to the primary vertex. As can be seen in Table 3.11, the ratio is greater than one. We have

some evidence that there is a systematic difference between the hydrogen run and the deuterium run.

Now, we have seen that the difference in trigger efficiencies between hydrogen and deuterium is of the order of 1%. Furthermore, the difference in reconstruction efficiency between the two runs is overall of the order of 1% as estimated from Monte Carlo. In addition to this, we are confident about our beam normalisation. Granted that the $\mu e$ events may select different regions of the spectrometer compared to deeply inelastic scattering events, the deviation indicated by the $\mu e$ ratio may not apply to the ratio of deeply inelastic cross-sections; and clearly, we cannot use the $\mu e$ ratio to correct the deeply inelastic ratio. But it can still be taken as an estimate of all the systematic effects, including those that have not been modelled in the Monte Carlo simulation. As a result of this, we shall take 6% as an estimate of the systematic uncertainties entering in the ratio of the deuterium to hydrogen cross-sections (per nucleon). This translates to roughly a 12% uncertainty on the neutron-to-proton cross-section ratio, and more specifically we shall allow the latter to be lowered by as much as 12% in any bin.

### 3.14 Summary

In the previous sections of the present chapter, we have analysed the sources of the corrections needed to measure cross-sections. At this stage, it is worth pausing and summarising the results we have obtained so far.

To this end, we have regrouped all the corrections that need to be applied in order to measure the cross-section per nucleon in Table 3.12.

We have calculated the geometrical acceptance of the trigger by Monte Carlo. It is a necessary correction for measuring absolute cross-sections, but it cancels out in the ratio.

Next we have measured the efficiency of the large-angle trigger. We have

**Table 3.12**

| $x_{bj}$ | | 0.005–0.028 | 0.028–0.05 | 0.05–0.08 | 0.08–0.16 | 0.16–1.00 |
|---|---|---|---|---|---|---|
| Beam | $H_2$ | $0.8129 \pm 0.0009 \pm 0.0017$ | | | | |
| | $D_2$ | $0.8117 \pm 0.0009 \pm 0.0017$ | | | | |
| $D_2$ purity | | 1.023 | 1.023 | 1.023 | 1.022 | 1.023 |
| Empty target | $H_2$ | 0.972 | | | | |
| | $D_2$ | 0.988 | | | | |
| Trigger | $H_2$ | $1.023 \pm 0.004 \pm 0.020$ | | | | |
| | $D_2$ | $1.027 \pm 0.006 \pm 0.026$ | | | | |
| Software | $H_2$ | $1.14 \pm 0.02$ | $1.09 \pm 0.01$ | $1.09 \pm 0.02$ | $1.06 \pm 0.01$ | $1.05 \pm 0.01$ |
| | $D_2$ | $1.10 \pm 0.01$ | $1.08 \pm 0.01$ | $1.07 \pm 0.01$ | $1.06 \pm 0.01$ | $1.05 \pm 0.01$ |
| Acceptance | | $3.92 \pm 0.08$ | $3.95 \pm 0.09$ | $3.21 \pm 0.08$ | $2.47 \pm 0.06$ | $2.28 \pm 0.07$ |
| Radiative corrections | $H_2$ | 0.856 | 0.879 | 0.932 | 0.958 | 0.984 |
| | $D_2$ | 0.857 | 0.887 | 0.932 | 0.957 | 0.985 |
| Fermi motion | | No correction applied | | | | |

**Corrections factors to be applied to observed cross-sections per nucleon for hydrogen and deuterium in order to obtain the true cross-sections. The beam correction is to be applied to the number of beams in order to get the useful number of beams. The first error is statistical, the second one is systematic.**

found that the hardware and the electronic efficiencies are very close to unit only for the upper half of the muon triggering system. The lower half of the muon triggering system cannot be used because of an unstable and inefficient

performance resulting from a mis-timing of the signals. Restricting our data to those events where the muon traverses only the upper half of the SPM scintillators, it was found that the residual inefficiency comes from self-vetoing events. This induces a correction of 2 to 3% on the cross-sections, with a systematic uncertainty of the order of 2 to 3%. It was also found that when the distance of closest approach of the muon to the SMS veto is at least 3 cm, the trigger efficiencies of the deuterium period and the hydrogen period agree within 1%.

Next we have determined the number of useful beam muons that went into the generation of our final data sample. In order to check the reliability of our beam counting we have compared the number of beams reported by the event scalers and the number of random beams selected by the RBEAM trigger. When the number of such RBEAM is scaled appropriately, the resulting number agrees within 0.2% with the number given by the event scalers. The beam correction factor, that is, the factor by which the total number of RBEAM triggers must be multiplied in order to get the number of useful beams has a statistical uncertainty of the order of 0.1%. In view of this, we consider the systematic uncertainty on our normalisation to be negligible.

We have estimated the efficiency of the reconstruction software by a hybrid procedure. The efficiency of the pattern-recognition code was calculated from a Monte Carlo integration the input to which is the efficiency of the wire chambers. The part of the inefficiency of the muon matching software that could not be estimated from Monte Carlo has been measured from data and was found to be $(1.9 \pm 0.7)\%$. The vertex-reconstruction code was found to be nearly 100% efficient.

However, it was found that there is some discordance, at the level of 5%, between a reconstruction efficiency measurement extracted from data and the Monte Carlo calculation. Due to a lack of time, it has not been possible to investigate the problem in greater detail. In particular, we do not know if the

hydrogen and the deuterium runs show similar discrepancies.

The background resulting from beams interacting outside the target vessel has been measured from data taken with an empty target vessel. The contamination from *mue* elastic scattering events was found to be negligible. Events originating from muon interactions in the target vessel leads to a 2.8% correction for hydrogen and 1.2% correction for deuterium.

Radiative corrections have been calculating with TERAD86, a program written by Bardin et al. The corrections are as high as 13% in the lowest $x_{bj}$ bin, but they are nearly identical for hydrogen and deuterium, typically within 1%.

Based on their negligible size, corrections due to Fermi motion will be neglected.

Impurities in the deuterium target lead to a correction of the order of 2.3% on the deuterium cross-section, and henceforth on the cross-section ratio. This correction is nearly independent of $x_{bj}$.

Finally, we have performed an independent check of the relative normalisation of the hydrogen and the deuterium samples by comparing the uncorrected $\mu e$ cross-sections from the two targets. It was found that they are discordant at the 10% level. We believe that this may be related to the reconstruction efficiency discrepancy between the Monte Carlo calculation and some observations in data. In view of this, the neutron to proton cross-section ratio will be assigned a systematic uncertainty of the order of 12%, in all bins.

# *Chapter 4*

# Final results

In the previous sections, we have dwelt at some length on the instrumental effects that we need to take into account in order to extract either absolute cross-sections or cross-section ratios. It is now time to present our final measurements.

In all subsequent results, the following cuts will be in effect

*1 in-time beam and no out-of-time beam*

$$Q^2 > 4\,\mathrm{GeV}^2/\mathrm{c}^2$$

$$\nu > 50\,\mathrm{GeV}$$

$$y < 0.65$$

$$x_{bj} > 0.005$$

$$\theta > 5\,\mathrm{mrad}$$

$$r_\mu > 0.03\,\mathrm{m}$$

$$z_\mu > 0.02\,\mathrm{m}$$

$$y_\mu < -0.08\,\mathrm{m} \text{ or } y_\mu > 0.02\,\mathrm{m}$$

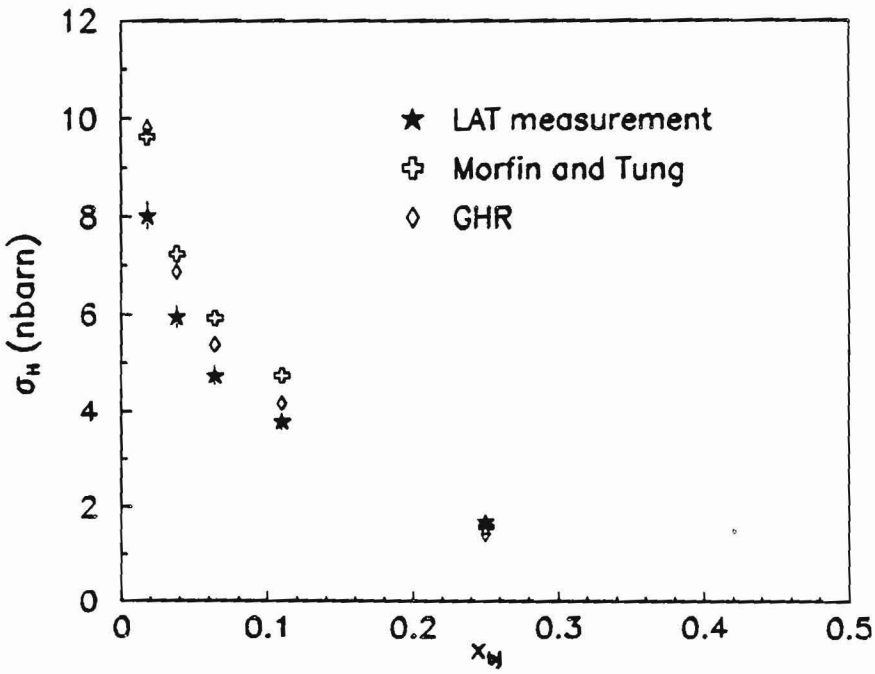


(a)

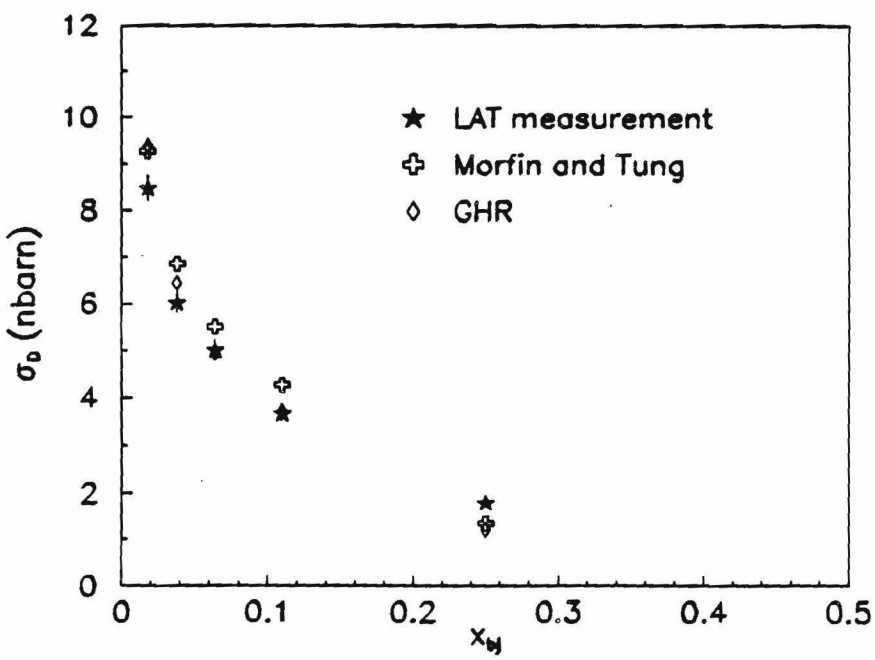


(b)

**Cross-sections for (a) hydrogen and (b) deuterium, compared to Morfin and Tung and GHR.**
**Fig. 4.1**

In order to extract the cross-sections, we have corrected for beam losses,

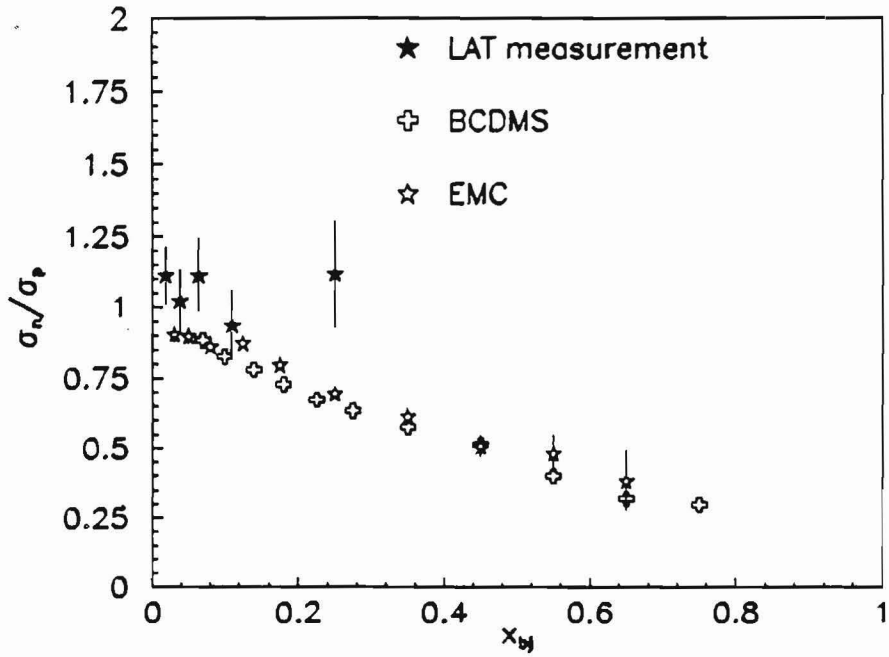


**Neutron to proton cross-section ratio from this measurement, compared to EMC and BCDMS.**
**Fig. 4.2**

acceptance, muon reconstruction efficiency, and trigger efficiency as described in the previous chapter. Furthermore, we have divided the $x_{bj}$ range as follows

$$0.005 - 0.028$$

$$0.028 - 0.05$$

$$0.05 - 0.08$$

$$0.08 - 0.16$$

$$0.16 - 1$$

and we report the cross-section $\sigma$ in each $x_{bj}$ bin $[x, x + \delta x]$ defined by

$$\sigma = \int_{x}^{x+\delta x} \left( \int_{Q^2} \frac{d^2\sigma}{dx\, dQ^2}\, dQ^2 \right) dx$$

Our final sample consists of 2741 hydrogen events, generated by $9.572 \times 10^{10}$

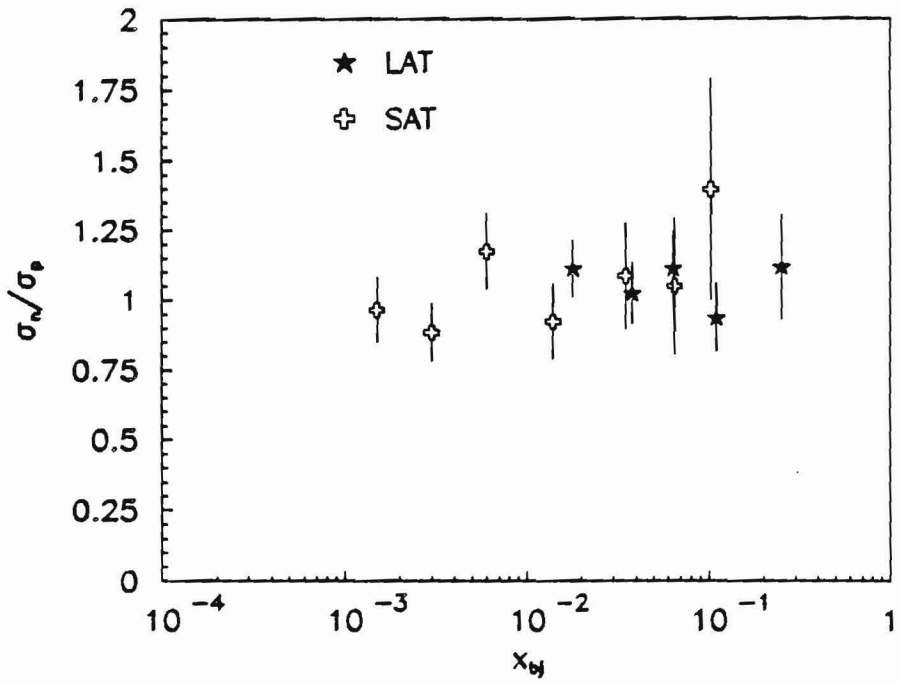


**Neutron-to-proton cross-section ratio from this measurement, compared to that obtained with the SAT trigger (Bhatti,1991).**

**Fig. 4.3**

beam muons and 3071 deuterium events, generated by $4.716 \times 10^{10}$ muons. The average $Q^2$ for both samples is approximately 15.5 $\mathrm{GeV}^2$ and the average energy transfer $\nu$ is about 155 GeV.

The cross-sections for proton and neutron are shown in Fig. 4.1 as a function of $x_{bj}$, integrated over the $Q^2$ range of the experiment. They are compared to a parametrisation from (Gluck, Hoffmann, Reya, 1982) (GHR) and a more recent parametrisation from (Morfin and Tung,1990). The actual values are shown in Table 4.1. The errors are statistical errors only. The discrepancy between the theoretical parametrisation and our measurement originates from systematic effects we discussed in the previous chapter. We believe that our

**Table 4.1**

| $x_{bj}$ | 0.005–0.028 | 0.028–0.05 | 0.05–0.08 | 0.08–0.16 | 0.16–1.00 |
|---|---|---|---|---|---|
| $\langle x_{bj} \rangle$ | 0.018 | 0.038 | 0.064 | 0.11 | 0.25 |
| $\langle Q^2 \rangle$ (GeV$^2$) | 7.0 | 10.6 | 14.3 | 22.1 | 48.5 |
| $\sigma$ (nbarn) p | $8.03 \pm 0.28$ | $5.96 \pm 0.23$ | $4.75 \pm 0.21$ | $3.78 \pm 0.17$ | $1.70 \pm 0.11$ |
| $\sigma$ (nbarn) D | $8.48 \pm 0.28$ | $6.03 \pm 0.23$ | $5.02 \pm 0.21$ | $3.67 \pm 0.16$ | $1.80 \pm 0.11$ |
| $F_2^p$ (MT) | 0.341 | 0.377 | 0.404 | 0.421 | 0.359 |
| $F_2^D$ (MT) | 0.328 | 0.356 | 0.375 | 0.380 | 0.297 |
| $F_2^D$ (NMC) | 0.357 | 0.357 | 0.351 | 0.335 | 0.268 |
| r | $1.11 \pm 0.10$ | $1.03 \pm 0.11$ | $1.11 \pm 0.13$ | $0.94 \pm 0.12$ | $1.12 \pm 0.19$ |
| $S_G^1$ | $-0.066 \pm 0.059$ | $-0.006 \pm 0.024$ | $-0.021 \pm 0.024$ | $0.018 \pm 0.036$ | $-0.082 \pm 0.124$ |
| $S_G^2$ | $-0.030 \pm 0.051$ | $-0.003 \pm 0.022$ | $-0.009 \pm 0.020$ | $0.008 \pm 0.034$ | $-0.032 \pm 0.091$ |
| $S_G^3$ | $-0.033 \pm 0.056$ | $-0.003 \pm 0.022$ | $-0.009 \pm 0.019$ | $0.007 \pm 0.030$ | $-0.029 \pm 0.082$ |

Final results

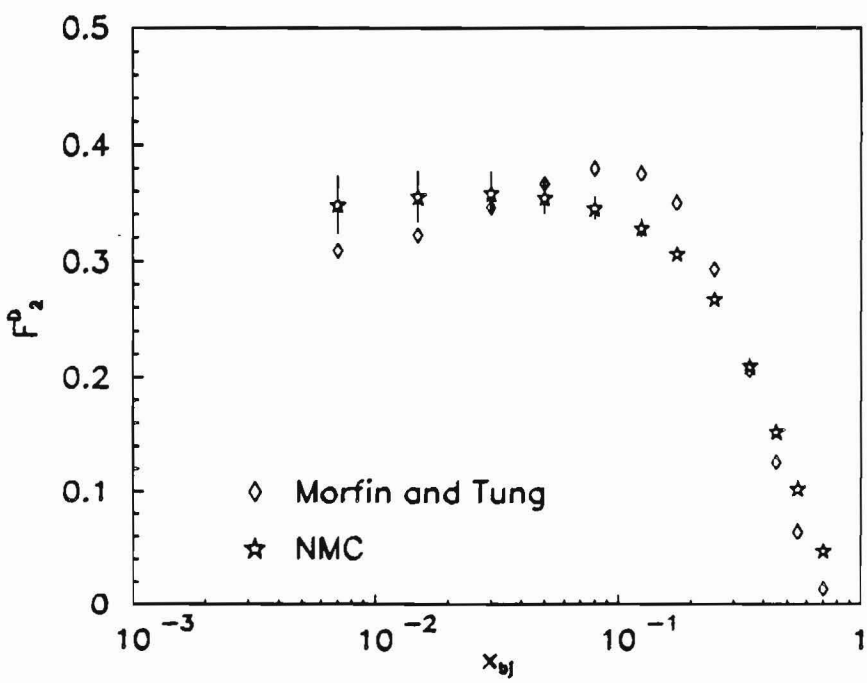


Morfin and Tung parametrisation of the deuterium structure function (1990), compared to the parametrisation used by NMC (Amaudrus,1991)

**Fig. 4.4**

cross-section measurement is accurate to within 15%. The ratio of the neutron to proton cross-section is shown in Fig. 4.2, where we compare our results to those from EMC and BCDMS. Comparison of our measured ratio to that obtained using the SAT trigger (Bhatti,1991) shows that, within errors, the LAT measurement is consistent with the SAT measurement in the overlap region (Fig. 4.3). We recall from the previous chapter that we have assigned a 6% systematic uncertainty to the deuterium to hydrogen cross-section ratio, which translates to roughly a 12% systematic uncertainty on the neutron to proton cross-section ratio. More specifically, we allow our ratio to be *lowered* by 12% in all bins.

The measurement of the neutron-to-proton cross-section ratio allows us to calculate the contribution $S(x_0, x_1)$ to the Gottfried integral

$$S(x_0, x_1) = \int_{x_0}^{x_1} \left(F_2^p - F_2^n\right) \frac{dx}{x}$$

This contribution can be written as

$$S(x_0, x_1) = \int_{x_0}^{x_1} F_2^p \left(1 - r\right) \frac{dx}{x}$$

where

$$r = \frac{F_2^n}{F_2^p}$$

is our *measured* cross-section ratio.

In principle, we need a measurement of $F_2^p$ in order to determine the Gottfried integral in our kinematical range. Since our data do not allow us to measure $F_2^p$ accurately, we shall use parametrisations of the proton structure function. Now, $S(x_0, x_1)$ can be approximated by

$$S(x_0, x_1) = \sum_{i=1}^{n} F_{2i}^p \left(1 - r_i\right) \left(\log x_{i+1} - \log x_i\right)$$

over the $n$ bins of our $x_{bj}$ range. $F_{2i}^p$ is the value of $F_2^p$ evaluated at the average of $x_{bj}$ in bin $i$ and $r_i$ is the ratio $r$ reported at the average of $x_{bj}$ in bin $i$.

The statistical error $\sigma_S$ associated to $S(x_0, x_1)$ is given by

$$\sigma_S^2 = \sum_{i=1}^{n} (F_{2i}^p)^2 \, \sigma_{r_i}^2 \, (\log x_{i+1} - \log x_i)^2$$

where $\sigma_{r_i}$ is the statistical error on the ratio $r$ in bin $i$. Similarly, we can use a parametrisation of the deuterium structure function per nucleon $F_2^D$, in which case the Gottfried integral can be approximated by

$$S(x_0, x_1) = \sum_{i=1}^{n} 2F_{2i}^D \left(\frac{1 - r_i}{1 + r_i}\right) (\log x_{i+1} - \log x_i)$$

In Table 4.1, we present a summary of our results. Most of the entries are self-explanatory, but some of them deserve a comment.

$S_G^1$ is the Gottfried integral in each bin evaluated using the Morfin and Tung parametrisation of the *proton* structure function. $S_G^2$ is the Gottfried integral evaluated using the Morfin and Tung parametrisation of the *deuteron* structure function. Finally, $S_G^3$ has been evaluated the same parametrisation used by the NMC (Amaudruz,1991). We have interpolated the values reported by the NMC to our $x_{bj}$ values. These structure functions have been evaluated at $Q^2 = 4\,GeV^2$.

In our evaluation of the Gottfried integral $S(x_0, x_1)$, we discard the last bin since it spans too wide a range to allow an accurate estimate of the integral. We find

$$S_G^1(0.005, 0.16) = -0.075 \pm 0.077$$

$$S_G^2(0.005, 0.16) = -0.067 \pm 0.068$$

$$S_G^3(0.005, 0.16) = -0.074 \pm 0.070$$

where the errors are statistical. The above values are consistent within the statistical uncertainties, which shows that at our level of precision, the Gottfried sum is not sensitive to the choice of structure function.

Now, if we allow the deuterium to hydrogen cross-section to be lowered by 6% by raising the hydrogen cross-section by the same relative amount, ratio to be decreased by 10%, we shall get new $S_G^1$, $S_G^2$ and $S_G^3$. This will allow us to have an estimate on the systematic uncertainty on the Gottfried integral. With this prescription, we find

$$S_G^1(0.005, 0.16) = 0.075 \pm 0.073$$

$$S_G^2(0.005, 0.16) = 0.074 \pm 0.073$$

$$S_G^3(0.005, 0.16) = 0.068 \pm 0.074$$

To compare our result with that of the NMC, we shall take $S_G^3$ as our final measurement, albeit such a choice is quite arbitrary. Our systematic uncertainty will be estimated by taking the average of the nominal value of the Gottfried integral and the one resulting from lowering the deuterium to proton ratio. An estimate of the systematic uncertainty will be given by half the distance between these two numbers. Consequently,

$$S_G(0.005, 0.16) = -0.003 \pm 0.074\,(\text{stat.}) \ \pm 0.071\,(syst.)$$

The NMC (Amaudruz,1991) measured the Gottfried integral for $x_{bj}$ between 0.004 and 0.8 and found

$$S_G(0.004, 0.8) = 0.227 \pm 0.007\,(\text{stat}) \ \pm 0.014\,(\text{syst})$$

This value was obtained by measuring the neutron-to-proton cross-section ratio and by assuming a parametrisation for the deuterium structure function $F_2^D$,

based on measurements done by SLAC, BCDMS, EMC , and CHIO. The parametrisation used by the NMC is shown in Fig. 4.4, where we compare it to the Morfin and Tung parametrisation.

The NMC Gottfried integral between $x_{bj} = 0.004$ and $x_{bj} = 0.15$ (which is nearly the same as the range in which our measurement is performed) is

$$S_G(0.004, 0.15) = 0.067$$

which is consistent with our measurement within errors.

In conclusion, our neutron to proton cross-section ratio measured with a large-angle trigger is consistent with unity at low $x_{bj}$. It is consistent with the measurement performed with the small-angle trigger in the kinematical region where the two triggers overlap. Our estimate of the Gottfried integral agrees within errors with the measurement performed by the New Muon Collaboration in the overlapping kinematical range, namely for $x_{bj}$ lying between 0.005 and 0.16.

# Conclusion

Experiment 665 at Fermilab has measured the ratio of the neutron to proton deeply inelastic cross-section with muons, at an incident beam energy of 490 GeV. The measurement was performed with a large-angle trigger, at a minimum $Q^2$ of $4\,\mathrm{GeV}^2/c^2$ and minimum $x_{bj}$ of 0.005. It was found that this ratio was consistent with unity at low $x_{bj}$. This ratio was compared with that obatined independently using a small-angle trigger (Bhatti,1991). Both measurements were found to be consistent in the $x_{bj}$ range where they overlap. From this ratio, we have estimated the contribution to the Gottfried integral and found that it is consistent with the value obtained by the New Muon Collaboration at CERN (Amaudruz,1991).

# Appendix A

## Statistical methods

In this appendix, we shall present some statistical results that, in the course of our analysis, we felt compelled to derive. Although the material presented here is not new, we have judged it useful to regroup it here for the benefit of those who may wish to understand the underlying mathematical arguments leading to formulae that are so valuable in the field of High Energy Physics. The reader who is interested in getting more acquainted with statistical methods may refer to (Kendall et al., 1987), or at a more elementary level (Dudewicz and Mishra, 1988). The work of (Eadie,1971) may prove also most useful and is more closely related to problems that one faces in High Energy Physics.

Recently, the field of robust statistical estimation, which, for a long time has been considered as the poor man's way of handling random samples, has gained significant importance. We shall not discuss the use of non-parametric methods here, but we refer to (Roussew,1987) and (Hettmansperger, 1984).

### A.2 Distribution of the ratio of two random variables

Given two independent random variables $X$ and $Y$ with respective probability distributions $f(x)$ and $g(y)$, we wish to know the probability distribution $h(z)$ of the random variable $Z = X/Y$. The case where both $X$ and $Y$ follow Gaussian distributions is of particular interest and will be treated in detail in this section. In what follows, we shall denote by $P(A)$ the probability that event $A$ occurs, by $P(A|B)$ the conditional probability that event $A$ occurs given $B$. The derivation of the distribution of $Z$ relies on the Theorem of

Total Probabilities which states that

$$P(A) = \sum_{n=1}^{\infty} P(A|B_n)P(B_n) \tag{A.1}$$

provided that events $B_n$ are incompatible and their total probability adds to unity.

The probability distribution $h(z)$ is given by

$$h(z) = \frac{P\left\{\frac{X}{Y} \in [z,\, z+dz[\,\right\}}{dz}$$

Let us split the domain of $Y$ into $Y > 0$ and $Y < 0$. Then we can write

$$\begin{aligned} P\left\{\frac{X}{Y} \in [z,\, z+dz[\,\right\} = & P\left\{Y > 0 \quad and \quad \frac{X}{Y} \in [z,\, z+dz[\,\right\} + \\ & P\left\{Y < 0 \quad and \quad \frac{X}{Y} \in [z,\, z+dz[\,\right\} \end{aligned} \tag{A.2}$$

Let us evaluate the first term of the right-hand side of Eq. A.2. From Eq. A.1

$$\begin{aligned} & P\left\{Y > 0 \quad and \quad \frac{X}{Y} \in [z,\, z+dz[\,\right\} = \\ & \int_{y=0}^{+\infty} P\left\{X \in [yz,\, yz + y\,dz[\ \middle|\ Y \in [y,\, y+dy[\,\right\} P\left\{Y \in [y,\, y+dy[\,\right\} = \\ & \left(\int_0^{+\infty} y\, f(yz)\, g(y)\, dy\right) dz \end{aligned} \tag{A.3}$$

Similarly we find that the second term of the right-hand side of Eq. A.2 is given by

$$P\left\{Y < 0 \quad and \quad \frac{X}{Y} \in [z,\, z+dz[\,\right\} = -\left(\int_{-\infty}^{0} y\, f(yz)\, g(y)\, dy\right) dz \tag{A.4}$$

and therefore combining Eq. A.3 and Eq. A.4 we get for the probability distribution $h(z)$ of $Z$

$$h(z) = \int_0^{+\infty} y\, f(yz)\, g(y)\, dy - \int_{-\infty}^{0} y\, f(yz)\, g(y)\, dy \tag{A.5}$$

We shall apply Eq. A.5 to the case where $X$ and $Y$ both have a Gaussian probability distribution function.

$$f(x) = \frac{1}{\sqrt{2\pi}\,\sigma_1} e^{-\frac{(x-\mu_1)^2}{2\sigma_1^2}}$$

$$g(y) = \frac{1}{\sqrt{2\pi}\sigma_2} e^{-\frac{(y-\mu_2)^2}{2\sigma_2^2}}$$

In this case, $h(z)$ will be given by

$$h(z) = \frac{1}{2\pi\sigma_1\sigma_2}\int_0^{+\infty} y\, e^{-\frac{1}{2}\left\{\frac{(yz-\mu_1)^2}{\sigma_1^2}+\frac{(y-\mu_2)^2}{\sigma_2^2}\right\}} dy \; - \; \frac{1}{2\pi\sigma_1\sigma_2}\int_{-\infty}^{0} y\, e^{-\frac{1}{2}\left\{\frac{(yz-\mu_1)^2}{\sigma_1^2}+\frac{(y-\mu_2)^2}{\sigma_2^2}\right\}} dy \tag{A.6}$$

If we set

$$\zeta = \frac{\frac{\mu_1 z}{\sigma_1^2}+\frac{\mu_2}{\sigma_2^2}}{\frac{z^2}{\sigma_1^2}+\frac{1}{\sigma_2^2}} \qquad \gamma = \sqrt{\frac{1}{\frac{z^2}{\sigma_1^2}+\frac{1}{\sigma_2^2}}} \qquad \delta^2 = \frac{\mu_1^2}{\sigma_1^2}+\frac{\mu_2^2}{\sigma_2^2}$$

then Eq. A.6 becomes

$$h(z) = \frac{1}{2\pi\sigma_1\sigma_2} e^{-\frac{1}{2}\left\{\delta^2-\frac{\zeta^2}{\gamma^2}\right\}}\left\{\int_0^{+\infty} y\, e^{-\frac{(y-\zeta)^2}{2\gamma^2}} dy \; - \int_{-\infty}^{0} y\, e^{-\frac{(y-\zeta)^2}{2\gamma^2}} dy\right\} \tag{A.7}$$

The integrals in Eq. A.7 are easily evaluated, and the expression for $h(z)$ becomes

$$h(z) = \frac{1}{2\pi\sigma_1\sigma_2} e^{-\frac{1}{2}\left\{\delta^2-\frac{\zeta^2}{\gamma^2}\right\}}\left\{2\gamma^2 e^{-\frac{\zeta^2}{2\gamma^2}} + \sqrt{2\pi}\zeta\gamma\left(1-2\Phi\left(-\frac{\zeta}{\gamma}\right)\right)\right\} \tag{A.8}$$

where the function $\Phi$ is defined by

$$\Phi(t) = \int_{-\infty}^{t} e^{-\frac{u^2}{2}} du$$

In the particular case where $\mu_1 = \mu_2 = 0$ and $\sigma_1 = \sigma_2 = \sigma$, the expression of $h(z)$ reduces to

$$h(z) = \frac{1}{\pi} \frac{1}{1+z^2}$$

that is, the ratio of the random variables $X$ and $Y$ follows a Cauchy distribution which has the remarkable property of not having any moment. In particular, it has no mean and consequently no variance. It can be shown from Eq. A.8 that $h(z)$ behaves asymptotically as $\frac{1}{z^2}$ as $z \to \infty$. This means that the ratio of two gaussian distributions has neither mean nor variance.

For practical applications, we shall assume that

$$\frac{\sigma_1}{\mu_1} \ll 1$$

$$\frac{\sigma_2}{\mu_2} \ll 1$$

This implies that the range of the random variables $X$ and $Y$ is essentially the positive real line. Then the distribution of $Z$ is approximately given by

$$h(z) = \frac{\mu_1 \sigma_2^2 z + \mu_2 \sigma_1^2}{\sqrt{2\pi}\left(\sigma_2^2 z^2 + \sigma_1^2\right)^{\frac{3}{2}}} e^{-\frac{1}{2}\frac{\left(\mu_2 z - \mu_1\right)^2}{\sigma_2^2 z^2 + \sigma_1^2}}$$

and it is then clear that the random variable $T$ defined by

$$T = \frac{\mu_2 - \mu_1 Z}{\sqrt{\sigma_1^2 Z^2 + \sigma_2^2}}$$

is normally distributed, with zero mean and unit variance.

Let us apply this result to the ratio $r$ of the parameters $p_1$ and $p_2$ of two binomial distributions. Our goal is to find a $1-\alpha$ confidence interval for $r = p_1/p_2$. Let $x_1$ and $n_1$ be respectively the number of successes and trials of the first binomial, and similarly for the second binomial, $x_2$ and $n_2$. Then the estimators of $p_1$ and $p_2$ are respectively $x_1/n_1$ and $x_2/n_2$. In the limit of large samples, $x_1/n1$ and $x_2/n_2$ are approximately gaussian distributed, with respective means $p_1, p_2$ and respective variances $p_1(1-p_1)/n_1$ and $p_2(1-p_2)/n_2$. We then apply the previous results to the ratio $Z$ of $x_1/n_1$ and $x_2/n_2$. The variable

$$T = \frac{p_1 - p_2 Z}{\sqrt{\frac{p_2(1-p_2)}{n_2} Z^2 + \frac{p_1(1-p_1)}{n_1}}}$$

$$= \frac{p_2(r - Z)}{\sqrt{\frac{p_2(1-p_2)}{n_2} Z^2 + \frac{r p_2(1-r p_2)}{n_1}}}$$

is approximately normally distributed, with zero mean and unit variance. To find a $(1-\alpha)$ confidence interval for $r$, we choose $\lambda$ such

$$P\left\{-\lambda \leq T \leq \lambda\right\} = 1 - \alpha$$

Solving for $r$ we then find that the confidence limits are solutions of the quadratic equation

$$\left(1 + \frac{\lambda^2}{n_1}\right) r^2 - 2\left(z + \frac{\lambda^2}{2 n_1 p_2}\right) r + z^2 \left(1 - \lambda^2 \frac{1-p_2}{n_2}\right) = 0$$

were $z$ is the value of the ratio estimated from data. The $(1-\alpha)$ confidence limits are then, taking $z$ to be $p_1/p_2$,

$$\frac{\frac{p_1}{p_2}}{1 + \frac{\lambda^2}{n_1}} \left\{ 1 + \frac{\lambda^2}{2 n_1 p_1} \pm \lambda \sqrt{\frac{1-p_1}{n_1 p_1} + \frac{1-p_2}{n_2 p_2} + \frac{\lambda^2}{4}\left(\frac{1}{n_1^2 p_1^2} + \frac{4(1-p_2)}{n_1 n_2 p_2}\right)} \right\}$$

In the case where $\lambda = 1$ and $n_1$ and $n_2$ are large the above expression reduces to the familiar result

$$\frac{p_1}{p_2}\left\{1 \pm \sqrt{\frac{1-p_1}{n_1 p_1} + \frac{1-p_2}{n_2 p_2}}\right\}$$

## A.4 Why should the $\chi^2$ probability be flat ?

In our studies of results from $\chi^2$ fits of various distributions, we have argued that if the errors used in the fit are Gaussian and are correctly estimated, then the resulting $\chi^2$ probability distribution should be flat. Here we give a proof of this result in a more general context. Let $X$ be a random variable having probability density function $f(x)$. Consider a new random variable $Z$ defined by

$$Z = F(X) = \int_{-\infty}^{X} f(t)\,dt$$

Then $Z \in [0,1]$.

We shall assume that $f(x)$ is such that $F^{-1}(z)$ exists. Let $G(z)$ be the cumulative probablity function of $Z$. We can write

$$G(z) = P\left\{F(X) < z\right\} = P\left\{x < F^{-1}(z)\right\} = \int_{-\infty}^{F^{-1}(z)} f(t)\,dt$$

Taking the derivative of G with respect to $z$ we get

$$\begin{aligned} G'(z) &= (F^{-1}(z))'\, f(F^{-1}(z)) \\ &= \frac{1}{F'(F^{-1})} f(F^{-1}(z)) \\ &= \frac{1}{f(F^{-1})} f(F^{-1}(z)) \\ &= 1 \end{aligned}$$

which shows that $Z$ is a uniform random variable on $[0,1]$.

The converse is easily proved. Assume that $X$ is a random variable having probability density function $g(x)$. Let $f(x)$ be a probablity density function. We define $F(x)$ by

$$F(x) = \int_{-\infty}^{x} f(t)\,dt$$

We want to find out under which condition $F(X)$ is uniform on $[0,1]$. A necessary condition for this is that

$$P\left\{F(X) < z\right\} = P\left\{x < F^{-1}(z)\right\} = z$$

which is equivalent to

$$\int_{-\infty}^{F^{-1}(z)} g(t)\,dt = z$$

and taking the derivative on both sides of the previous equation, we find that

$$\frac{g(F^{-1}(z))}{f(F^{-1}(z))} = 1$$

from which it follows that $f = g$. Therefore a necessary and sufficient condition for $Z$ to be uniform on $[0,1]$ is that the integrand defining $z$ be the probability distribution function of $X$.

The $\chi^2$ function used to perform track-parameter estimates is a special case of the maximum likelihood method where the measurements are assumed to follow independent Gaussian distributions. If this hypothesis is satisfied, then the $\chi^2$ probability distribution will be uniform on $[0,1]$. Otherwise, by the previous result, it will deviate from uniformity. This can happen for instance when the measurement errors (i.e. the standard deviation of the Gaussians) are not estimated properly, or when the errors are simply not Gaussian.

## A.6 Maximum-likelihood estimator of efficiency functions

A most common problem faced in the stage of the analysis of data in a high energy-physics experiment is to estimate an efficiency $\varepsilon(r)$ as a function of a particular variable $r$. We observe $n$ values of $r$, $(r_1, r_2, \cdots, r_n)$, and for each of these values we observe the outcome of a Bernoulli variable $X$ taking the value 1 if the outcome is a success and 0 if it is a failure. A traditional method is to bin the random variable $r$ and in each bin in $r$ estimate the efficiency as the ratio of the number of successes to the number of trials in that bin. This can then be fitted to a particular functional dependence on $r$.

An alternative method is to determine the parameters characterising the particular functional dependence by maximising the maximum-likelihood function. Let the efficiency $\varepsilon$ be a function of $r$ depending on a vector of parameters $\alpha$

$$\varepsilon = p(r, \alpha)$$

The likelihood function $\mathcal{L}(\alpha)$ is then given by

$$\prod_{i \in S} p(r_i, \alpha) \prod_{j \in F} (1 - p(r_j, \alpha)$$

where $S$ is the set of successes and $F$ the set of failures.

Maximising $\mathcal{L}$ with respect to $\alpha$ is equivalent to maximising the logarithm of $\mathcal{L}$ with respect to $\alpha$

$$L(\alpha) = \sum_{i \in S} \log p(r_i, \alpha) + \sum_{j \in F} \log(1 - p(r_j, \alpha))$$

The estimator of $\alpha$ thus obtained is usually the solution of a transcendental equation which has to be solved numerically.

In the case of a single parameter $\alpha$, the equation can be solved numerically, for instance by the Muller method.

# References

M.R. Adams et al. (E665 collaboration) (1990a). *A Spectrometer for Muon Scattering at the Tevatron*, *Nuclear Instrumentation and Methods* **A291**, **533**.

M.R. Adams et al. (E665 collaboration) (1990b). *Preliminary results on neutron to proton cross-section ratio at low $x_{bj}$ from deep inelastic muon scattering at 490 GeV/c*, *Contributed talk to Singapore conference.*

S. Aïd, for the E665 collaboration (1990). *Preliminary results from E665 on cross-section ratios at low $x_{bj}$ using $H_2$, $D_2$ and Xe targets*, *Proceedings of the workshop on hadron structure functions and parton distributions, Fermi National Accelerator Laboratory, 26-28 Avril 1990* Ed. D.F. Geesaman, et al., World Scientific.

A.A. Akhundov, D.Yu. Bardin, N.M. Shumeïko (1986). *Electromagnetic cor-*

*rections to elastic radiative tail in deep inelastic lepton nucleon scattering,* *Soviet Journal of Nuclear Physics* **44**, 988.

A.A. Akhundov, D.Yu. Bardin, W. Lohmann (1986). *Radiative corrections to deep inelastic muon scattering, Dubna, preprint E2-86-104.*

P. Amaudruz et al. (NMC) (1991). *Gottfried sum from the ratio $F_2^n/F_2^p$,* *Physical Review Letters* **66**, 2712.

P.L. Anthony (1989a). *The Utility Match Pam (UMPAM), E665 memo SW082.*

P.L. Anthony (1989b). *Muon Matching, E665 software talk ST0149.*

W.B. Atwood, G.B. West (1973). *Extraction of asymptotic nucleon cross-sections from deuterium data,* *Physical Review* **D7**, 773.

J.J. Aubert et al. (EMC) (1987). *Measurements of the nucleon structure functions $F_2^N$ in deep inelastic muon scattering from deuterium and comparison with those from hydrogen and iron,* *Nuclear Physics* **B293**, 740.

D. Yu Bardin, N.M. Shumeĭko (1979). *Theoretical estimate of systematic effects in experiments on deep inelastic $l^{+-}$ N scattering,* *Soviet Journal of Nuclear Physics* **29**, 499.

A.C. Benvenuti et al. (BCDMS collaboration) (1990). *A Comparison of the structure functions $F_2$ of the proton and the neutron from deep inelastic muon scattering at high $Q^2$,* *Phys. Lett.* **B237**, 601.

M. Bernheim et al. (1981). *Momentum distribution of nucleons in the deuteron from the d(e,e'p)n reaction*, *Nuclear Physics* **A365**, 349.

A.A. Bhatti (1991). *The ratio of the proton and neutron structure functions in 490 GeV/c deep inelastic muon scattering*, *Ph.D. thesis*, University of Washington.

S.I. Bilen'kaya, S.M. Bilen'kiı, Yu. Kazarinov, L.I. Lapidus (1974). *Electromagnetic form factor of the proton and heavy hypothetical particles*, *JETP Letters* **19**, 317.

S.M. Bilenky (1974). *Introduction to Feynman diagrams*, Pergamon Press.

J.D. Bjorken (1969). *Asymptotic sum rules at infinite momentum*, *Physical Review* **179**, 1547.

A. Bodek, J.L. Ritchie (1981). *Fermi motion effects in deep inelastic lepton scattering from nuclear targets*, *Physical Review* **D23**, 1070.

E.D. Bloom et al. (1969). *High-energy inelastic $e-p$ scattering at 6° and 10°*, *Physical Review Letters* **23**, 930.

By R. Brun, R. Hagelberg, M. Hansroul, J.C. Lassalle (1978). *GEANT: Simulation program for particle physics experiments. User guide and reference manual*, *CERN-DD/78/2 Rev.*

P.D.B. Collins, A.D. Martin, E.J. Squires (1989). *Particle physics and cos-*

*mology*, John Wiley & sons.

M. Diemoz, F. Ferroni and E. Longo (1986). *Nuclear structure functions from neutrino scattering*, *Physics Reports* **130**, 293.

E.J. Dudewicz, S.N. Mishra (1988). *Modern mathematical statistics*, Wiley & Sons

W.T. Eadie, D. Dryard, F.E. James, M. Roos, B. Sadoulet (1971). *Statistical methods in experimental physics*, North-Holland Publishing Company.

U. Ecker (1988). *Determination of the liquid target densities in the E665 Run 1987/188*, *E665 memo AN025.*

R.P. Feynman (1969). *Very high-energy collisions of hadrons*, *Physical Review Letters* **23**, 1415.

L.L. Frankfurt, M.I. Strikman (1978). *On the problem of extracting the neutron structure function from eD scattering*, *Physics Letters* **76B**, 333.

J. Gasser, H. Leutwyler (1982). *Quark masses*, *Phys. Rep.* **87**, 77.

M. Gluck, E. Hoffmann, E. Reya (1982). *Scaling violations and the gluon distribution of the nucleon*, *Zeit. Phys.* **C13**, 119.

C.D. Green (1969). *Integral equation methods*, Barnes & Noble, Inc., New York.

T.P. Hettmansperger (1984). *Statistical inference based on ranks*, John Wiley & Sons, Inc.

H. Hochstadt (1973). *Integral equations*, Wiley & sons.

R. Hofstadter (1963). *Electron Scattering and Nuclear and Nucleon Structure*, Benjamin Inc.

R. Hofstadter, L. I. Schiff (1964). *Nucleon Structure*, *Proc. Inter. Conf. at Stanford, June 24–27 1963*, Standford University Press, California.

M. Kendall, A. Stuart, J.K. Ord (1987). *Kendall's Advanced Theory of Statistics*, Oxford University Press, New York.

D. Kusno, M.J. Moravcsik (1981). *The smearing corrections on deuterium targets*, *Nuclear Physics* **B184**, 283.

J. Kuti, V. Weisskopf (1971). *Inelastic lepton-nucleon scattering and lepton pair production in the relativistic quark-parton model*, *Physical Review* **D4**, 3418.

M. Lacombe et al. (1981). *Parametrization of the deuteron wave function of the Paris N–N potential*, *Physics Letters* **101B**, 139.

P.V. Landshoff, J.C. Polkinghorne (1978). *Fermi motion corrections for deuterium targets*, *Physical Review* **D18**, 153.

E. Leader, E. Predazzi (1982). *An introduction to gauge theories and the*

*'new physics'*, Cambridge University Press.

C. Lietzke, S.J. Wimpenny (1989). *A Comparison of the RadEMC and Bardin-Shumeiko Radiative Correction Programs*, *University of California (Riverside), Preprint UCR/DIS-89-06*

W. Lohmann, A.A. Akhundov (1990). *The treatment of the radiative corrections in a deep inelastic muon scattering experiment*, *Institut für Hochenenergiephysik, Zeuten, Preprint PHE 90-32.*

S.G. Mikhlin (1957). *Integral equations*, Pergamon Press Ltd.

L.W. Mo, Y.S. Tsai (1969). *Radiative corrections to elastic and inelastic ep and $\mu p$ scattering*, *Rev. Mod. Phys.* **41**, 205.

J.G. Morfin, Wu-Ki Tung (1990). *Parton distributions from a global QCD analysis of deep inelastic scattering and lepton pair production*, *Preprint FERMILAB-PUB-90/74.*

P.D. Morley, I. Schmidt (1986). *Relativistic Fermi motion and the EMC effect*, *Physical Review* **D34**, 1305.

N.F. Mott (1929). *Proc. Roy. Soc. London* **A124**, 425.

N.I. Muskelishvili (1953). *Singular integral equations*, P. Noordhoff N.V. – Groningen-Holland.

W.D. Nowak (1986). *Review of Deep Inelastic Charged Lepton Scattering*, *Fortschr. Phys.* **34**, 57.

W. Pogozelski (1966). *Integral equations and their applications*, Pergamon Press, PWN-Polish Scientific Publishers, Warszawa.

M.A. Preston, R.K. Bhaduri (1975). *Structure of the nucleus*, Addison-Wesley Publishing Company, Inc.

M.E. Rose (1948). *Physical Review* **73**, 279.

M.N. Rosenbluth (1950). *Physical Review* **79**, 615.

D.A. Ross, C.T. Sachradja (1979). *Flavour symmetry breaking in anti-quark distributions*, *Nuclear Physics* **B149**, 497.

P.J. Rousseeuw, A.M. Leroy (1987). *Robust regression and outlier detection*, Wiley & sons.

J.J. Ryan, M. Schmitt, A. Bhatti (1990b). *Chamber efficiencies*, *E665 memo AN081*.

J.J. Ryan (1991). *Particle production in deep inelastic muon scattering*, *Ph.D. Thesis*, Massachussets Institute of Technology.

A.F. Salvarani (1991). *Forward hadron production in muon deep inelastic scattering*, *Ph.D. Thesis*, University of California at San Diego.

M. Schmitt (1991a). *Private communication.*

M. Schmitt, S. Aïd (1991b). *Inefficiencies of the muon match, muon projection reconstruction and LAT filter, E665 Internal Memo AN090.*

M. Schmitt, S. Aïd (1991c). *Muon match inefficiency – An update, E665 Internal Memo AN091.*

M. Schmitt (1991d). *EMEV : Skimming $\mu e$ and $\mu\gamma$ Events, E665 Internal Memo.*

M. Schmitt (1991e). *Drift Chamber Efficiency Model, E665 Internal Memo AN083.*

M. Schmitt (1991f). *A study of the Momentum Discrepancy between the BEAM and FORWARD Spectrometers, E665 Internal Memo*

N.M. Shumeïko (1979). *On the approximate calculation of electromagnetic corrections to deep inelastic $l\,N$ scattering, Soviet Journal of Nuclear Physics* **29**, 807.

R.D. Smith (1986). *Effect of nuclear binding and Fermi motion on the ratio $R(A) = \sigma_L/\sigma_T$ in Deep Inelastic Scattering, Phys. Lett.* **B182**, 283.

T. Sjöstrand (1982). *The Lund Monte Carlo for jet fragmentation, Comp. Phys. Comm.* **27**, 243.

A. Sudbery (1986). *Quantum mechanics and the particles of nature,* Cam-

bridge University Press.

S. Stein et al. (1975). *Electron scattering at 4° with energies of* 4.5-20 *GeV*, *Physical Review* **D12**, 1884.

L. Valentin (1981). *Subatomic Physics : Nuclei and Particles*, Hermann.

R. Voss (1985). *Structure Functions : Deep Inelastic Scattering on Nucleons and Nuclei*, in *The Quark Structure of Matter, Proc. of a topical European Meeting in the Rhine Valley (Strasbourg-Karlsruhe), 26 September – 1 October 1985* Ed. M. Jacob and K. Winter, World Scientific.

B.L. van der Waerden (1969). *Mathematical statistics*, Springer Verlag.

G.B. West (1971). *Total neutron cross-sections may not be what they seem to be*, *Phys. Lett.* **37B**, 509.

G.B. West (1972). *The Dōppler effect in the extraction of total neutron cross-sections from deuterium data with particular emphasis on asymptotic hadron and deep inelastic electron scattering*, *Ann. Phys.* **74**, 464.

F. Wilczek (1982). *Quantum Chromodynamics : The Modern Theory of the Strong Interactions*, *Ann. Rev. of Nucl. and. Part. Science* **32**, 177.

W. Wittek (1981a). *Determination of the point(s) of closest approach for two charged tracks in an inhomogeneous magnetic field*, *EMCSW/81/15*.

W. Wittek (1981b). *The convex method, EMCSW/81/14.*

V.R. Zoller (1991). *The nucleon structure functions in deep inelastic scattering off deuterium : nuclear shadowing and Gottfried sum rule, Moscow, preprint ITEP-91-58.*